Stony Brook University

On the Anelastic Behavior of Plasma Sprayed Ceramic Coatings: Observations, Characterizations and Applications

A Dissertation Presented

by

Gopal Dwivedi

to

The Graduate School

In Partial Fulfillment of the

Requirements

for the Degree of

Doctor of Philosophy

in

Materials Science and Engineering

Stony Brook University
August 2011

Stony Brook University

The Graduate School

Gopal Dwivedi

We, the dissertation committee for the above candidate for the
Doctor of Philosophy degree, hereby recommend
acceptance of this dissertation.

Dr. Sanjay Sampath – Dissertation Advisor
Professor, Materials Science and Engineering

Dr. Christopher Weyant – Chairperson of Defense
Assistant Professor, Materials Science and Engineering

Dr. Toshio Nakamura
Professor, Mechanical Engineering

Dr. Curt Johnson
Adjunct Professor, Materials Science and Engineering

Dr. Carlos G. Levi
Professor, Materials and Mechanical Engineering
University of California Santa Barbara

This dissertation is accepted by the Graduate School

Lawrence Martin
Dean of the Graduate School

Abstract of the Dissertation

On the Anelastic Behavior of Plasma Sprayed Ceramic Coatings: Observations, Characterizations and Applications

by

Gopal Dwivedi

Doctor of Philosophy

in

Materials Science and Engineering

Stony Brook University

2011

Plasma sprayed ceramic materials contain an assortment of microstructural defects, including pores, cracks, and interfaces arising from the droplet based assemblage of the spray deposition technique. The defective architecture of the deposits introduces a novel "anelastic" response in the coatings comprising of their non-linear and hysteretic stress-strain relationship under mechanical loading. It has been established that this anelasticity can be attributed to the relative movement of the embedded defects under varying stresses; while the non-linear response of the coatings arises from the opening/closure of defects, hysteresis is produced by the frictional sliding among defect surfaces. Recent studies have indicated that anelastic behavior of coatings can be a unique descriptor of their mechanical behavior and related to the defect configuration. In this dissertation, a multi-variable study employing systematic processing strategies was conducted to augment the understanding on various aspects of the reported

anelastic behavior. Enhancements to bi-layer curvature measurement technique allowed for reliable and repeatable quantification of the anelastic response, enabling extraction of three anelastic parameters; elastic modulus, non-linear degree and hysteresis degree. This allowed for further exploration of the process space enabling controlled introduction of anelasticity in thermal sprayed ceramic coatings.

This dissertation reports on these findings by first describing the experimental advancements in bilayer curvature measurements via thermal cycling of a coated beam. This experimental development allowed assessment of sensitivity and repeatability of the obtained anelastic parameters to varying microstructures imposed by processing excursions. Subsequently, controlled modification of anelasticity was achieved through material and process parameters as well as through extrinsic modification of the defects within the microstructure. The results suggest that anelasticity can be tuned by manipulation of the material as well as processing conditions, and the presence of foreign materials in a coating is seen to have significant influence on the coating response. The anelastic response was also verified through purely mechanical (four-point-bend) loading of ceramic coatings on substrates at room temperature in order to avoid any temperature effects in anelasticity measurements.

The implication of this work is significant as it provides a comprehensive and quantitative description of the properties of layered, high defect density ceramic coatings produced from complex deposition processes such as plasma spray. These quantitative descriptors will not only provide opportunities to generate/produce/create enhanced design of thermo-structural coatings but also a robust methodology for process-structure-property-performance relations.

Dedicated To

My lovely wife, My parents and Late Prof. Bala

Table of Contents

List of Figures.....ix

List of Tables.....xvii

Acknowledgements.....xviii

1. Introduction 1

1.1. Anelasticity in bulk materials 1

1.2. Anelasticity in layered structures 4

1.2.1. Rocks 4

1.2.2. Bones and Nacre 6

1.2.3. Plasma sprayed ceramics 10

2. Statement of the problem 19

3. Experimental procedures 22

3.1. Coating Deposition 22

3.1.1. Plasma spray process 22

3.1.2. Coating deposition 24

3.2. Thickness, weight and curvature measurements 27

3.3. Free-standing coating preparation 28

3.4. Thermal conductivity measurements 28

3.5. Indentation elastic modulus and hardness measurements 28

3.6. Four-point bend (4PB) test 29

4. Measurement and quantification of anelastic behavior via bi-layer curvature-temperature (BCT) measurements 31

4.1. Coating modulus and stress calculations based on BCT measurements 31

4.1.1. Stress calculations 31

4.1.2. Elastic modulus calculations 33

4.2. Stress evolution during coating deposition: in-situ coating property (ICP) sensor 34

4.3. Ex-situ thermal cycling of a deposited coating: BCT measurement sensor 38
4.3.1. Reproduction of curvature-temperature curve by heating the coating using a flame torch 38
4.3.2. Thermal cycling of coating using a heat-blower 40
4.3.3. Uniform thermal cycling of coating in a furnace 41
4.4. Quantification of anelastic properties 43
4.5. Summary and understanding of the anelasticity parameters 47
5. Sensitivity of anelasticity and its application in coatings repeatability assessment .. 49
5.1. Single crack model 50
5.2. Multiple crack model applied on a crack matrix 52
5.3. Simulation of curvature-temperature plot for the given crack matrix 53
5.4. Experimental results on sensitivity of anelasticity to process excursions 54
5.5. Repeatability assessment of coatings using anelastic parameters 60
5.5.1. Design of experiment 63
5.5.2. Characterizations and repeatability assessment 64
6. Controlled introduction of anelasticity via processing parameters 70
6.1. Spray distances 70
6.2. Spray particles energies 76
6.3. Coating deposition Pattern 80
7. Role of interface character on anelastic behavior 86
7.1. Topological modification of defect surfaces 86
7.2. Interface surface modification by introduction of salt to the coatings 90
7.2.1. Immersion of a PS YSZ coating into a salt solution 91
7.2.2. Effect of salt immersion on the anelasticity of amorphous coatings 94
7.2.3. Change in anelasticity due to introduction of salt during deposition 96
8. Mechanical equivalence of bi-layer curvature measurement at room temperature 100
8.1. Results and discussion 100
8.2. Examination of error sensitivity of elastic modulus on the input parameters to the model 103

9. Plasma sprayed ceramics and nacre like materials: similarities in mechanical response 106

10. Summary and Conclusions 112

11. Suggestions for future work 117

11.1. Anelasticity and mechanical damping in plasma sprayed YSZ coatings 117

11.2. TBC anelasticity and service life 118

11.3. Anelasticity in coatings sprayed with other thermal spray processes 121

11.4. Experimental approach to observe anelasticity under compressive thermal loading 124

11.5. Anelasticity and fracture toughness 125

References 128

List of Figures

Figure 1.1: a) and (b) shows the schematic of instant loading in terms of stress and strain respectively, and (c) and (d) are the corresponding strain and stress response of a real solid[3]. The effect lags the cause under the two different loading conditions and the time to match the response of a defect free solid depends on the time relaxation constants τ_σ and τ_ε. 2

Figure 1.2: A typical stress strain curve of a ductile material. The material shows a strain recovery of ε2-ε3 attributed to the anelasticity[4]. 3

Figure 1.3: Representative stress-strain curve of rocks under uniaxial compression[6]. 5

Figure 1.4: (a) Axial and lateral strain under uniaxial compression of Westerly Granite rocks. (b) Linear strain of the same rock under hydrostatic pressure[7] 6

Figure 1.5: Hierarchical structure of nacre over several length scale present in red abalone shell[11]..... 7

Figure 1.6: Copy of an oscilloscope trace of the load displacement curve of a pearl oyster under a cyclic uniaxial tensile loading. The strain relaxation was observed while the specimen was allowed to relax for one minute between loadings.[14] 8

Figure 1.7: Schematic representation of hierarchical structure of bone[15]. 9

Figure 1.8: Experimentally measured stress-strain behavior of a trabecular bone under uniaxial compression[16]. Inset shows the SEM image of the trabaculae mesh structure with arrows pointing to the trabeculae..... 10

Figure 1.9: Stress-strain relationship of a cylindrical dog-bone tensile specimen under 1st, 2nd and 50th cyclic compressive loading. Note that the response during first cycle is different than others.[17] 11

Figure 1.10: Figure 1.10: Stress-strain relationship of PS YSZ coating under different mode of loading. Note that the difference in mechanical behavior of the coating under compression and tension are anelastic and slightly different[18]..... 12

Figure 1.11: Stress-strain relationship of PS YSZ coating sprayed on one side of Aluminum plate obtained from $\kappa - T$ response of the specimen during a heating and cooling cycle. Point (A) corresponds to start of the heating and point (B)[26] that of cooling 13

Figure 1.12: A schematic of plasma sprayed process and coating formation. 15

Figure 1.13: (a) microstructural details of a single splat. (b) detailed characterization of different types of defect in a fractured as well as polished cross sections of a PS YSZ coating..... 15

Figure 1.14 : (a) sliding of splat interface upon compressive loading[17]. (b) *in-situ* measurement of relative displacement of a pore and evidences of interfacial sliding of splats under different stress magnitudes[49]..... 17

Figure 1.15: A schematic representation of the two mechanisms responsible for anelasticity in plasma sprayed coatings[50]..... 18

Figure 3.1: (a) Schematics of plasma spray torch. (b) cross sectional drawing showing interiors of the torch and (c) the F4 SULZER plasma spray torch..... 23

Figure 3.2: Illustration of "injection optimization" procedure. At optimum injection condition particles achieve maximum temperature and velocity..... 24

Figure 4.1: Schematics of in-situ coating property (ICP) sensor..... 35

Figure 4.2: Curvature calculation scheme from the three point deflection records by displacement laser sensor measurements..... 36

Figure 4.3: A typical curvature and temperature plot against time obtained from the ICP sensor. The steps for deposition process are mentioned in the figure..... 36

Figure 4.4: The curvature-temperature plot of the ICP data shown in Figure 4.3. During the cooling down process, the coating shows non-linear behavior..... 37

Figure 4.5: The schematics and photograph of specimen heating using a flame torch to reproduce the cooling curve of Figure 4.4..... 39

Figure 4.6: A typical curvature temperature record obtained from flame torch heating of substrate. The figure displays a clean non-linear behavior of the coating during the cooling..... 39

Figure 4.7: The schematics and photograph of specimen heating method using a box-heater assembly..... 40

Figure 4.8: (a) curvature-temperature plots obtained from box heater assembly for the two different blowing directions. (b) temperature dependent front and back temperature difference for the two cases. Two things are to be noted. First, the box heater assembly introduces significantly large thermal gradient, and second, the curvature changes are different for the two modes of heating..... 41

Figure 4.9: The schematics and photograph of advancement in specimen heating using a muffle furnace..... 42

Figure 4.10: A repeatable curvature-temperature plot obtained from furnace heating of specimen. To shorten the time for cooling down, the specimen was taken out of the furnace at T_{out}=170°C. 42

Figure 4.11: A repeatable curvature-temperature plot obtained from heating and cooling both in the furnace. First cycle is different from the consecutive cycles. 43

Figure 4.12: Stress-strain calculation scheme from a curvature-temperature data of a coating. (a) a typical curvature-temperature plot obtained from BCT measurements. The data is processed to calculate the stress-strain relationship (b) from the heating part of (a). (c) shows the complete stress-strain cycle corresponding to (a). Note that the *E* and *ND* are calculated only from loading or heating part of the stress-strain curve. 44

Figure 4.13: Illustration of possible behavior of a coating on the reversal of loading for coatings with three different crack densities. The area of hysteresis loop, and hence the HD, can significantly differ even for the same loading curve. 48

Figure 5.1: Schematics of the embedded crack under compression used by Liu et al. The angle (θ), coefficient of friction (μ), crack face openings (δ), and crack length (a) were used as inputs to the model for the stress-strain calculations[47]. 50

Figure 5.2: The four stages of the response of the single crack under compression. Note that after stage IV, another stage I would be required to bring the crack to its starting (zero) stress state[47]. 51

Figure 5.3: (a) effect of different coefficient of friction on the single crack's response. (b) effect of different crack face openings. The hysteresis is largest for the case of μ= 0.5 and δ= 0[26]. 52

Figure 5.4: (a) multiple cracks mesh modeled from a PS YSZ coating. (b) stress-strain relations obtained from the approximated multiple crack formula and FEM analysis[26]. 52

Figure 5.5: (a) multiple cracks mesh on an aluminum substrate to be analyzed for its curvature-temperature response. (b) results obtained from multiple-crack model analysis of the configuration under temperature change. Not only, cracks are capable of introducing anelasticity, but also the anelasticity degree can be changed by modifying the coefficient of friction between crack faces[26]. 54

Figure 5.6: : SEM micrograph for powders with (a) Hollow Sphere (HOSP) and (b) Fused and Crushed (FC) morphologies. Polished ((c) and (d)) and fractured[26] ((e) and (f)) cross sections of HOSP and FC coatings sprayed at similar processing conditions. It is interesting to note how different powder morphologies form coatings with different defect architectures. HOSP coating exhibits more number of interfaces and cracks than the FC coating. 57

Figure 5.7: Curvature- temperature responses ((a) and (c)) and their computed stress-strain relations ((b) and (d)) of the two HOSP coatings. HOSP- A was sprayed with higher feedrate than that used for HOSP- B. The two coatings show significantly different anelastic responses both in curvature-temperature as well as stress-strain relations[26]. 58

Figure 5.8: Curvature- temperature responses ((a) and (c)) and their computed stress-strain relations ((b) and (d)) of the two FC coatings. For FC- A, a finer powder cut was used than that used for FC- B. The coating sprayed with fine powder cut shows lesser hysteresis than that sprayed with coarse powder cut[26]. 59

Figure 5.9: The non-linear parameters, E, ND and HD, of the four coatings along with their hysteresis degree (HD). The coatings are mapped on to the E-ND space for a better comparison[26]..... 60

Figure 5.10: Schematic illustration of the steps involved in a coating deposition process. Variability introduced at any stage of these steps can change the coating properties, and hence its performance[67]. 61

Figure 5.11: Illustration of TBCs distribution over their life cycle. A large number of coatings show much lower life cycle. A better reproducibility of a process can narrow the distribution. 62

Figure 5.12: % variability in thermal conductivity measurements of a standard sample, a single PS YSZ and six different PS YSZ coating specimens from a single coating. The data clearly represents the intrinsic variability associated with the instrument (1.9%) and the coatings (8%)[44, 67]. 63

Figure 5.13: (a) schematics of carousel setup used for spraying of batch- 1 and 2. (b) the particle size distributions of the powder used for fabrications of batch- 1,2 and 3. Batch-3 was sprayed with a narrow size distribution powder[67]. 64

Figure 5.14: Post-spray deposition analysis and characterization for the three batches of YSZ coatings. Each measurement displays different order of variability in the coatings of that batch.[67]..... 67

Figure 5.15: Map of non-linear elastic properties of plasma sprayed YSZ coatings from the three batches. Batch- 3, sprayed on carousel and with narrow powder cut, shows highest repeatability among the three batches[67]. 68

Figure 6.1: (a) Average T & V measured with DPV2000 sensor for coatings sprayed with three spray distance: YSA-A (60 mm), YSZ-B (100 mm) and YSZ-C (150 mm). (b) shows the melting index and kinetic energy distribution of the particles corresponding to the three coatings with their microstructures. The zero melting index is shown by dotted line. One can easily observe that coating sprayed with

longer spray distance contains higher number of interfaces and unmelts attributed to the lower melting index of the particles. 72

Figure 6.2: Thermal conductivity of the three coatings sprayed at different spray distances. 73

Figure 6.3: Curvature-temperature and stress-strain curves for the three coatings, YSZ-A, YSZ-B and YSZ-C. YSZ-B exhibits larger hysteresis area than YSZ- C, however the hysteresis degree is higher for YSZ-C as the area is normalized to the total stress-strain change[50]. 74

Figure 6.4: The three anelastic parameters for the YSZ- A, B and C coatings sprayed at three different spray distances, 60, 100 and 150 mm respectively[50]. 75

Figure 6.5: Hysteresis degree obtained from curvature-temperature plot and the stress-strain curves for the three coatings, YSZ-A, B and C. The absolute values from the two different calculation methods are somewhat different; however their trend is almost similar. 76

Figure 6.6: (a) Average T & V measured with DPV2000 sensor for coatings sprayed with three spray distance. YSA-D (Low E), YSZ-E (Med E) and YSZ-F (High E). (b) shows the melting index and kinetic energy distribution of the particles corresponding to the three coatings with their SEM micrographs. YSZ-D coating shows higher porosity and splat interfaces due to overall low melting index among the three coatings 78

Figure 6.7: Curvature-temperature curves for the three coatings sprayed with three different plasma energies, YSZ-D, YSZ-E and YSZ-F[50]. 79

Figure 6.8: The three anelastic parameters for the coatings sprayed at three different plasma energies. YSZ- D, E and F corresponds to Low, Medium and High energy conditions respectively[50]. 80

Figure 6.9:: Schematics of raster pattern used for the deposition of coatings YSZ- G, H and I. 81

Figure 6.10: Curvature-temperature curves for the three coatings, YSZ-G, YSZ-H and YSZ-I. The visual inspection of the curves suggests that the coating sprayed with different deposition pattern exhibit different anelastic response. 82

Figure 6.11: The anelastic parameters of the three coatings sprayed with different deposition patterns. The coatings sprayed on ICP sensor display significantly different microstructures. 83

Figure 6.12: The anelastic parameters of the three coatings sprayed with different deposition patterns. 84

Figure 7.1: (a) exhibits surface roughness introduced due to cracking within a splat. (b) fractured surface of PS YSZ coating showing the nano-scale roughness on the splat surface due to columnar grain termination[50]..... 87

Figure 7.2: SEM micrographs of (a) splats morphology and (b) polished and (c) fractured cross sections of the three amorphous coatings, mullite, cordierite and forsterite. None of the three coatings display any sign of cracking at splat levels, however some crystallinity can be observed in forsterite coating..... 88

Figure 7.3: XRD data of the three amorphous coatings. Forsterite coating shows more number of peaks than Mullite and cordierite coatings indicating higher degree of crystallinity associated with it..... 88

Figure 7.4: Curvature-temperature responses of three amorphous coatings obtained from BCT measurements. Cordierite coating shows highest non-linearity among the three attributed to its high porosity content. All three coatings exhibit limited hysteresis in their anelastic behavior. 89

Figure 7.5: Anelastic parameters of the three amorphous coatings. Both the ND as well as HD are lower in the case of mullite coating. 90

Figure 7.6: Curvature-temperature response of YSZ- J coating after treatment with salt solution followed by water. The response after salt solution treatment is shifted in Y-axis for clarity 92

Figure 7.7: Curvature-temperature response of YSZ- J coating after treatment with salt solution and then water. The response after salt solution treatment is shifted in Y-axis for clarity. 92

Figure 7.8: Curvature-temperature response of mullite and forsterite coatings before and after salt solution treatment. Forsterite shows higher degree of change in anelasticity than mullite..... 95

Figure 7.9: Anelastic parameters of the two amorphous coatings before and after salt solution treatments. 96

Figure 7.10: (a) schematic of salt solution spraying with coating deposition. (b) the curvature-temperature responses of the coating, YSZ-K and L. Coating sprayed with salt-solution jet shows very high degree of anelasticity..... 97

Figure 7.11: The SEM micrographs of YSZ-J coating cross section polished under (a) wet and (b) dry conditions. The EDS spectra of polished surfaces show presence of Na in the cross section polished under wet conditions. On the other hand the dry polished cross section does not show a significant Na peak suggesting a uniform distribution of salt in coating. 98

Figure 7.12: E and HD values for YSZ-J and K coatings. Both the parameters were higher for the case of coating deposited with salt solution stream. 98

Figure 8.1: Extraction of non linear properties of coatings from 4PB test; (a) a typical curvature-moment plot obtained from test. The careful selection procedure of transition moment is depicted in the figure. (b) stress-strain curve obtained from the processing of moment-curvature plot shown in (a)[57]. 101

Figure 8.2: The E vs ND map for comparative study between the non-linear properties obtained from BCT thermal cycle as well as 4PB test. The E values from 4PB data are more scattered than those from thermal cycling data, which can be attributed to a higher sensitivity to errors in 4PB test as well as temperature change involved in the BCT thermal cycle test[57]. 102

Figure 8.3: Stress strain curve estimated for curvature-temperature data from BCT thermal cycle test and curvature-temperature data from 4PB test for a single specimen. The coating suffering from mechanical load shows less non-linearity[57]. 103

Figure 9.1: (a, b) are the polished cross section of a nacre from abalone shell at two different magnifications. (c) is the SEM image of a fractured cross section of the same nacre. All the three images display a brick-mortar assembly in the nacreous structure..... 107

Figure 9.2: The load displacement curves of (a) a plasma sprayed YSZ coating under three-point bending and (b) a nacre under uniaxial tensile loading condition[14]. Given that the modes of loadings were different, the mechanical responses of the two structures are noticeably comparable. 107

Figure 9.3: Schematic comparison of microstructure of plasma sprayed ceramics and nacre. Under loading condition, both the layered structures undergo movements between the layers(splats or platelets). *(Diagram courtsey: Prof. Christopher Weyant, Stony Brook University.)* 108

Figure 9.4: (a) comparison between the layered structure of nacre and plasma sprayed YSZ coating. Both the structures show waviness in their constitutive layers. (b) the roughness associated with nacre platelets and splat surfaces. (c) exhibits presence of asperity and bridge between nacre platelets. These features contribute to the toughening and strength of the nacreous structure[71]. 109

Figure 9.5: The load displacement curves of an as-sprayed and a PMMA infiltrated plasma sprayed YSZ coatings under three-point-bend loading. The infiltrated coating displays higher strength and hysteretic behavior as compared to as-sprayed one. It also exhibits more graceful failure mode than the as-sprayed coating..... 110

Figure 9.6: A fractured cross section of infiltrated YSZ specimen at two different magnifications. Bridging and tearing of the polymer attributes to enhanced mechanical properties of the coating. 111

Figure 10.1: Effect of different types of defects in a coating on the three anelastic parameters. 116

Figure 11.1: tanδ and degree of hysteresis (HD) of the coatings sprayed with three different plasma enthalpies. 118

Figure 11.2: A typical plasma sprayed TBC system consists of a Hastelloy superalloy, NiCrAlY bondcoat and PS YSZ as the top coat. 119

Figure 11.3. The growth of thermally grown oxide (TGO) in a TBC system. The TGO develops high compressive stresses (~ 1GPa) at the coating and bondcoat interface leading the topcoat to failure.[76, 77] 120

Figure 11.4: The curvature-temperature responses of three HVOF Alumina coatings sprayed with different raster speeds. The slowest raster speed introduces anelasticity in the coating.[76, 77] 121

Figure 11.5: Curvature-temperature responses of the three Mo coatings. (a) thin coating and (b) thick coating sprayed by APS process. (c) thick coating sprayed by flame spray process. 123

Figure 11.6: The anelastic curvature-temperature responses of YSZ coating on a Mo substrate. Due to lower CTE of substrate, the coating undergoes compression upon heating. 124

Figure 11.7: Comparison between the fracture toughness and nonlinearity of PS YSZ coatings. 126

List of Tables

Table 5.1: shows the details of powders used for the coating depositions, and their corresponding particles temperature and velocity measured by AccuraSpray sensor[26]. 56

Table 6.1: The plasma input parameters and measured output power for the three conditions. The spray distance and raster speed were kept constant at 100 mm and 500 mm/sec. 77

Table 7.1: Thickness and CTE value used for the calculation of anelastic parameters of the three amorphous coatings 90

Table 8.1: Error analysis for (a) thermal test; (b) 4PB test in calculation of initial modulus induced from the errors in different input parameters[57]. 104

Acknowledgements

First, I would like to convey my special regards to Prof. Sanjay Sampath for his supportive as well as motivating guidance throughout this research. I would also like to express my sincere gratitude to Professor Nakamura for his expert suggestions and discussions on the experiments and interpretations of the results. I really appreciate the advice and knowledge I gained from Professor Chris Weyant and Dr. Curt Johnson from their vast repertoire of research experiences and am grateful to them for agreeing to be a part of of my examination committee. Sincere thanks to Professor Carlos Levi for considering my request to be present as an external member of my examination committee. I would also like to thank Professor David Welch for his suggestions time and again and for the long discussions that helped interpretation of many of my experimental results.

I appreciate the help received from Xi Yang of the Mechanical Engg. Department in installing the 4PB setup and processing the experimental data. Also, I am thankful to Prof. Chad Korach for allowing us to perform 4PB tests in his laboratory. I am thankful to Dr. Amit Shyam and Dr. Edgar Lara-Curzio from HTML laboratory at ORNL for their help and support in mechanical behavior characterization of coatings.

I am thankful to Steve Baader for helping me design the new version of ECP sensor, without his help this research would not have progressed this far. I am grateful to Dr. Jose Colmenares-Angulo, Dr. Kentaro Shinoda and Dr. Yang Tan for spending their precious time in spraying coatings for my experiments. I am also thankful to Dr. Alfredo Valarezo for his ever innovative ideas for experiments. For lending their moral support, suggestions and knowledge, I am grateful to my friends Dr. Brian Choi and Chris Jensen. Without the good times that we spent together it would have been difficult to handle the work pressure. Thank you my friends! Dr. Jim Quinn from Materials Sciences Department deserved a special thanks for his help with microscopy studies. I appreciate Glenn Bancke for his kind help on several occasions. I also would like to thank Lynn Allopenna and Debby Michienzi for their help with all official paper work.

Furthermore, I want to thank the CTSR family members, especially Travis Wentz, Eduardo Mari, Lorena Bejarano, Arash Gabchi, Katherine Flynn, Ari Sagiv, Dr. Yikai Chen, Dr. Dimitris Zois, Ravi Dey and Ling Li for their support and help at several stages of research.

I especially want to thank my colleagues Vaishak Viswanathan and Junghan Kim for their valuable help in conducting many of my experiments. I am also thankful to my friend Shekhar Sastry for being there during tough times.

Last but not the least, I would like to dedicate my thesis to my lovely wife, my parents and late professor R. Balasubramaniam for their never ending support and constant motivation throughout the course of my research.

1. Introduction

1.1. Anelasticity in bulk materials

"The property of a solid by virtue of which stress and strain are not uniquely related in the elastic range will be called "anelasticity". Clarence Zener[1] (1946)

A defect free solid behaves in an ideally elastic manner obeying the Hooke's law, where stress is always proportional to strain below the yield point of material (eq. (1.1)). In other words, the solid would return to zero stress upon zero strain or vice-versa.

$$\sigma = E\varepsilon \qquad \text{Eq. (1.1)}$$

Deviations from ideal elastic behavior are introduced in certain solids due to presence of microstructural and crystallographic defects rendering reversible stress-strain relations that are not unique. Such a response is deemed anelastic and can arise from atomic diffusion, internal friction and associated time dependent effects. The anelastic behavior of material in a real solid is determined by atomic movements and this is governed by the diffusion kinetics of mobile atoms and point defects[2].

The quantitative model to describe anelasticity was first proposed by W. Voigt in 1882[1].

$$\sigma + \tau_\varepsilon \dot{\sigma} = M_R(\varepsilon + \tau_\sigma \dot{\varepsilon}) \qquad \text{Eq. (1.2)}$$

This model incorporated stress and strain along with their first time derivatives using a linear response of the material. In this model (Eq. (1.2)) stress σ, and strain ε, and their respective time derivatives, (stress) $\dot{\sigma}$ and (strain) $\dot{\varepsilon}$ are related through a linear response equation with τ_ε and τ_σ which are the time relaxation constants for the stress and strain respectively. The coefficient M_R is the reduced modulus which is the real part of the complex modulus under cyclic loading of material. As it can be observed, the model is a generalized version of the Hooke's law. Instead of having just one parameter, like the elastic modulus in the case of Hooke's law, the anelasticity equation has three materials parameters: the strain and stress relaxation time and the reduced elastic modulus. Figure 1.1 shows the systematic illustration of the response of

the materials upon an instant loading of the material in two different ways. In both the cases the effect (stress or strain) does not follow the cause (strain or stress) instantaneously and in reality, the effect lags in time with respect to the cause. If the system is kept under a constant load for an adequate period of time a stress or strain value corresponding to the Hooke's linear stress-strain value would be achieved. This occurrence of residual deformation which gradually disappears is also known as elastic after effect or anelasticity[1] .

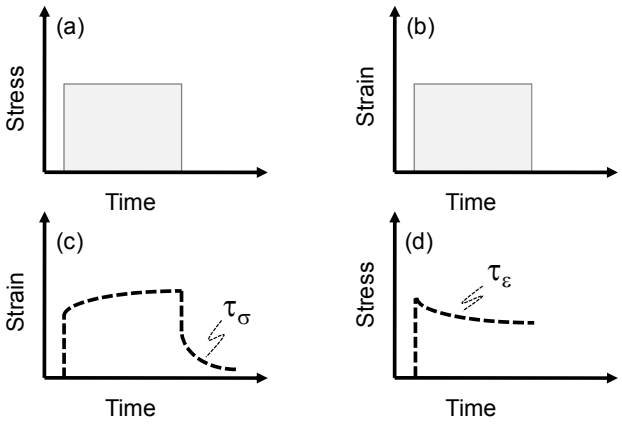

Figure 1.1: a) and (b) shows the schematic of instant loading in terms of stress and strain respectively, and (c) and (d) are the corresponding strain and stress response of a real solid[3]. The effect lags the cause under the two different loading conditions and the time to match the response of a defect free solid depends on the time relaxation constants τ_σ and τ_ε.

Another phenomenon associated with the anelastic behavior of materials is Internal Friction. This is the dissipation of mechanical energy as a result of anelastic processes occurring in a strained solid[3]. For a cyclically loaded solid, the internal friction is calculated as the ratio of the dissipated energy over the total stored energy per unit volume. If the solid is strained in a periodic manner, the internal friction represents the damping of the solid.

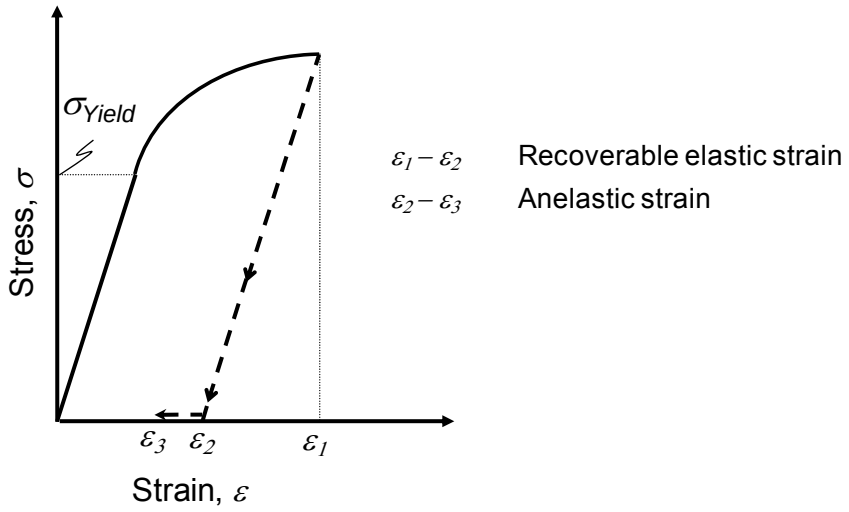

Figure 1.2: A typical stress strain curve of a ductile material. The material shows a strain recovery of ε2-ε3 attributed to the anelasticity[4].

The anelastic behavior in a ductile material can also be seen under quasi-static loading (Figure (1.2)). For example, when a metal is loaded to certain plastic strains, say ε_1 and the stress is released, the system returns to a state of residual strain of ε_2 with the elastic strain recovery of $\varepsilon_1 - \varepsilon_2$. However, over the course of time the system goes through another stage of time dependent strain recovery $\varepsilon_2 - \varepsilon_3$. Since this recovery is a time dependent phenomenon, it is referred to as "anelastic strain recovery". This can be attributed to the relaxation kinetics of the lattice defects in the ductile material[5].

For the case of metals, there have been several mechanisms proposed by many researchers for the physical origin of anelasticity. Some of them are localized relaxation centers, slip bands and lattice defects such as voids, dislocations and grain boundaries[1]. However, there are many instances where the anelasticity can also be induced by diffusion mechanisms within the materials. For example, the Snoek relaxation is the stress-induced migration of C, N or O atoms in metals with bcc lattice structure. The Zener effect, where the atom pairs of substitutional alloys, pairs of interstitial atoms and solute vacancy pairs possessing lesser symmetry than the lattice tend to form elastic dipoles, which, upon the application of stress can reorient themselves to contribute to the stress relaxation mechanisms. Another type of relaxation is the Gorski effect, where a solute which produces lattice dilation in a solvent undergoes a long range diffusion path. This relaxation is initiated by an introduction of macroscopic strain gradient which changes the chemical potential of the solute[3]. The detailed analysis on these relaxation mechanisms are beyond the scope of this study. Nevertheless, their contributions to anelasticity are more important in this context.

The above discussion was based on a typical crystalline solid material, where only lattice defects contribute to anelasticity. However it did not include any other physical defects such as cracks, pores, interfacial defects in a layered structure etc. which are commonly found in natural and engineered material. Evidence for instances, where these defects induce anelasticity to the system at very low strain rates, exists for both natural and synthetic systems. The mechanisms here closely resemble those responsible for anelasticity in real solids such as the energy dissipation resulting from internal friction phenomenon, however, the interpretation of the structure-property relations are completely different. It is this topic, relevant to layered materials produced via spray deposition, which is of prime interest to this dissertation.

The following subsection discusses relevant systems where the stress-strain relationship represents an anelastic response due to microscopic length scale defects in structure.

1.2. Anelasticity in layered structures

1.2.1. Rocks

Rock is one of the most common layered ceramic structures present in nature. Interestingly, most crystalline rocks exhibit an anelastic behavior on mechanical loading. Figure 1.3 shows a schematic representation of such an anelastic, non-linear and hysteretic response of a rock[6]. The slope of stress-strain curve increases as stress is increased. This behavior under uniaxial compression is similar to that under external hydrostatic pressure, except for the hysteresis which is not present in the latter case. The non-linearity of rocks can be attributed to the cracks present in it. At low stresses, the cracks are open, and as the cracks experience the compressive stress field around them they start to close making the rock elastically stiffer. Since the orientations of cracks in rocks are quite flat, above a certain stress limit/value no change in stiffness due to crack closure occurs, therefore the response of the material is linearly elastic (Figure 1.3).

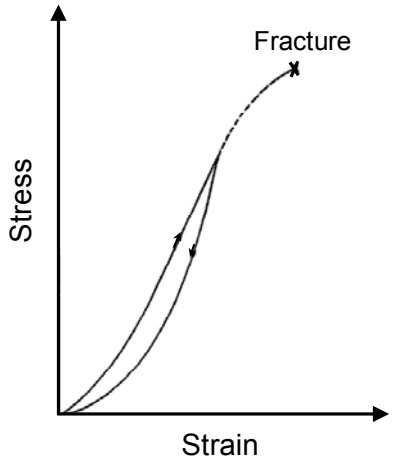

Figure 1.3: Representative stress-strain curve of rocks under uniaxial compression[6].

Similar to the explanation given for non-linearity, one could hypothesize the contribution of crack to hysteresis. Under uniaxial compression, although the cracks and pores are closing with increasing stresses, some sliding between the crack faces is still possible. This sliding motion dissipates energy due to friction and contributes to the hysteretic response of the rocks. For a westerly granite rock, Walsh showed experimentally that both axial as well as lateral stress-strain responses exhibit the anelastic response (Figure 1.4(a))[6]. Moreover, under hydrostatic pressure conditions, the crack face sliding is restricted, and hence reduced hysteresis is observed in the stress-strain response (Figure 1.4(b)).[6]

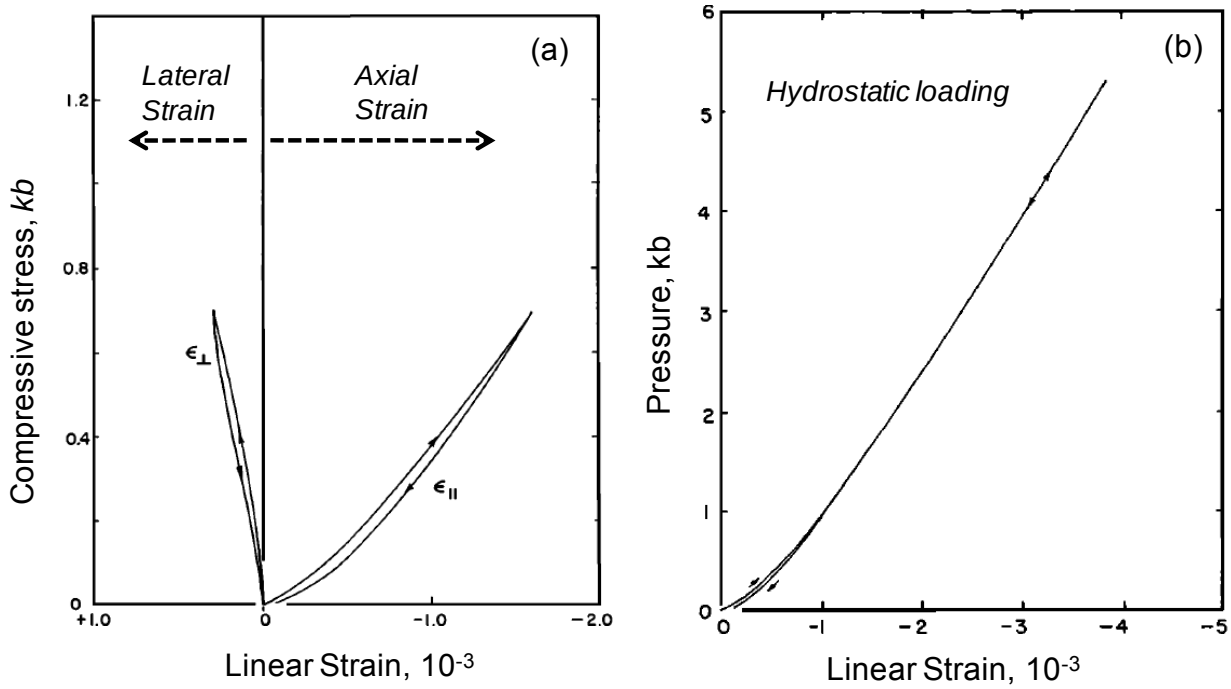

Figure 1.4: (a) Axial and lateral strain under uniaxial compression of Westerly Granite rocks. (b) Linear strain of the same rock under hydrostatic pressure[7]

From the above discussion on the mechanical behavior of rock, it becomes clear that the layered microstructure of rocks with embedded microscopic defects cause the anelastic response in its stress-strain behavior. Thus it may well be expected that a layered system similar to rock containing cracks might respond anelastically upon external loads.

1.2.2. Bones and Nacre

Apart from rocks, there are many other classes of materials and composites which evolve in nature following a layer-by-layer material growth. Materials such as nacre (mother of pearl) and Bone are a few of many such examples. Due to their unique assemblage of layers, the properties of both nacre and bone have been a subject of intense research for many decades and are being considered for devising future materials to mimic their extraordinary properties. These natural materials are known for their unique anelastic properties correlated to their layered structures.

Nacre, also known as the mother of pearl, is a product of biological formations on an inner shell layer in mollusks[8]. These brick-mortar like structures are composed of alternating mineral (Aragonite, one of the crystallographic forms of $CaCO_3$) and organic (protein and polysaccharide) layers with an overall composition of 95% and 5%

respectively [8, 9]. Its stiffness is in the same order as, while its strength is 2-3 times higher than, that of its major constituent Aragonite. With a fracture toughness 3000 times higher than that of monolithic mineral , these structures have provided deeper insights into layered structures to the research community.[10]

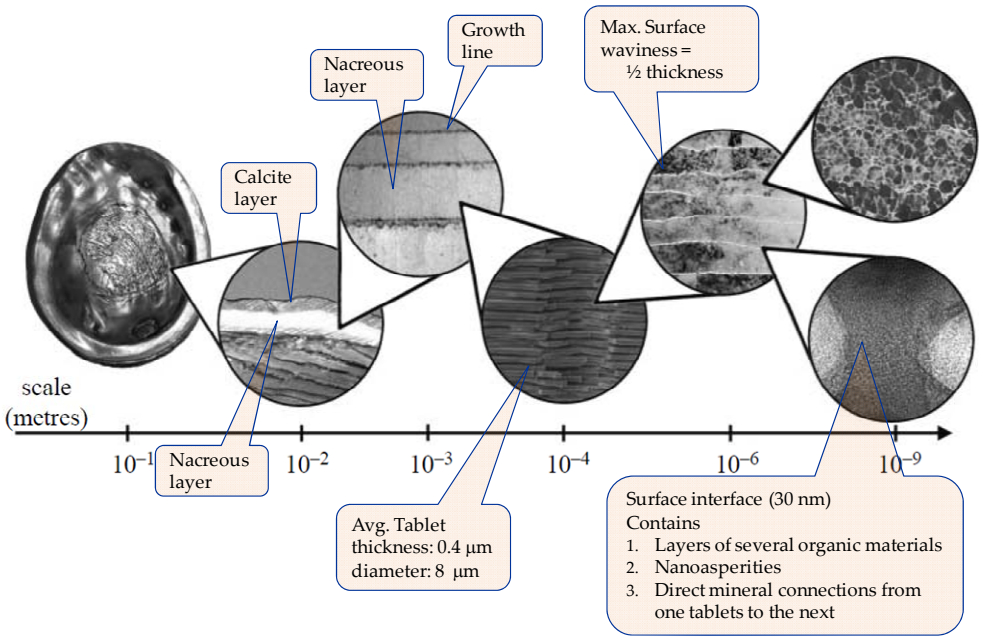

Figure 1.5: Hierarchical structure of nacre over several length scale present in red abalone shell[11]

There are six different kind of nacreous structure present in nature; however the one with the greatest fracture toughness is called "sheet nacre", which is a brick-mortar assembly of polygonal aragonite platelets and thin biopolymer layers.[12, 13] Interestingly, these materials exhibit a hierarchy of layered structure (Figure 1.5)[11], which means a different type of layered structure can be observed at different length scales. These fine structures, from mm range to nanometer range, protect the animal from any external impact. The thick outer calcite layer is hard and brittle which requires a lot of energy to fracture, and the nacreous structure underneath is capable of dissipating energy through large inelastic deformations.

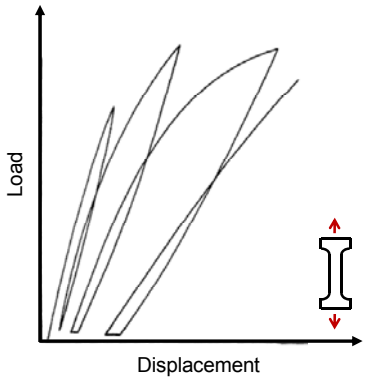

Figure 1.6: Copy of an oscilloscope trace of the load displacement curve of a pearl oyster under a cyclic uniaxial tensile loading. The strain relaxation was observed while the specimen was allowed to relax for one minute between loadings.[14]

Figure 1.6 shows the stress-strain curve of nacre under uniaxial tensile conditions. A couple of interesting observations were made by Currey in 1986 on this anelastic response of nacre[14]. It was observed that, upon loading, the nacre initially shows a non linear response but when the loading direction/condition is reversed the curve does not follow the loading path .Moreover the curve did not reach the initial position at which the loading was started. The fact that residual deformation ceased to exist after a few minutes of complete unloading confirms that the structure is capable of undergoing anelastic deformation. This anelasticity seems to be larger for larger values of strain. The actual numbers on the plot axes were not provided; nevertheless it is the shape of the curve which is of greater importance here. Among all the mechanisms responsible for this interesting behavior, the dominating one is the shearing at the interface. The polymer can stretch up to large strains without losing the bonds between surrounding platelets. Once the polymer is stretched to a certain extent, the deformation is inelastic and there remains a residual strain in the system, which can only be recovered up to a certain percentage.

Similar to nacre, bone is also a high performance biological layered material, which consists of a mineral (hydroxyapatite $Ca_5(PO_4)_3OH_3$) and a soft material (collagen)[11]. As with a nacreous structure it is organized over several length scales. Figure 1.7 shows the six to seven level hierarchical layered structure of the bone. Nanoscopic mineral crystals are embedded into collagen fibrils, and the three dimensional arrangements of these fibrils dictates the bone strength. The collagen fibre, which is the building block for the larger structures: lamellae and osetons, is formed by self alignment of the collagen fibrils[11].

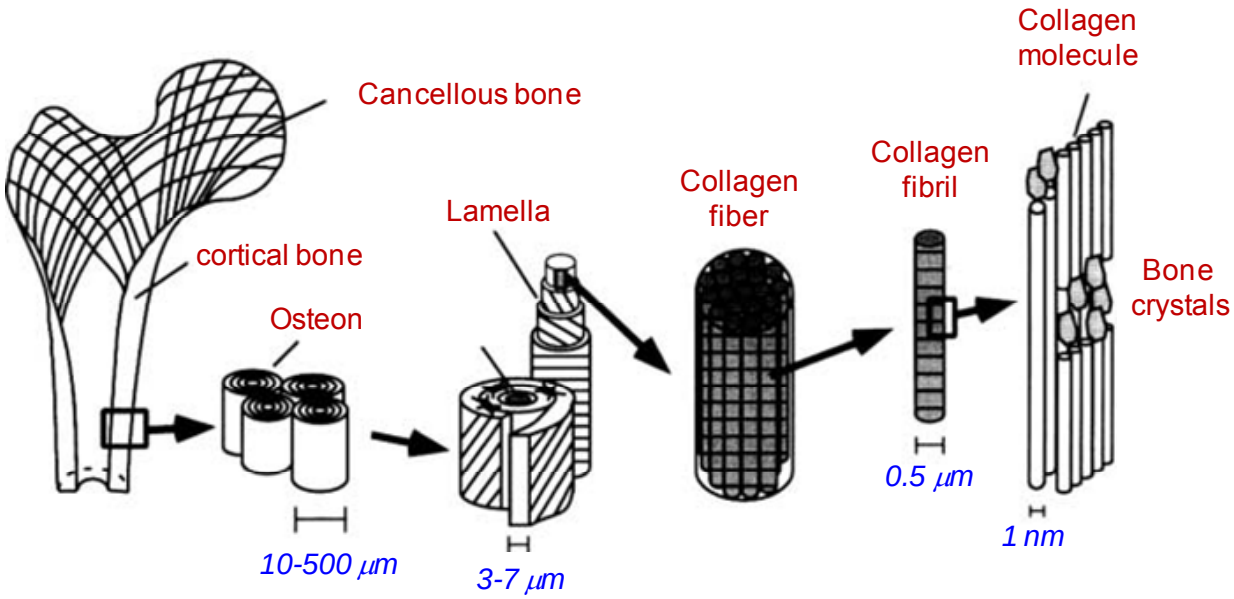

Figure 1.7: Schematic representation of hierarchical structure of bone[15].

Figure 1.8 shows the anelastic stress-strain response of trabecular bone with an image of porous trabecular structure in inset[16]. This type of bone structure consists of a mesh of interconnected spicules (shown by arrows in figure 1.8 inset), known as trabeculae, which are filled with bone marrow. When compressive stress is applied, the trabeculae collide and compress into each other, which reduces the bone-volume fraction due to the reduction in porosity. As a result the material starts to stiffen resulting in temporary load tolerance by the trabecular structure. Here we are only focusing on the layered structure and the anelasticity of the bones.

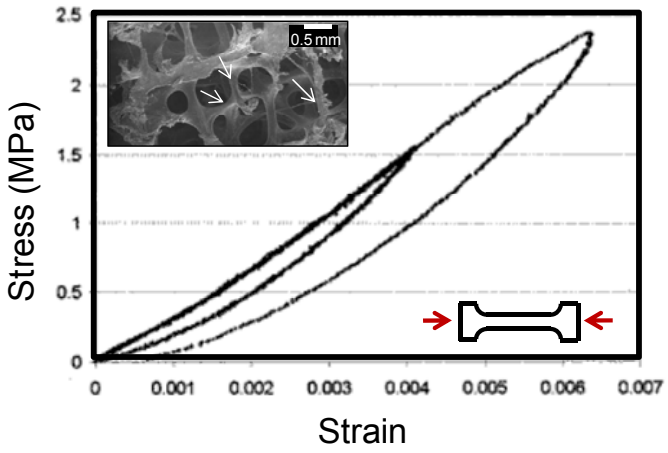

Figure 1.8: Experimentally measured stress-strain behavior of a trabecular bone under uniaxial compression[16]. Inset shows the SEM image of the trabaculae mesh structure with arrows pointing to the trabeculae.

From the above discussion, one can visualize that the sources of anelasticity in the bone are porosity and the inter-lamellar characteristics of the layered material. The extraordinary mechanical properties exhibited simultaneously, such as high fracture toughness and strength of the self assembled natural materials, is due to the layered stacking of these fine structures.

1.2.3. Plasma sprayed ceramics

Recent work has shown that plasma sprayed ceramic coatings show anelastic behavior akin to those observed in layered structures. Figure 1.9 shows the anelastic response of a plasma sprayed (PS) ceramic (yttria stabilized zirconia (YSZ)) coating under uniaxial compressive loading conditions[17]. Although, the response is very similar to those observed for other layered materials (discussed above), unlike bones and rocks, the ceramic deposit becomes compliant as the strain is increased. In other words, the slope of the curve gets smaller at higher strain values.

Experiment for Figure 1.9 was conducted on a hollow dog-bone tensile test specimen with a cylindrical cross section. The specimen was prepared by depositing a thick plasma sprayed YSZ coating on a substrate. Later, the substrate was etched using appropriate chemicals with no change in coating chemistry. The stress-strain curve of the coating clearly shows a non-linear as well as hysteretic response, collectively referred to the anelastic behavior[17]. The first loading-unloading cycle was completely different from the others, and it brought the coating to a residual strain state. The

subsequent cycles were highly repeatable with no residual strains. The response seemed to be slightly different as the number of cycles increased.

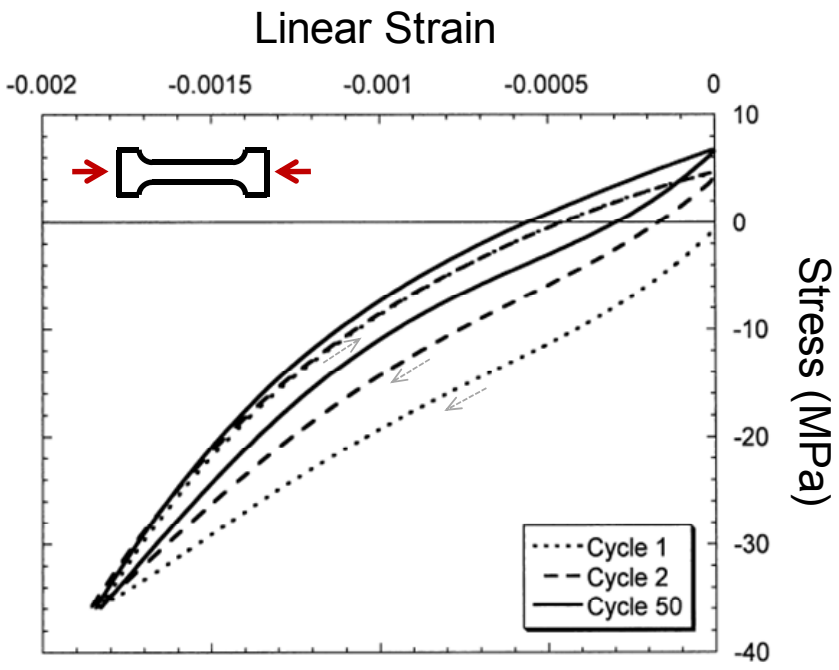

Figure 1.9: Stress-strain relationship of a cylindrical dog-bone tensile specimen under 1st, 2nd and 50th cyclic compressive loading. Note that the response during first cycle is different than others.[17]

Similar observations were presented by Choi et al, where the coated specimens were loaded under three different kind of loadings such as tensile, compressive and bending[18]. Figure 1.10 shows those results. The details of the specimen dimensions are provided in reference [18].

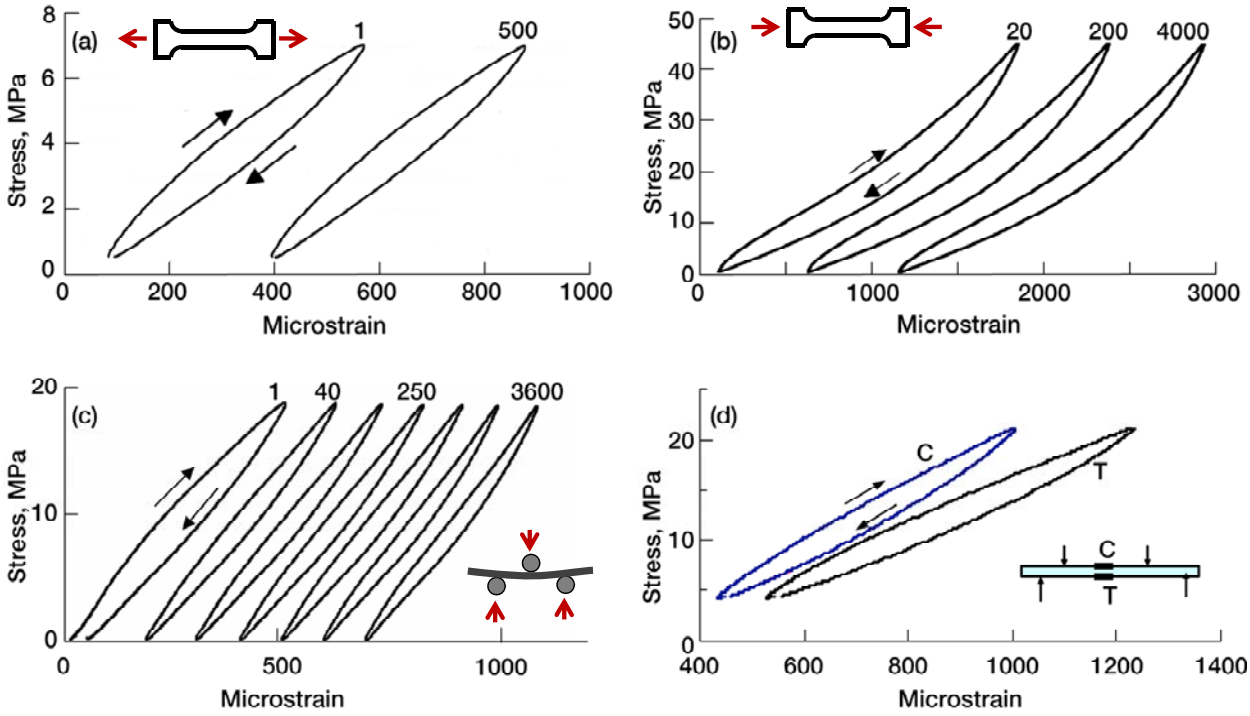

Figure 1.10: Figure 1.10: Stress-strain relationship of PS YSZ coating under different mode of loading. Note that the difference in mechanical behavior of the coating under compression and tension are anelastic and slightly different[18]

Clearly, similar to results shown by Rejda et al.[17] for compression, the anelastic behavior can be observed in coatings under other loading conditions too. The residual strain observed during first cycle suggests some kind of relaxation in stresses developed during the deposition. It is also important to note that after first cycle the coating appears to produce no discernable residual strain in an individual loading-unloading cycle. However the infinitesimal residual strains add up to a significant value after several loading.

Similar results have been reported by many other researchers observing the non-linear response of the thermal sprayed coatings. Kroupa et al proposed that under sufficient compressive load, crack faces are closed and the coatings exhibit higher apparent stiffness while opened cracks under tensile state produce more compliant response[19-21]. The nonlinear behavior of plasma sprayed $ZrSiO_4$ coatings were also observed by Harok et al under four-point bend tests[22]. The mechanical behavior is elastic because ceramics generally do not exhibit plasticity at room temperature. Similar phenomenon was found by Eldridge et al that plasma sprayed YSZ coatings exhibit nonlinear elastic behavior and that the modulus increases with applied stress because of coating compaction[23]. Another bend test combined with strain analysis by Wakui et al reported increasing in-plane stiffness of YSZ coatings with compressive stresses while

decreasing stiffness under larger tensile stresses[24]. They further reported the nonlinear stress-strain responses of plasma sprayed zirconia coating using the laser speckle strain-displacement gauge. Non-linear stress-strain relation of thermally sprayed metallic Ni–45Cr coating was also reported by Wang et al under tensile loading of the specimen along the through-thickness direction[25]. They attribute the non-linearity of the coating to its lamellar features.

The anelastic response of the PS YSZ coatings results was investigated in detail by Liu et al[26]. In their experiments, the specimen was prepared by depositing a thin PS YSZ coating on one side of an aluminum substrate, to generate the thermal mismatch stresses between coating and substrate under temperature change. The size of specimen (9″ x 1″) allowed an in-plane curvature change of the deposited beam, and the curvature (κ) and temperature (T) relationship was obtained. Later the relationship was converted to the stress-strain plot. Figure 1.11 shows the $\sigma - \varepsilon$ curve obtained from such experiment.

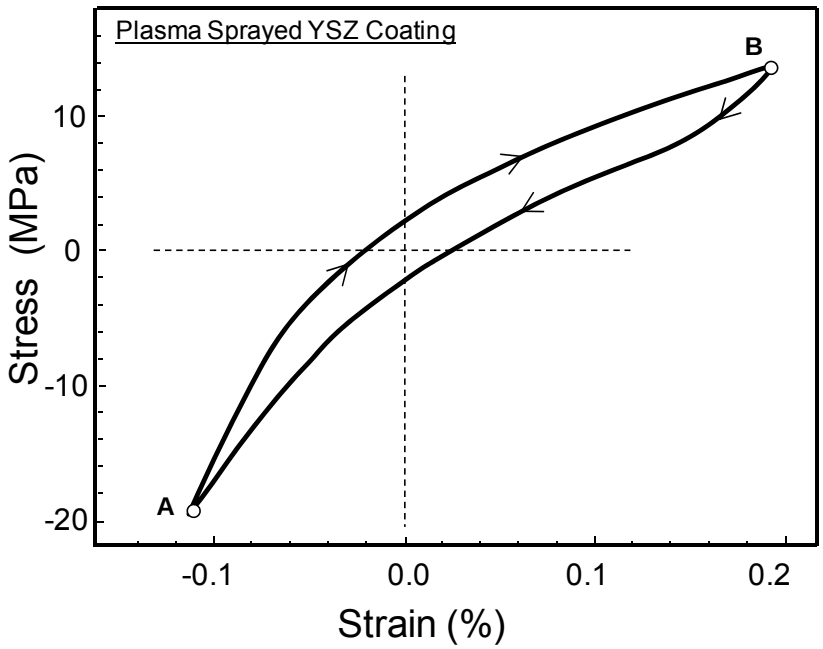

Figure 1.11: Stress-strain relationship of PS YSZ coating sprayed on one side of Aluminum plate obtained from $\kappa - T$ response of the specimen during a heating and cooling cycle. Point (A) corresponds to start of the heating and point (B)[26] that of cooling

The coating is initially under a state of compression after deposition. As the coated specimen is heated, thermal mismatch stresses arise due to the difference in the thermal coefficients of the coating and the substrate materials, which takes the coating from compression to tension. Once the system reaches a certain maximum temperature,

corresponding to the max tensile stress, it is cooled to the start temperature and the system returns to its initial stress state. The coating behaves non-linearly during both the heating and cooling phases, and the stress-strain curve exhibits hysteresis in it.

The above discussions have provided sufficient evidence of the presence of anelastic behavior in PS YSZ coatings although its extension to other sprayed materials is unclear. In order to understand the mechanisms governing anelasticity, an enhanced understanding of the microstructure and its linkage to processing is required. In the following discussion we will first briefly investigate the coating deposition process and its microstructural evolution. Later the underlying mechanisms for anelasticity will be discussed.

Coating deposition by spraying molten particles on a desired surface has been around for a long time, and is known as thermal spray[27]. In general, plasma spray, one of the branches of thermal spray technique, is a semi-continuous melt-spray process in which materials in their powdered forms are heated or melted and accelerated to high velocities towards the substrate[28] (Figure 1.12). The momentum and heat to these particles are provided by thermal plasma[28]. The complex brick-wall architecture of thermal sprayed coatings is developed due to semi-continuous process, particles flattening and rapid solidification of particles. At the first impact on the substrate, the solidification rates of 10^6 K/Sec result in solidification of molten or semi-molten particles with an average grain size from tenth of micrometers to couple of nanometers[29-31]. Here each individual flattened and solidified particle is referred to as a *"splat"* (Figure 1.13(a)), and these splats are the building blocks of any thermal spray microstructure. [32]. Depending on the ambient conditions, the depositing as well as the deposited splat may acquire other impurities or undesirable changes in terms of phase change, vacancies, oxidation and reduction. Additionally, metastable phases can also be formed introducing amorphicity and highly supersaturated phases. Finally, the deposit shrinkage due to high rates of solidification can also introduce residual stresses in a coating which can affect the coating properties in many ways [30, 33]. The final coating developed from successive impingement as well as inter-bonding among the splats, consists of different kind of defects such as interlameller pores, cracks and globular pores .These are associated with the splat and their neighboring splats (Figure 1.13(b))[34].

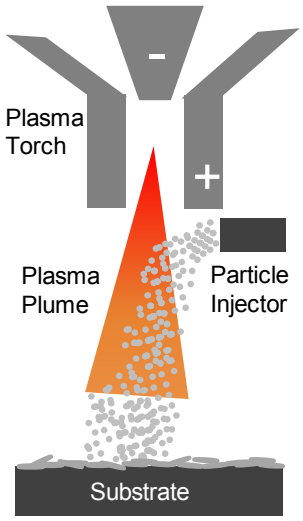

Figure 1.12: A schematic of plasma sprayed process and coating formation.

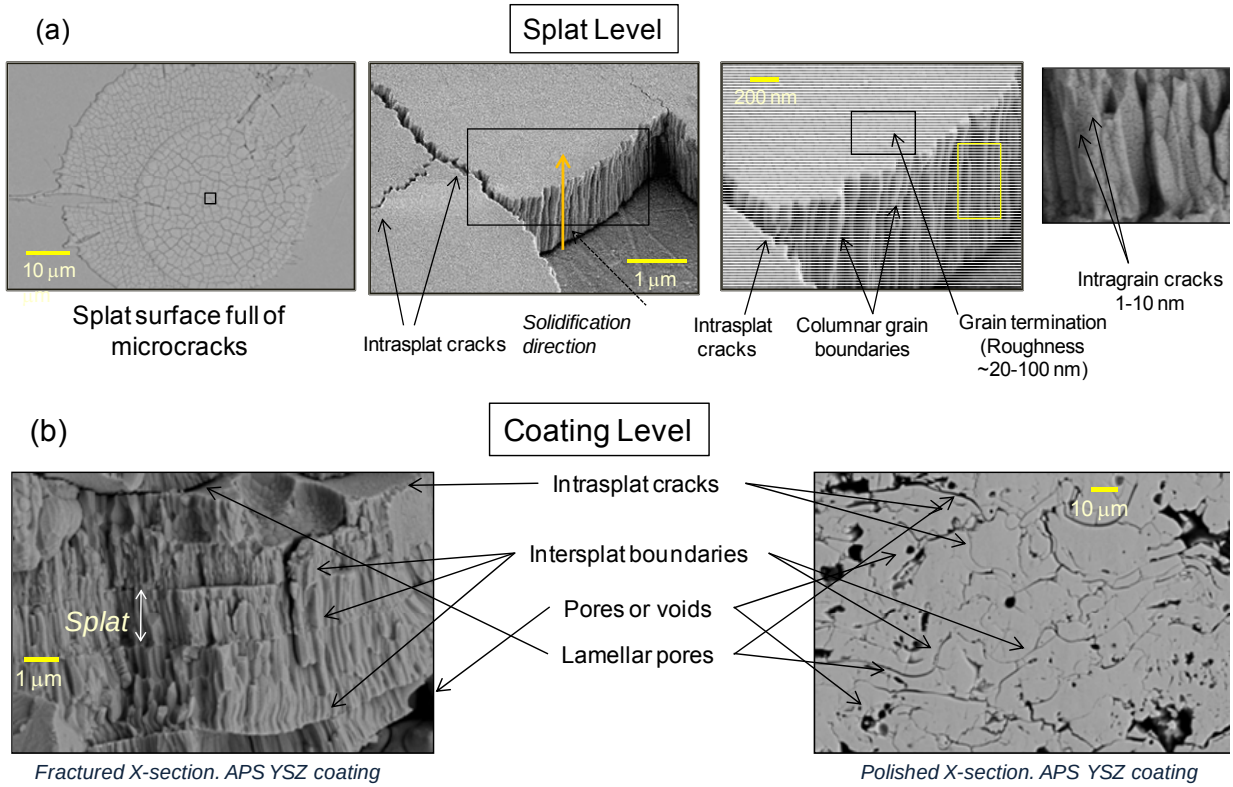

Figure 1.13: (a) microstructural details of a single splat. (b) detailed characterization of different types of defect in a fractured as well as polished cross sections of a PS YSZ coating.

Figure 1.13 (a) shows the hierarchy of sub-structures within a single splat. The molten particle, coming in contact with a relatively cooler substrate or pre-deposited particles, solidifies and cracks as a result of relaxation of large quenching stresses produced by rapid solidification of spray particles [35, 36]. Upon observation at a higher magnification, those cracked walls exhibit a columnar grain growth along the direction of heat flow, which is from the substrate or the pre-deposited layer to the free surface of the newly deposited splat. The average grain diameter is generally between 20-100 nm range[37]. At even higher magnification, these single columnar grains also show the presence of some cracking within a grain.

Figure 1.13 (b) displays fractured and polished cross sectional images. The former one explains the coating evolution by layering of splats; the latter provides an idea of the dimensions of these defects present in the coating. The figure also indicates the different classes of defects in the coating, such as inter-splat boundaries, globular pores, interlamellar spacing, and the intra-splat cracks. Two different splats, when in close contact, share an inter-splat boundary. These boundary surfaces with significant openings are referred to as interlamellar spacings. With even larger opening dimensions, they are also considered as interlamellar pores. Generally these defects are irregular and are in the in-plane direction of the coatings. Another class of defects in the coating are the globular pores which are either spherical or elliptical. These defects are generated due to either contraption of air pockets or the un-compacted free space surrounded by unmolten or partially molten particles. At smaller length scale, the intra-splat defects, such as cracks in a single splat, columnar grain boundaries and cracks in columnar grain, exhibit another class of defects in a coating. In short, one can conclude that a PS ceramic (YSZ) structure contains a variety of morphological defects ranging from nanometer to mm length scale.

The defect architecture governs the overall properties of the coatings, and these defects are prescribed by characteristics of feedstock materials, processing parameters and the deposit formation dynamics. A great amount of work has been done in the past to characterize these defects and correlate them with the coating properties, such as conductivity, toughness etc [34, 38-48]. Understanding the interplay of the defects can provide sufficient insights into the coating properties, and hence can enable a better tailoring of microstructure by controlling the processing inputs.

The anelasticity in PS ceramics can mainly be attributed to either phase transformation in the deposit materials or geometrical and microstructural conditions of the coatings. Excluding the possibility of the former phenomenon, the relative movements of the embedded defects can be used to dictate the anelasticity in PS

ceramic coatings. Many researchers have shown evidences of such relative movements (Figure 1.14).

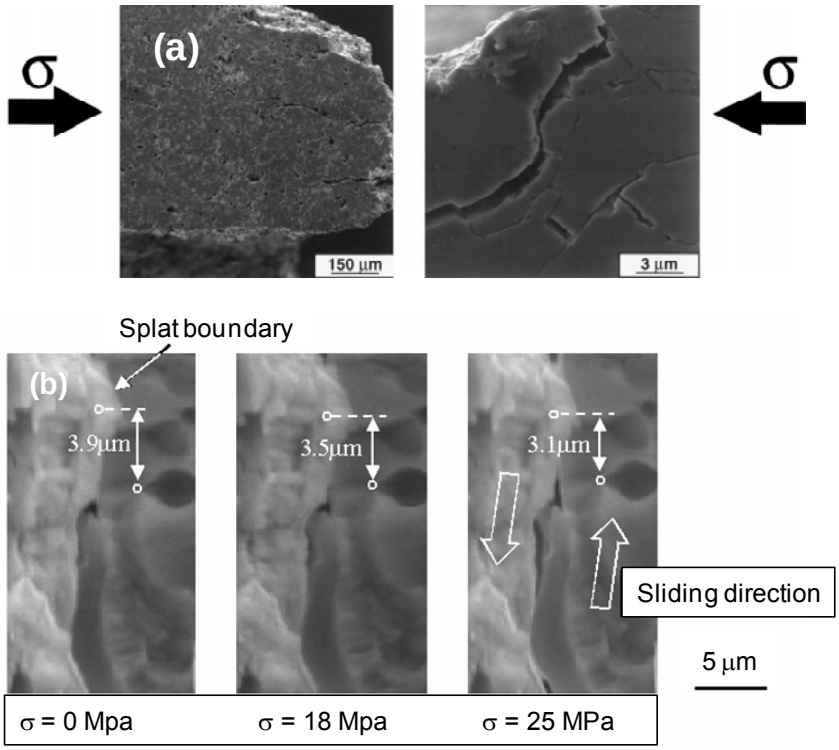

Figure 1.14 : (a) sliding of splat interface upon compressive loading[17]. (b) *in-situ* measurement of relative displacement of a pore and evidences of interfacial sliding of splats under different stress magnitudes[49].

Figure 1.14 (a) shows the moved splat interfaces of a thick PS YSZ coating under compression. The corresponding stress-strain results have been discussed earlier in this section[17]. Similarly, Figure 1.14 (b) shows the measurement of relative displacement on flexural bending preformed with the *in-situ* SEM characterization of the microstructure of a free-standing YSZ coating[49]. It can be seen that the pore displacement, with respect to a fixed point, changes (decreases in this case) with stress magnitude. Additionally, at higher stresses the sliding of splat at defect interfaces was observed. One interesting conclusion can be made from these observations. Some classes of defects such as pores start responding to its surrounding stress state right from the beginning of loading, while on the other hand, some of the other defects require certain stress magnitudes before they start to be displaced. It is important to note that the images shown in Figure 1.14 belong to the inelastically deformed coatings under large stresses; however it is highly possible that under relatively reduced loading condition these effects (sliding or movement of defects) are capable of introducing anelasticity in the structure, which means that they move back to their original state if the load is released.

Figure 1.15 displays a schematic of a defect architecture closely resembling a PS YSZ coating[50]. The two different mechanisms are also shown in the figure. One of them is the opening/ closure of microcracks and pores, which provide some degree of "softening" to the structure. This also explains why the overall elastic modulus of a PS YSZ coating (10-40 GPa) is lower than it's bulk value (206 GPa). Additionally, the same mechanism can also be used to explain the non-linear stress-strain behavior of a coating under compressive or tensile loading. The other mechanism can shed some light on the hysteretic response of the coatings under cyclic loading. The sliding of interfaces and closed cracks can cause some energy dissipation in a complete loading-unloading cycle, which causes the coating to exhibit a hysteretic behavior.

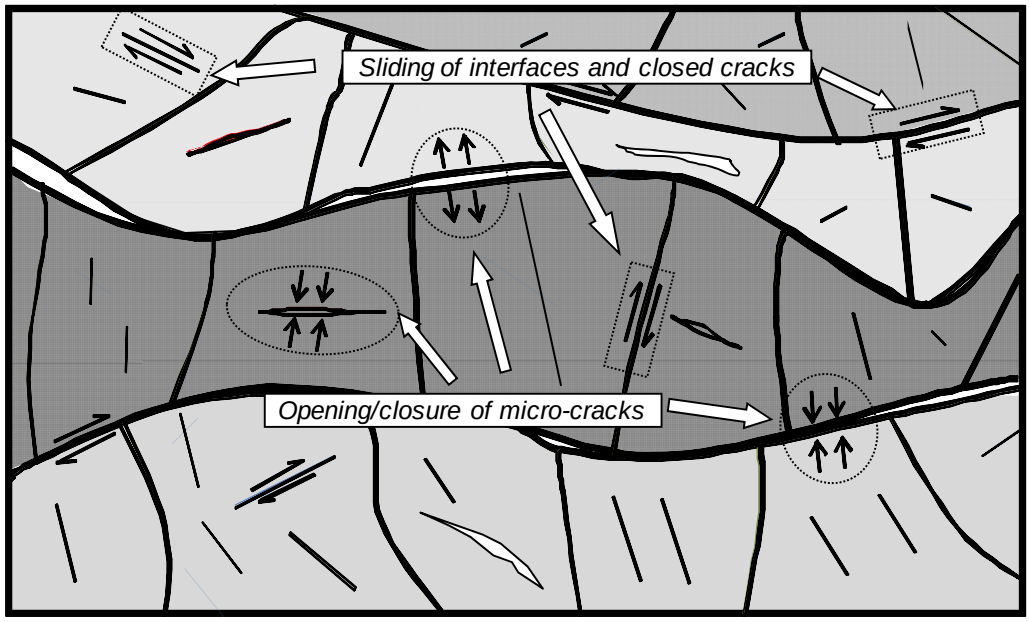

Figure 1.15: A schematic representation of the two mechanisms responsible for anelasticity in plasma sprayed coatings[50].

From the two proposed mechanisms, it can be extrapolated that the density of each defect category controls the overall anelasticity. Therefore, it can easily be hypothesized that this novel behavior of PS ceramic coatings can be regulated by tailoring the coating microstructure by tuning the process inputs. This dissertation attempts to provide an enhanced understanding of the anelasticity phenomenon which enables the process controlled modification of the anelastic behavior as a tool for enhanced coating design and performance.

2. Statement of the problem

Plasma sprayed ceramic coatings contain a myriad array of defects, which dominate the physical and functional properties of the coatings. The detailed investigation of their microstructure reveals that these defects, such as columnar grain boundaries, interlamellar pores or spacing, globular pores etc, range from a nanometer to sub-millimeter length scale. The properties of coatings are very sensitive to the defect architecture. Additionally, the local variability in coatings microstructure within a coating can introduce some variability associated with the measurement of a particular property. This implies that the measured property at one location of a coating could significantly differ from the measurement on another location. Moreover, due to the random orientation of these defects it becomes extremely difficult to predict or simulate properties coatings

Despite the complexity the defective microstructure does provides numerous useful attributes to the coatings characteristics and consequently properties. For example, the interlamellar pores/spacing contributes to lower thermal conductivity of a sprayed material as compared to their bulk counterpart. Furthermore, the opening-closure of the defects introduces "softening" of the structure during mechanical loading, which imparts compliance when subjected to thermo-structural and mechanical strains. It has been observed that the compliant characteristic of the coating exhibits its non-linear stress-strain relationship under different type of loadings, such as uniaxial tensile, biaxial flexural loadings.

Recent observations on the non-linear behavior of plasma sprayed YSZ (ceramic) coatings by Nakamura et al, provided a new method to measure and quantify the non-linear elastic properties of the sprayed coatings. In temperature excursions, the coating-substrate system experiences thermal mismatch stresses resulting in a change in curvature of the bi-layer assembly. The curvature-temperature relationship of these coatings can be processed to estimate the non-linear stress-strain behavior of the coatings, which provides two useful parameters, E (elastic modulus) and ND (degree of non-linearity) which in turn provide characteristic description of the coatings. Here E is the elastic modulus of the coating in its linear region, while the ND is the measurement of departure from linearity in the non-linear part of the stress-strain response of a coating. Apart from other techniques commonly used to calculate the stress-strain

behaviors of materials, such as indentation, uniaxial tensile or compressive loadings etc, the bi-layer curvature-temperature (BCT) measurement technique allows simplicity in specimen preparation and the properties can be measured directly for the sprayed coating on a substrate. The BCT measurements enabled a direct comparison among coatings with different defect architecture. One of the advantages of the technique is that it measured the response of a coating over a large sampling area, which minimizes the variability associated with the local architecture of the coating.

Though, the measurement technique was proven as a useful tool to compare different coatings, the sensitivity of the measurement technique and its relationship to processing and microstructure is the next major challenge in this arena. This is one of the primary research interests for this dissertation. Additionally, one of the chronic problems associated with the plasma sprayed coatings is their repeatability/reproducibility, which are influenced by several factors, such as plasma torch conditions, ambient conditions during spraying, deposition pattern used for deposition and many more. Having examined the sensitivity of the non-linear parameters, a study was conducted on the assessment of repeatability of coatings sprayed with geometric and temporal variations. This investigation provided the evaluation of intrinsic variability among simultaneously processed coatings. Finally, the study also addressed the reproducibility of plasma spray process at different periods.

With modifications and enhancements to the substrate curvature measurement technique (BCT), it was observed that the plasma sprayed ceramic coatings additionally exhibit a hysteretic stress-strain response. Collectively, a non-linear and hysteretic response is referred to as anelasticity of a coating. The mechanism behind hysteretic behavior is attributed to energy dissipation due to the frictional sliding within the defect (splat interfaces and cracks) surfaces. A single crack model proposed by Liu et al confirmed that the crack orientation and the opening between its faces can significantly affect the overall anelasticity of the material. This provides an approach to control the anelasticity by tailoring the defect types and architecture by tuning the processing conditions. One of the sections in this dissertation focuses on controlling the anelasticity by changing the processing conditions by various means, such as spray distance, plasma enthalpy, and deposition patterns. The purpose of the study was to acquire different densities of various types of defects and their dimensions, which will broaden our understanding as to how the anelasticity of coatings can be controlled.

The interface roughness among the assembled splats can affect the sliding friction among the interfaces. In a crystalline splat, the splat surface appears to be significantly rough due to the columnar grain terminations, which can impart sufficient frictional energy loss at the sliding sites between two splats. This suggests that controlling this

roughness can provide an approach to alter the hysteretic response in a coating. For example, if the deposited splat is amorphous, the splat surfaces will be smooth due to lack of columnar grain terminations. Moreover, in crystalline coatings the frictional properties of defect surfaces can also be altered extrinsically by introducing another media at the sliding sites. This set forth a number of interesting questions: How significantly can the anelasticity be controlled by changing the surface roughness? Would it be depending on the crytallinity of deposited coatings? Up to what extent the presence of foreign media at the sliding surface can alter the anelasticity of coatings? This dissertation attempts to answer these questions using material selection and design of experiments.

The BCT measurement requires heating of a coating-substrate system, which introduces the temperature factor associated with the properties extraction. Though the temperature change during the measurements is in the range where any physical or chemical alteration in the coating properties is not possible, the change in mechanical properties of substrate material cannot be ignored. This raises a question whether the anelasticity phenomenon can be observed at room temperature conditions under purely mechanical loading situations. In order to investigate this aspect, the four-point-bend test method was adapted. This type of loading also provides bi-axial stress state in coatings similar to the case of thermal loading under BCT measurements, which enables a direct comparison of coatings' behavior under two different types of loading.

As discussed in chapter 1, the naturally layered materials such as rocks, bones, nacre exhibit anelastic behavior akin to that observed in spray deposits. Especially, the microstructural observation of nacreous materials reveals a "brick and mortar" arrangement comprising of inorganic structural platelets adhesively bonded with polymers, which is comparable to that of brick-wall splat structure of plasma sprayed coatings. A careful examination of the microstructures of these materials reveals that the layer characteristics governing the anelasticity in nacre as well as spray deposits are significantly similar. Given that the nacreous structure contains a polymeric media which serves as mortar to the brick-mortar arrangement, the plasma sprayed ceramics, on the contrary, exhibits intrinsic anelastic behavior without any presence of a tougher phase. Will the introduction of polymer into the ceramic coatings alter their mechanical properties? A preliminary study is conducted as an attempt to investigate the effect of polymer presence on anelasticity of the plasma sprayed YSZ coatings.

3. Experimental procedures

3.1. Coating Deposition

3.1.1. Plasma spray process

3.1.1.1. Plasma generation

A typical thermal plasma used for plasma spraying is set up using a direct current which generates a stable and non-transferred arc between the water cooled electrodes, named cathode and anode, of the torch (Figure 3.1)[51]. The cathode and anode are made out of tungsten and copper metal respectively[52]. For most of the coating depositions, vortex plasma was used; which was generated using F4-H2 torch (Sulzer Metco, Westbury, USA). The arc gas, a mixture of an inert gas such as Ar or N2 and a few percent of enthalpy enhancing gas such as Hydrogen, is introduced from the back of the torch interior. The gas swirls in a vortex due to design of the torch and exits out at the end of anode. The electric arc generated from the cathode to the anode completes the circuit, and an axially rotating plasma flame, due to the vortex momentum of the gases, forms at the outer face of the anode. The enthalpy of a given plasma plume is regulated by the flow rate of input gases, and the plasma velocity is mainly controlled by nozzle diameter and arc current. Depending on the material to be deposited, the arc gas composition can be changed from pure inert gas (Ar and N2) to other combination of it with He or/ and H2[53]. Any arc gas mixture has either of the heavy gases Ar or N2 to provide adequate momentum in the plume without increasing the arc current, and H2 and/or He are used to enhance the enthalpy transfer to the particles.

3.1.1.2. Powder feed

Due to the high temperature of the plume (up to 10,000K), the powder is fed externally into the plasma plume instead of other modes of injections, such as axially with the flame used in other thermal spray processes. For our studies, the required powder was fed using Plasma Technik Twin 10 feeder, and was externally injected to the plume from the top radial position. A carrier gas, Ar in this case, was used to provide the required momentum to the particle in order to have them flow into and

then along with the plasma plume. It is important to know that for different feedstock materials and powder feed rate, the carrier gas flow rate is very critical to achieve maximum number of particles being carried away with the plasma plume. A lower or higher flow rate of carrier gas than its optimum value can lead the powder to under and over injection respectively (Figure 3.2). It has been reported in the past that at this optimized condition the particles temperature and velocities (T &V) are maximum for the given set of other plasma input parameters. The procedure of achieving optimum injection is referred to as "injection optimization"[54]. For all the coating deposition process the injection optimization procedure was exercised.

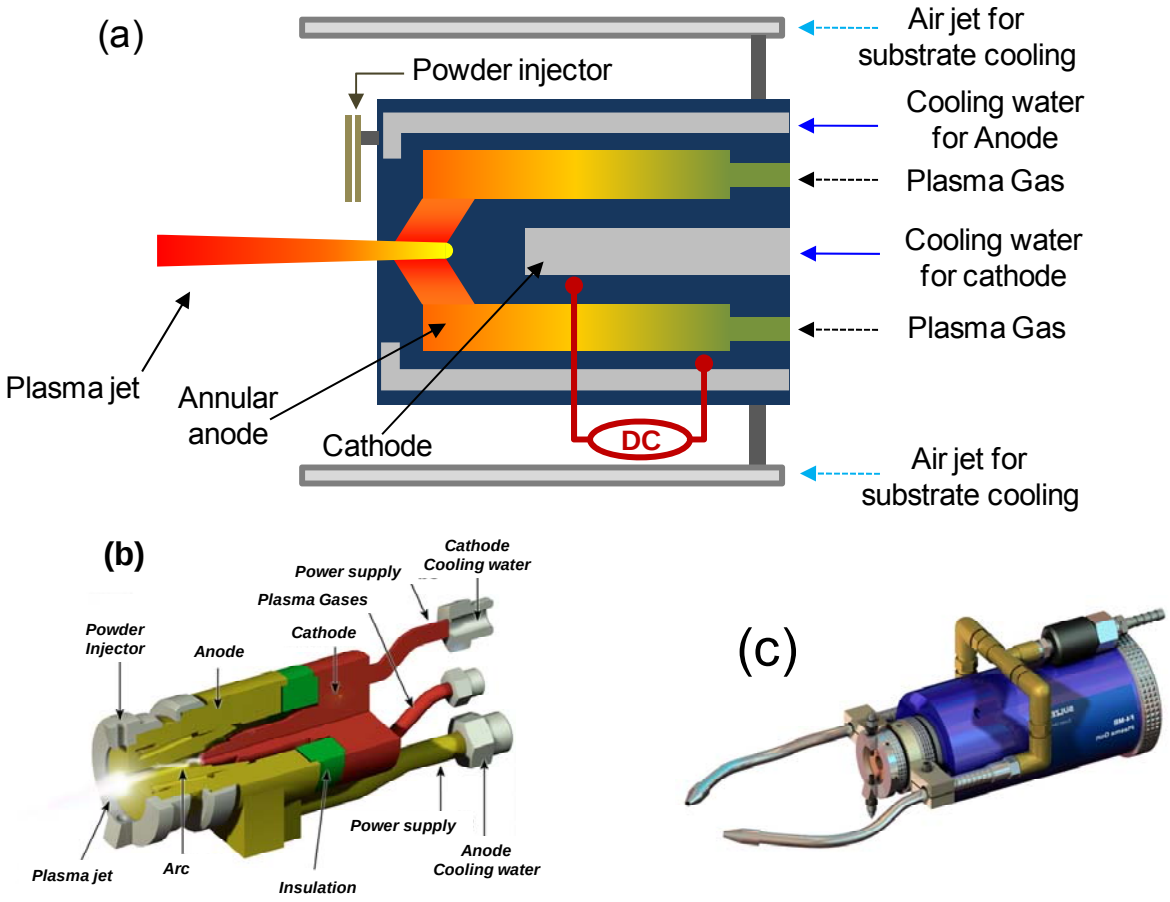

Figure 3.1: (a) Schematics of plasma spray torch. (b) cross sectional drawing showing interiors of the torch and (c) the F4 SULZER plasma spray torch.

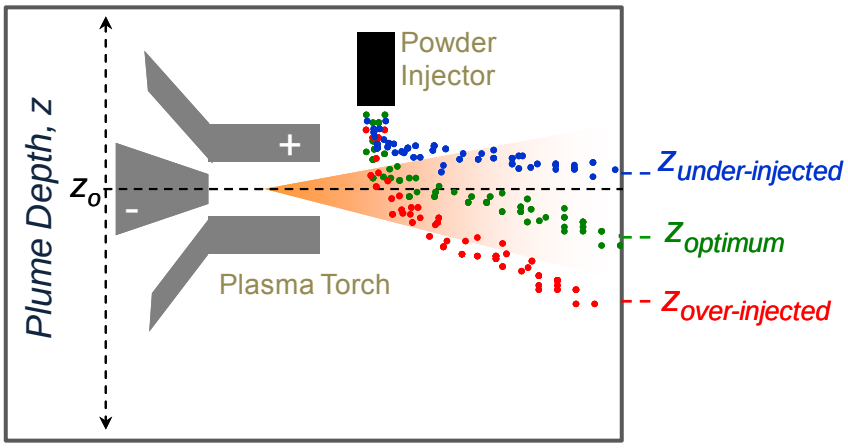

Figure 3.2: Illustration of "injection optimization" procedure. At optimum injection condition particles achieve maximum temperature and velocity.

3.1.2. Coating deposition

3.1.2.1. Particles diagnostic (Temperature and Velocity)

Prior to the actual coating deposition, the input parameters for plasma, i.e. Current, Argon flow rate and H_2, and those for powder feed, feedrate and carrier gas flow rate, are selected. The details of these parameters are provided separately in each section. Figure 3.3 illustrates the steps used for a coating deposition. The plasma torch was turned on with the robot position- A, also referred as *Home Position*. The powder feed was started and torch was then moved to position- B for the particles diagnostics, i.e. measurement of particles temperature and velocities (T & V). Two sensors were used for this: first was DPV2000 (Tecnar Automation LTEE, Canada), which measures T & V of individual particles, and it was programmed to measure up to 5000 particle counts. For further analysis, the measurement can be plotted as a particle distribution over temperature or velocity or it can be reported as the average numbers of the T & V. Since, all the particles dwelling through the plasma plume are not in the same molten state, it is inappropriate to dictate the particles energy characteristics, T & V, in terms of their average measured values. Hence, their distribution provides the fine details of the number of particles in molten, semi-molten and unmolten states. Nevertheless, the average numbers for T & V are comfortably used to represent the temperature and velocity achieved for a given set of processing parameters.

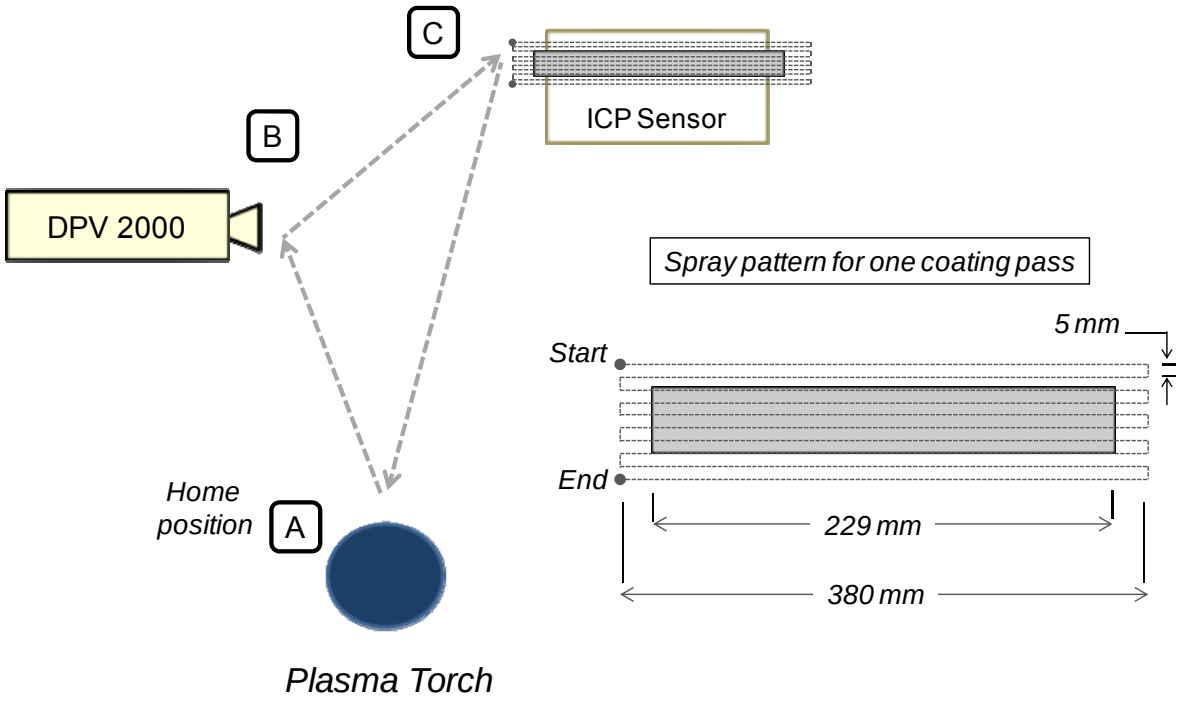

Figure 3.3: Steps involved in a typical coating deposition. The torch raster pattern on coating is also shown on the right.

The second sensor used for the particle diagnostic was AccuraSpray-g3 (Tecnar Automation LTEE, Canada), which performs the measurement on an ensemble of particles, based on the snap-shot of the overall particle plume, and provides the average T & V as an output for that particular condition. The advantage of the second sensor is that it displays the position of the particle plume with respect to the plasma which helps tune the carrier gas flow in order to perform the injection optimization step. It is important to note that the measurement algorithms for these sensors are significantly different; therefore, a direct comparison of average T & V numbers obtained from the two sensors cannot be used. However, for a comparative analysis of the particle diagnostics the measurements made by either of the two can be used. For both the sensors, the powder feedrate is kept at a much lower value (5 g/min) than the required value for the deposition to save the powder. It has been shown in past that the measurements with lower feed rate are similar to those performed with higher feedrates[55].

After the diagnostics the torch is moved to home position (A) again, and powder feed is turned off. This is done to perform the preheating of the substrates. Since, the coating deposit formation strongly depends on the substrate temperature[56]; the preheating is done to bring the substrate closely to the substrate temperature achieved

during deposition. For the preheating process the torch is moved to position- C, and, generally, two to four preheat passes are made depending on the enthalpy of the plasma. The torch raster pattern for the preheating is same as that for coating deposition (Figure 3.3). After preheating, the torch is again brought back to the home position (A) and the powder feed is turned on at its required feedrate for deposition. Again, the torch with powder injection is moved to position- C where it deposits the coating on a prepared substrate mounted on the insitu-coating property sensor (ICP). A detailed explanation on ICP is provided in section 4.2. The details of the deposition pattern are provided later in this section and it was identical for the preheating procedure also.

3.1.2.2. Substrate preparation

All coatings were deposited on flat 9″ (229 mm) x 1″ (25.4 mm) Al6061 substrate. The substrate material as well as dimension was selected based on one of the requirements of curvature measurement both *in-situ* as well as post deposition thermal cycling. The high coefficient of thermal expansion (CTE) of Al, as compared to the depositing materials, leads to a high mismatch of stresses between the coating and substrate systems causing a larger curvature change with change in temperature. To achieve a good resolution in curvature measurements, after a number of experiments, the thickness of substrate was kept between 2.24 and 3.2 mm. The dimension of the substrate (width: length = 9: 1) is chosen to keep the planar stress condition over a large volume of the coating except for edges. Prior to coating deposition, the substrate is cleaned with isopropanol solution to remove any oil residue, and then grit blasted using SiO_2 grit (#24) at 40 psi upto a surface roughness of 3.5-4 microns. This exercise is important to provide a good adhesion between coating and substrate. The substrates were then cleaned again using an air jet to blow away any dust or grit residue remaining after the grit-blasting process. The weight and thickness (at 5 places on the substrate) of the substrate are measured using a micrometer (Mitutoyo Corp.-S/N 293-344) with a resolution of 1 μm and a weighing instrument (Fisher Scientific-A200DS) with a resolution of 1 mg.

3.1.2.3. Torch raster pattern

The torch raster pattern, which was used for most of the coating deposition, is shown in figure 3.3. Total 10 strokes are made to complete one pass, and each stroke was spaced out by 5 mm in the vertical direction. The total raster or stroke length was 380 mm, exceeding substrate size by 75 mm on both sides. This excess movement of torch is required to have a uniform coating deposition. The set of 10 strokes is referred to as a coating pass, and the total numbers of passes are decided based on the coating thickness requirement. In some of the experiments of section 5.4, the raster pattern was

deliberately changed to examine its influence on coating properties; the details are described in that section.

In order to prevent the substrates from overheating, two 40 psi air jets from the two sides of the torch were also used (figure 3.1 (c)). Given that Al loses its mechanical strength drastically beyond 300^{o}C, it is important to maintain low deposition temperatures. Among all the input parameters for plasma as well as powder feed, the stand-off distance (spray distance) of torch from the substrate, its raster speed, and spray angle can also change the coating formation mechanisms. The latter two were kept constant for most of the spraying except for coating deposition in experiments under section 5.3.

3.2. Thickness, weight and curvature measurements

The thickness and mass of substrates measured prior to deposition are subtracted from the post deposition measurements of the coated specimen to get the true coating thickness and weight values. The apparent density (g/cc) of a coating was calculated by simply mass/ volume method (Eq. (3.1)).

$$\rho = \frac{m}{t \times w \times l} \qquad \text{Eq. (3.1)}$$

Where m is the mass of coating in grams, t, w and l are the thickness, width and length of the coating in mm.

Once the specimen is cooled down, there is a residual curvature present in it. This residual curvature is a direct implication of the residual stresses present in that coating. The curvature present in the substrate was calculated by first measuring the depth of the specimen sitting on a flat surface using dial depth micrometer (Compac Geneve), and then fitting those numbers to an equation of circle. The pre-deposition residual curvature in an uncoated substrate was then subtracted from the curvature values measured after the coating deposition. The resultant values can be used to infer the actual gain in curvature due to deposition.

3.3. Free-standing coating preparation

Some of the characterization techniques require the coatings to be in their free-standing (without substrate) form. In order to prepare them, the coatings with substrate are cut to the near net required shape and are then removed from the substrate by dissolving the coated specimens into Aqua Regia (3 vol% HCl and 1 vol% HNO3) for an extended period of time, about 3-4 hours. The substrates' material (Al6061) corrodes away and the free standing coating samples are then thoroughly washed with water. It has been confirmed in past that this dissolution process does not show any deleterious effect to the coatings. Once the coating was in the free standing form it was further ground and polished to the required dimension.

3.4. Thermal conductivity measurements

To prepare samples for thermal conductivity measurements, a free-standing form of coatings with the dimension 15x25.4 mm were prepared. The coating samples were then rounded to disks with a diameter of approximately 12.7 mm and coated with a very thin graphite layer using an Acheson-Aerodag G spray-can. The thermal conductivity was measured by Holometrix Laser Flash Instrument at room temperature[43]. Each sample was subjected to a short laser pulse, and corresponding temperature rise was measured on opposite side. The measurement was also made on the flipped specimen. This practice gives a better average value of thermal conductivity of the coating as there is a possibility of a through thickness gradient in defect density. The instrument first measures the specific heat for a calibration sample, then for the free standing specimens. With an additional input of density and thickness to the software, thermal conductivity of different samples were calculated.

3.5. Indentation elastic modulus and hardness measurements

A small piece of the coated specimen with dimensions 5x7 mm was cut from the curvature beam. The top surface of the coating was polished up to a finish of 3 μm in order to reduce the roughness of coating surface. Depth-sensing indentation method was used to extract the materials properties using the contact response of a small volume of material. Nanotest 600*(Micro Materials Limited, Wrexham Technology park, Wrexham, LL 137YP, UK) instrument was used to perform the experiments. In the

present study, a 1.59 mm (1/16") diameter WC-Co spherical indenter was used with a maximum load of 5N. The maximum loads of each loading-unloading cycle are equally divided between zero and the total maximum load, and a partial unloading to 75% of the maximum load was chosen. Oliver and Pharr method was used to analyze the load-displacement data.[39] For each of the samples, 15 indents were made, and the average value as well as standard deviation of elastic modulus and hardness were calculated.

3.6. Four-point bend (4PB) test

Figure 3.4 shows schematics as well as the picture of the 4PB test setup. The specimen size was kept the same as it was received after deposition. The outer supporting span and inner loading span were kept constant at 120 mm and 60 mm respectively. A laser displacement sensor (SUNX LM10) with a resolution of 1 μm is placed at the center of the setup spotting its laser beam at the bottom of the specimen to measure the mid-point deflection of the beam. The load cell with max load capacity of 500N (least count 0.1N) was attached to the crosshead of the screw-driven machine frame (TIRATEST 26005). The crosshead speed was kept constant at 0.1 mm/min, and the coated specimen was placed such that the coating underwent tension upon loading. To avoid any plastic deformation in the substrate, the maximum load was calculated and set prior to deciding the loading-unloading cycle. Also, a preload of 1.5-2N was also applied to confirm the contacts between loading rollers and specimen. The load-displacement curve was then plotted and analyzed to obtain non-linear parameters of the coating.

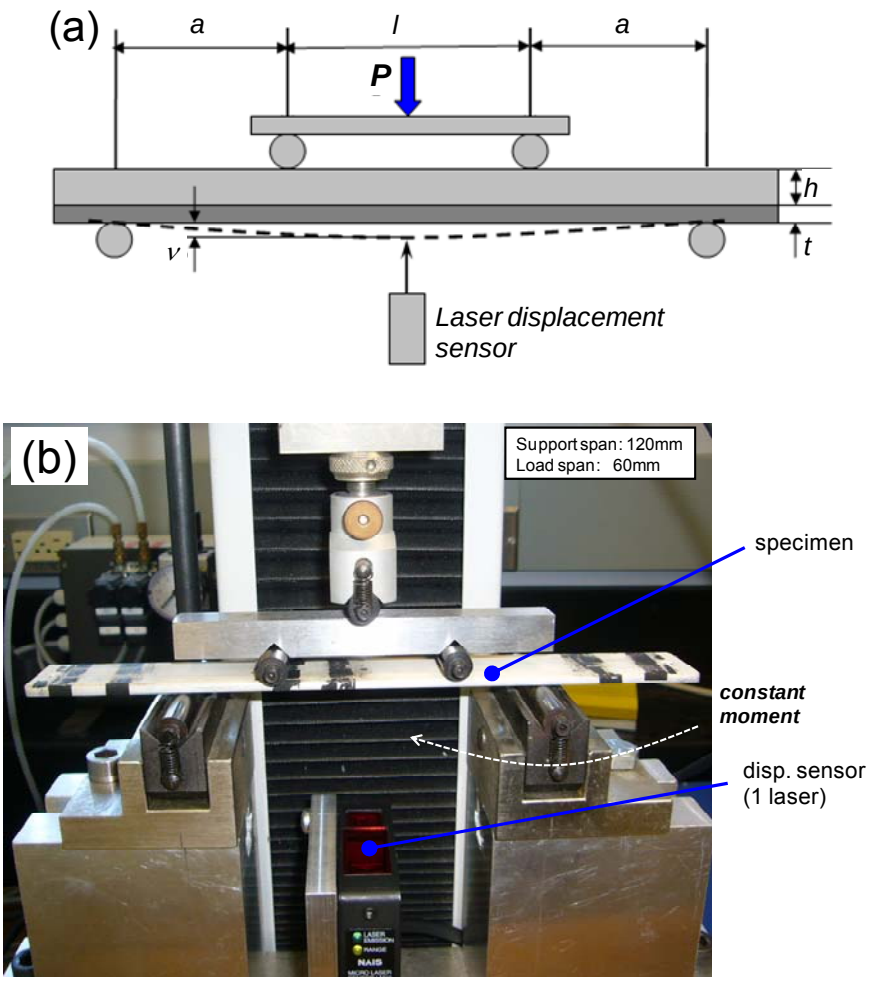

Figure 3.4: (a) schematics of a typical four-point bend (4PB) setup showing the loads and different roller positions. (b) shows the photograph of the 4PB setup[57].

4. Measurement and quantification of anelastic behavior via bi-layer curvature-temperature (BCT) measurements

4.1. Coating modulus and stress calculations based on BCT measurements

Beam curvature measurements have been used extensively to characterize coatings and layered materials especially those present on substrate. The curvature measurement techniques have been used extensively in the electronic industry to characterize stresses in deposited films. These measurements provide information on in-plane residual stresses as well as elastic properties of deposited films. The curvature technique has been adapted by many research groups to examine stress-evolution and residual stresses in thermal sprayed films [58, 59].Of special relevance in the analysis of anelastic behavior are: calculations on residual stresses from beam curvature and extraction of elastic modulus. In the following we will discuss detailed analytical formulations for determining such data from curvature measurements.

4.1.1. Stress calculations

The stresses in a plasma sprayed coating originate from the large temperature differences experienced by the coating-substrate system during the spraying process. When the molten particles come in contact with the layers underneath, they are rapidly quenched. Their contraction is restricted by the adhesion between the particles and the substrate or the pre-deposited layer. Due to the rapid solidification of splats, tensile "quenching stresses" are generated in the coating[33]. Additionally, since the deposition takes place at elevated temperature, during cooling the thermal mismatch stresses or "thermal stresses" develop in the coating due to the CTE difference between coating

and substrate material. The nature of thermal mismatch stresses is compressive as thermal expansion coefficient of substrates (mostly metal) is higher than that of coating material (ceramics) in general. The overall residual stress in a coating is the result of the tensile quenching stress and the compressive thermal stress. The sign as well as the magnitude of residual stress is critical for the integrity of the coating-substrate system, which influences the property and performance of the coating. Since this residual stress superimposes the external applied stress on the coating during its service, a coating with a very high residual stress can result in cracking, delamination or shape changes. Hence, the knowledge of residual stress is important for a coating design of a given part of a turbine. There are several ways of measuring the residual stress present in a coating such as X-ray and neutron diffractions, ex-situ and in-situ curvature methods[60, 61], change in curvature due to material removal[58] etc. However, in this study we will focus on the substrate curvature change in a coating during or after the deposition to estimate the stresses of and modulus in a coating.

Stoney Approximation

Stoney (1906)[62], first derived a stress calculation formula (Eq. (4.1)) for a thin electrochemically deposited layer on a substrate.

$$\sigma_q = \frac{E_s t_s^2}{6(1-\nu_s)\Delta R \Delta t_c} \qquad \text{Eq. (4.1)}$$

Where σ_q is the quenching stress in the layer. E_s, ν_s and t_c are t_s Young's modulus, Poisson's ratio and thickness of coating and substrate. ΔR and Δt_c are the change in radius and change in thickness of the coating respectively. The calculation is based on curvature change in a plate after deposition of a layer, assuming, no out-of plane stresses are present in the layered system. This relationship is valid as long as coating thickness << substrate thickness << radius of curvature. The Stoney formula to calculate the stresses has been extensively used to infer film stress change, as it does not require the knowledge of film modulus for calculations.

Brenner and Senderoff Approximation

Brenner and Senderoff[63] derived an alternative formulation (Eq. (4.2)) for thick films to remove uncertainties associated with Stoney's thin film approximation.

$$\sigma_q = \frac{E_s t_s \left(t_s + \beta^{5/4} \Delta t_c \right)}{6(1-\nu_s)\Delta R \Delta t_c}; \beta = \frac{E_s (1-\nu_c)}{E_c (1-\nu_s)} \qquad \text{Eq. (4.2)}$$

Where, E_c and ν_c are the Young's modulus and Poisson's ratio of the film. Though, the calculation requires properties of the deposited layer, the calculation was valid for

coating thicknesses up to half of that of the substrate thickness. This eliminates the limitation of spraying only thin coatings to calculate the stresses. Generally TS coatings are never thicker than half of the substrate thickness; therefore this formula is suitable for stress calculations in TS coatings, given that the Young's modulus and Poisson's ratio of the coating are known.

The above two expressions (Eq. (4.1 and 4.2)) are valid only for the deposited layer. However in the case of TS process the coating deposition occurs layer by layer, where the shift of neutral axis of a bending beam cannot be assumed to be fixed. In order to understand stress evolution in coatings, Tsui and Clyne[64] proposed an analytical model for predicting residual stresses in a progressively deposited coating on a substrate with planar geometry. The model is capable of calculating stresses from the curvature change due to each layer deposition under the assumption that, no temperature change occurs during deposition. Since it incorporates the shifting of neutral axis during deposition, this model is more precise than Stoney's or Brenner and Senderoff's approximation, and holds good for coating of any given thickness. The model also calculates and superimposes the thermal stresses developed in the coating during the cool down phase starting from the temperature at deposition to the room temperature. With the input of material properties and process details, a stress profile in the coating and the substrate can be predicted. Another part of the model calculates the mismatch stress developed due to cooling of the coated specimen from the deposition temperature to the room temperature. Our main focus in this dissertation is on the anelasticity of a deposited coating, therefore the detailed analyses of the above analytical models are beyond the scope of this study.

4.1.2. Elastic modulus calculations

Apart from the residual stresses, the elastic modulus calculation is also important for coating design. Beyond its significance in precise calculation of coating stresses, the elastic modulus provides information about the coating's porosity level, cohesion between coating layers and also governs the total thermal stresses generated during the cool down. Therefore the overall residual stress in the coating strongly depends on the coating modulus. There are several ways to measure the coating elastic modulus, such as tensile, compressive and flexural loading tests, micro-indentation etc.; however, we will mainly focus here on the modulus calculation based on bi-layer curvature-temperature (BCT) response of a coated specimen.

For linear elastic bi-layer systems, the formula given below is used to calculate the elastic modulus of a layer from the curvature change recorded against temperature change[60].

$$\Delta k = \left(\frac{6E_c^{'}E_s^{'}t_c t_s (t_c + t_s)}{E_c^{'}t_c^4 + E_s^{'}t_s^4 + E_c^{'}E_s^{'}\left(6t_c^2 t_s^2 + 4t_c^3 t_s + 4t_c t_s^3\right)} \Delta\alpha \right) \Delta T;$$

$$E_c^{'} = \frac{E_c}{(1-\nu_c)} \;\&\; E_s^{'} = \frac{E_s}{(1-\nu_s)} \qquad \text{Eq. (4.3)}$$

Where, Δk is the curvature change in the system against the temperature change (ΔT) and $\Delta\alpha$ is the difference in coefficient of thermal expansions (CTE) of coating and substrate. For a linear elastic material system, the change in curvature and temperature follows a linear relationship, which is not the case in anelastic plasma sprayed ceramics. Nevertheless, this formula can be used to extract the elastic modulus of a coating at different linear segments on a non-linear curvature-temperature plot for a given coating.

So far we have discussed the methods to estimate stresses and elastic modulus from a given curvature-temperature relationship of a coating. In the following section we will see the applications of the above formulae. It is important to know that none of the above relationships for the stress calculations will be required or used for coating's anelasticity quantification. However it is worth discussing the different types of stresses developed in a coating over the course of the deposition process, as these stresses dictate the overall residual stress state in a coating which in turn governs the anelasticity to a great extent.

4.2. Stress evolution during coating deposition: in-situ coating property (ICP) sensor

Figure 4.1 shows the schematic of the *in-situ* coating property (ICP) sensor[60], an approach developed at the Center for Thermal Spray Research at Stony Brook University, which measures the change in substrate curvature during deposition. There have been other attempts to measure the curvature change in the substrate at the time of deposition [35, 59]. However, the advanced ICP sensor enables precise curvature measurements with a high resolution. The ICP sensor setup has three laser displacement sensors spaced out by a distance of 74 mm. These lasers record the movement of the three points on a 9" x 1" substrate, mounted symmetrically on the ICP sensor by the screws fastened through two holes on both sides of the substrate. The relative change in displacements is fitted to the equation of a circle (Figure 4.2).

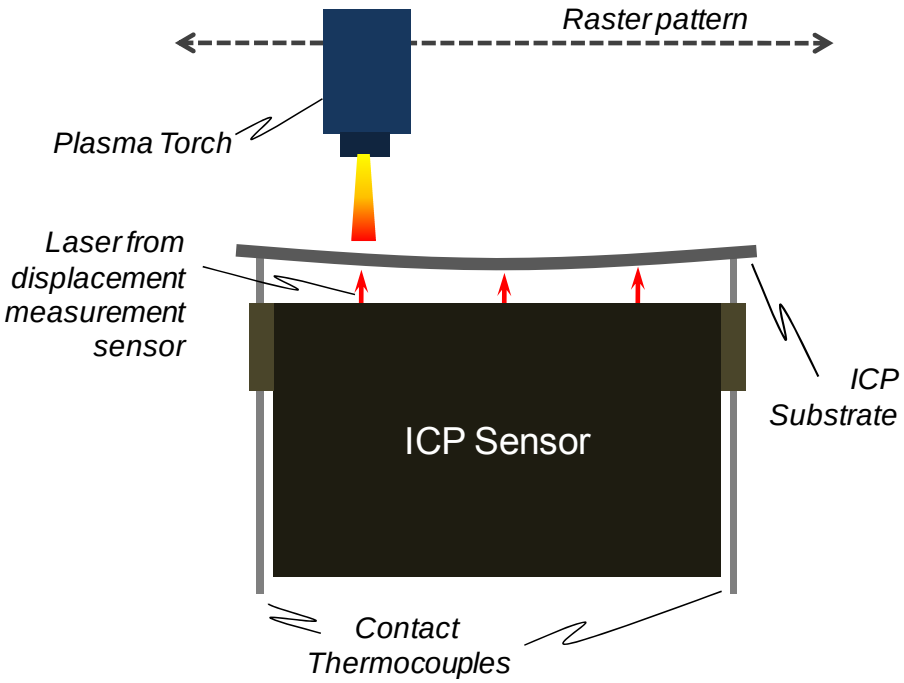

Figure 4.1: Schematics of in-situ coating property (ICP) sensor.

For the temperature measurement of the substrate, two contact thermocouples on both ends of the substrate are attached to the sensor (Figure (4.1)). The *in-situ* measurement of the curvature as well as the temperature change with time is then recorded and plotted by software. Figure 4.3 displays the recorded data of a typical APS YSZ coating deposition on an aluminum substrate. Each local peak corresponds to one pass during deposition, and each of the local minima points is where the next pass starts. By visualizing the ICP data, the complete coating deposition scheme can be traced.

The ICP sensor's curvature-temperature plot can be divided into three parts. The first part represents the preheating process. Each of the peaks in the plot belongs to each preheat pass. After preheating, the torch is brought back to its "home position" where the powder feed is turned on. It takes a few seconds to get a stable powder feed into the plasma, and while this happens, the substrate temperature drops a little bit (Figure 4.3). It is interesting to note that the cumulative curvature change at the end of each pass is an increasing function, and a linear approximation can be made for overall curvature change at the end of each pass. The slope of this line is referred to as "evolving stress". We will discuss about it later in this section. The third part of curvature-time plot is recorded during the cooling of the coated specimen. During this session the specimen undergoes curvature change due to thermal expansion mismatch

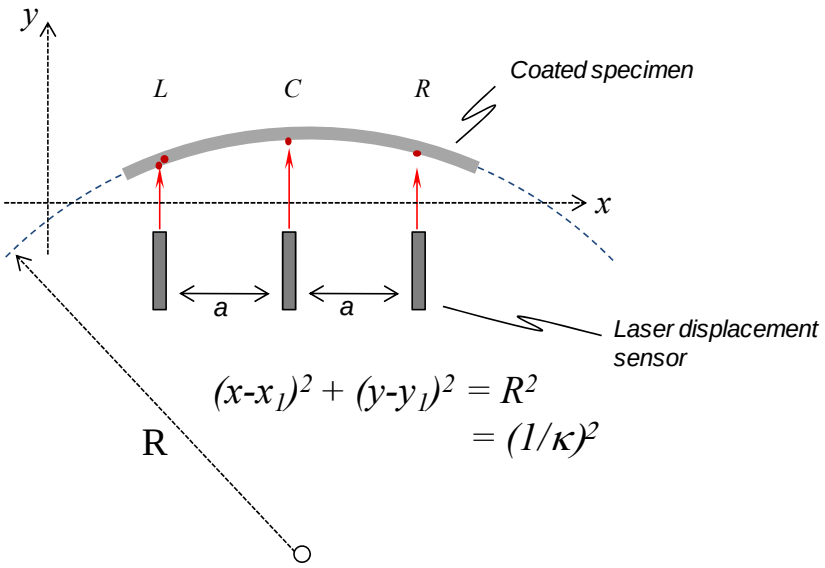

Figure 4.2: Curvature calculation scheme from the three point deflection records by displacement laser sensor measurements.

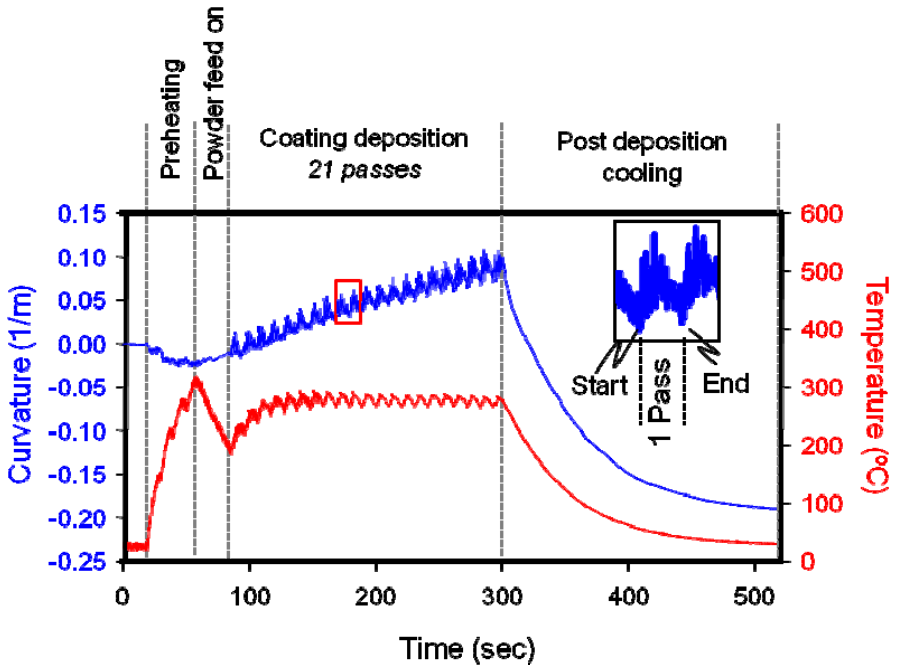

Figure 4.3: A typical curvature and temperature plot against time obtained from the ICP sensor. The steps for deposition process are mentioned in the figure.

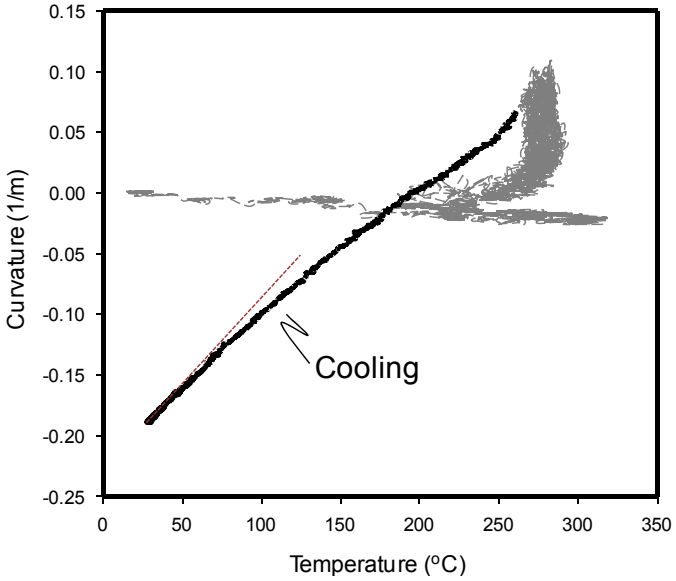

Figure 4.4: The curvature-temperature plot of the ICP data shown in Figure 4.3. During the cooling down process, the coating shows non-linear behavior.

The three sections of the ICP sensor's data provide stress information about the three stages of deposition. The overall curvature change during preheating, though very small, gives information about the relaxation of surface residual stresses in the substrate, generated due to the grit blasting process. The change in curvature in each pass in part-2 of the ICP sensor data clarifies the contribution of the stress generated in the pass onto the overall stress state of the layers deposited prior to that pass. In most cases this curvature change per pass is almost constant. Therefore the curvature-time plot in part-2 can be approximated as linear, where the slope of the line can represent the stresses evolved during each layer, also referred to as "evolving stress". The evolving stress can be correlated with the quality of bonding (cohesion) between the layers at the macroscopic scale and among the splats at microscopic level. For most of the plasma sprayed ceramic coatings, the evolving stress is positive which indicates that quenching stresses develop in coatings which are tensile in nature. For APS ceramic coatings, if the evolving stress is low cohesion is poor and for a coating deposition with high cohesion evolving stress is high. At the end of deposition, the plasma sprayed ceramic coatings are in tension irrespective of the substrate material properties. The coating-substrate system cools down after deposition, and the sign of thermal expansion mismatch governs the room temperature stress state of the coating. If the sign is positive, i.e. CTE of the coating is lower than that of substrate material, a compressive thermal stress superimposes on the tensile stress generated at the end of

the deposition. The resultant stress is referred to as room temperature residual stress in the coating.

There is another perspective of ICP sensor's data: the curvature and temperature relationship. Figure 4.4 shows the curvature-temperature plot of the curvature-temperature-time data shown in Figure 4.3. While the grey colored part of this curve belongs to the preheating and coating deposition period, the rest of the plot corresponds to the cooling down process from deposition temperature to room temperature. It is interesting to observe the non-linear behavior of the curve, which is quite dissimilar to the linear relationship between curvature-temperature derived for a general bi-layer material (Eq. 4.3) assuming the two layers to be linear elastic. The non-linearity can arise from the following two sources. The first source could be change in the substrate's elastic properties at high temperature, and the second could be the coating's intrinsic properties contributing to the non-linearity. The temperature range in which the deposition is performed excluded the possibility of any mechanical strength loss in the substrate material. Therefore it becomes obvious that the non-linear curvature-temperature plot is purely due to the intrinsic properties of the coating itself.

4.3. Ex-situ thermal cycling of a deposited coating: BCT measurement sensor

4.3.1. Reproduction of curvature-temperature curve by heating the coating using a flame torch

To reproduce the cooling curve of the curvature-temperature data recorded by ICP sensor, the specimen was reheated using a flame torch (usually MAPP gas) while it was on the ICP sensor. The torch was passed over the specimen multiple times until substrate temperature reached 250-300^{o}C and the system was left to cool under forced air convection conditions. Figure 4.5 shows the schematic of such a heating process. Typically it takes 2 minutes to heat up to 250^{o}C and about 7 minutes to cool down to the room temperature in the spraying booth. The curvature-temperature data was recorded and plotted for further analysis (Figure 4.6). There are large fluctuations in curvature measurements while the specimen is heated, which are produced by the motion of the hand-held flame torch. The far less noisy measurement during cool down displays the non-linear behavior of the coating. Even though, in comparison to the heating, the cooling section data is smoother and better for analysis, the presence of factors such as forced air convection and different radiation properties of coating and substrates

implies that the thermal gradient during cooling can be significantly large and inconsistent through thickness as well as along the length.

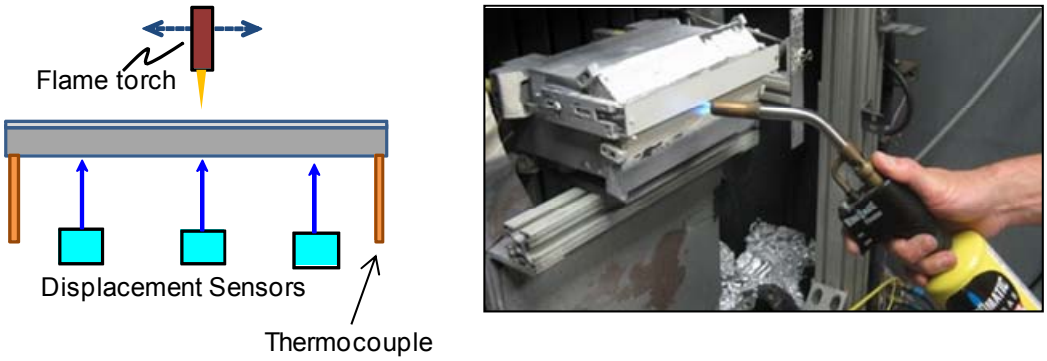

Figure 4.5: The schematics and photograph of specimen heating using a flame torch to reproduce the cooling curve of Figure 4.4.

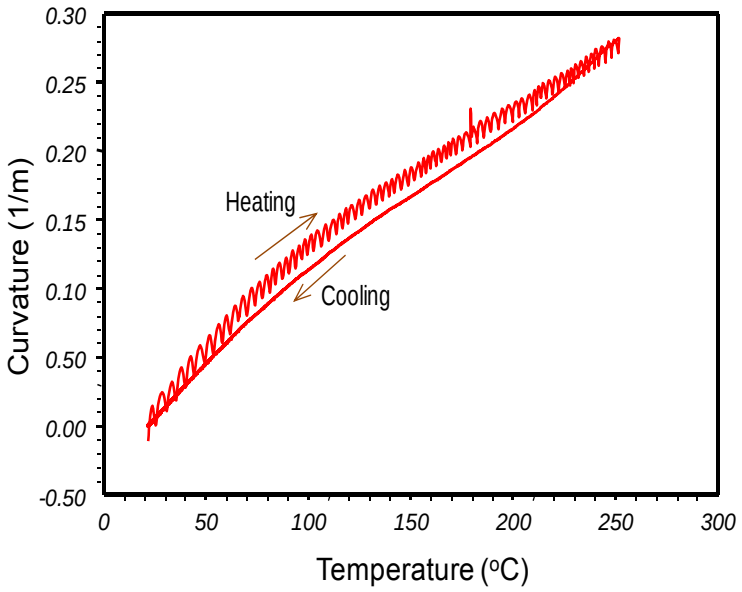

Figure 4.6: A typical curvature temperature record obtained from flame torch heating of substrate. The figure displays a clean non-linear behavior of the coating during the cooling.

4.3.2. Thermal cycling of coating using a heat-blower

To examine the curvature change in the coating-substrate system during heating, an alternative mode of heating is used (Figure 4.7)). A heater box with fans on the front face of the coating is used for continuous heating by blowing heated air on to the specimen. The air is blown through the fins of a heater core inside the box. Temperature of the air is controlled by heating and cooling of the heater. In this case it takes 15-20 minutes to heat the system up to 250°C, which is significantly slow when compared to flame torch heating. The cooling can take 15 to 40 minutes depending on the ambient conditions. To avoid any false measurement due to poor contact between the thermocouples and the specimen, self adhesive thermocouples (SA-KA series, Omega Inc., USA) are glued on both faces of the specimen. Due to the improvements in the measuring technique it has been possible to obtain smooth data for the heating and cooling for analysis and has also reduced the possibility of false temperature measurements. However the problem of inconsistent thermal gradients still persisted. Moreover these gradients were different for the heating cycle across different faces of the specimen and were dependent on the average temperature of the system during thermal cycle (Figure 4.8 (b)).

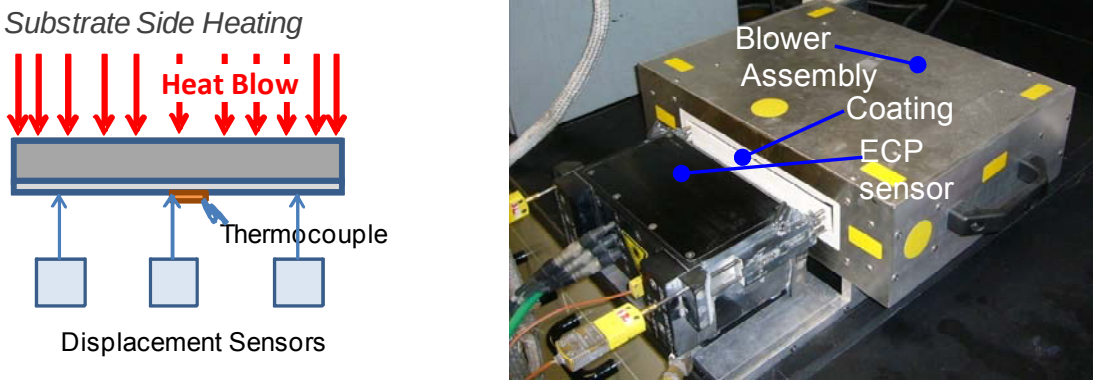

Figure 4.7: The schematics and photograph of specimen heating method using a box-heater assembly.

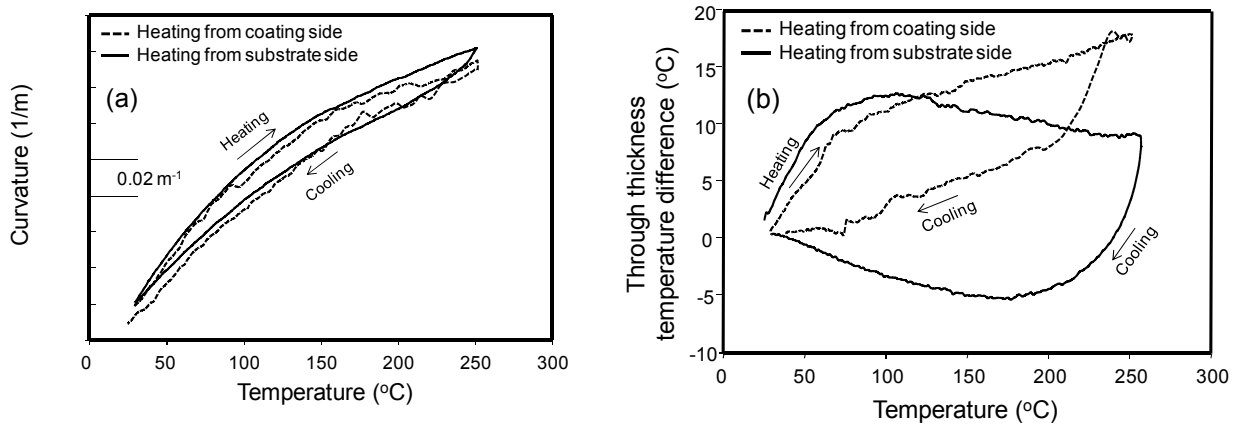

Figure 4.8: (a) curvature-temperature plots obtained from box heater assembly for the two different blowing directions. (b) temperature dependent front and back temperature difference for the two cases. Two things are to be noted. First, the box heater assembly introduces significantly large thermal gradient, and second, the curvature changes are different for the two modes of heating.

4.3.3. Uniform thermal cycling of coating in a furnace

Figure 4.9. To avoid any experimental artifacts associated with the thermal gradients developed due to forced air convection, this version of the BCT setup involves the whole thermal cycle (heating and cooling) being carried in a muffle furnace (Thermolyne-F6018). This modification provides a uniform heating and cooling with a negligible thermal gradient of 1 to 2^{o}C both in through thickness as well as along the length directions. Similar to the previous version of the test method, a self adhesive thermocouple is glued on to the substrate side of the specimen. Typically, one thermal cycle takes 30 minutes for heating from room temperature to the maximum temperature (generally 250^{o}C), and approximate 10 hours for cooling. To shorten the cooling time, the specimen is taken out of the furnace at around 170^{o}C (T_{out}), and is then cooled down under ambient condition. The selection of the temperature was based on several experiments made in the past. At this temperature the specimen experienced less thermal shock due to sudden changes in temperature and cooling rates (Figure 4.10). For each specimen at least three thermal cycles were performed in order to confirm repeatable curvature-temperature response of the specimen. The very first cycle is distinctly dissimilar to the second and third cycle; however the later two are highly repeatable (Figure 4.10). In most of the cases, the second cycle was considered for further analysis.

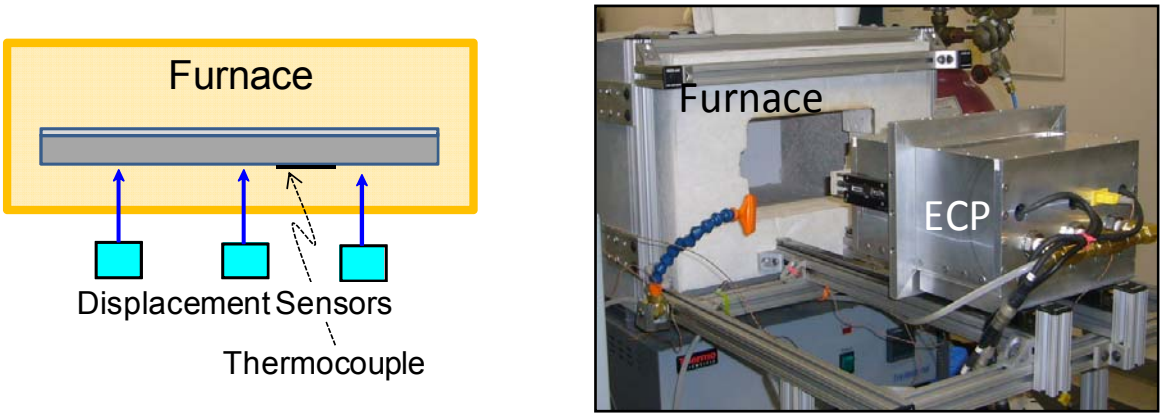

Figure 4.9: The schematics and photograph of advancement in specimen heating using a muffle furnace.

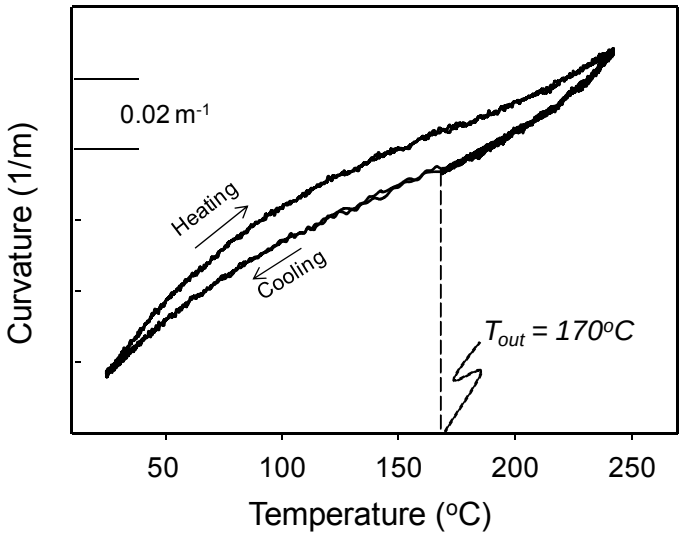

Figure 4.10: A repeatable curvature-temperature plot obtained from furnace heating of specimen. To shorten the time for cooling down, the specimen was taken out of the furnace at T_{out}=170°C.

Improvement with forced cooling

Figure 4.11. The data collected from the setup and procedure discussed in version- 3 was able to provide an error-free measurement of curvature and temperature for the heating part of the thermal cycle. This was used to extract the non-linear properties of the coating, especially the degree of non-linearity and the low temperature elastic modulus. However, in order to collect clean data for the cooling part of thermal cycle it was important that the specimen should not be exposed to any thermal shock which was almost unavoidable in the present setup as the specimen was taken out of the box at a temperature around 170°C. To circumvent this problem, an exhaust fan was

introduced at the orifice of the furnace, on its top wall, to extract heat from the furnace. This modification reduced the cooling time of the specimen from 250°C to room temperature by 8 hours and provided both smooth heating and cooling curves with a better hysteresis loop for quantification.

The non-linear and hysteretic curvature-temperature plot was then processed to extract non-linear coating properties: *ND*, *E* and another parameter "degree of hysteresis, *HD*".

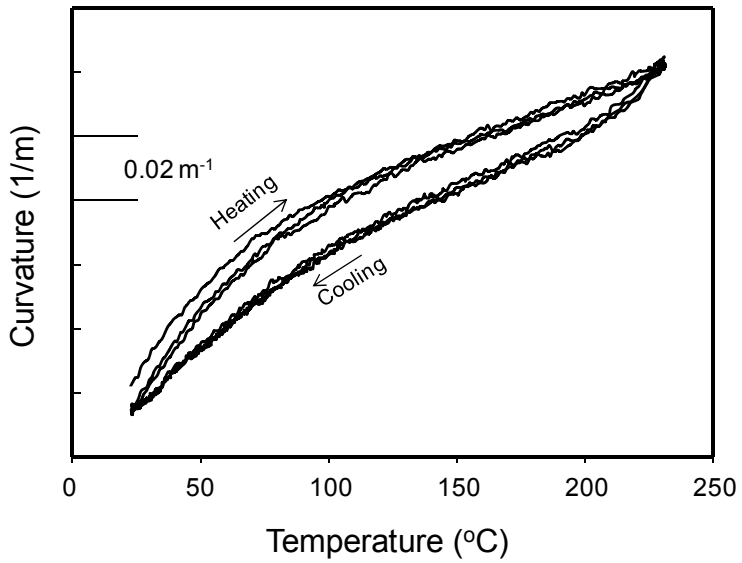

Figure 4.11: A repeatable curvature-temperature plot obtained from heating and cooling both in the furnace. First cycle is different from the consecutive cycles.

4.4. Quantification of anelastic properties

In a heating-cooling cycle the change in curvature at the beginning of cooling is highly sensitive to the maximum temperature of that cycle. Thus, interpretation of cooling curves must be made in conjunction with the maximum temperature of thermal cycle, though the maximum temperature achieved for the experiments can vary from day to day for the same furnace settings. At this stage of experiments it is difficult to assess the effect of cooling rates on the anelasticity under thermal loading; therefore only heating curves will be used to extract non-linear properties of coatings.

In order to describe the non-linear behavior of a coating, a phenomenological constitutive uniaxial stress-strain model, proposed by Nakamura et al, is adapted[61]. Apart from the thicknesses of coating and substrate, there are two other input

parameters required for the analysis. First is the post-deposition residual curvature, and second is the transition temperature. The former is important to decide the compressive stress state in the coating at the room temperature after the deposition, while the latter decides the temperature beyond which the coating delivers non-linear mechanical performance. The measurement procedure for the first one has been described earlier (section 4.3), and the second one is selected after drawing a straight line on the graph starting from the minimum temperature with the maximum number of data point falling on the line(Figure 4.11 (a)).

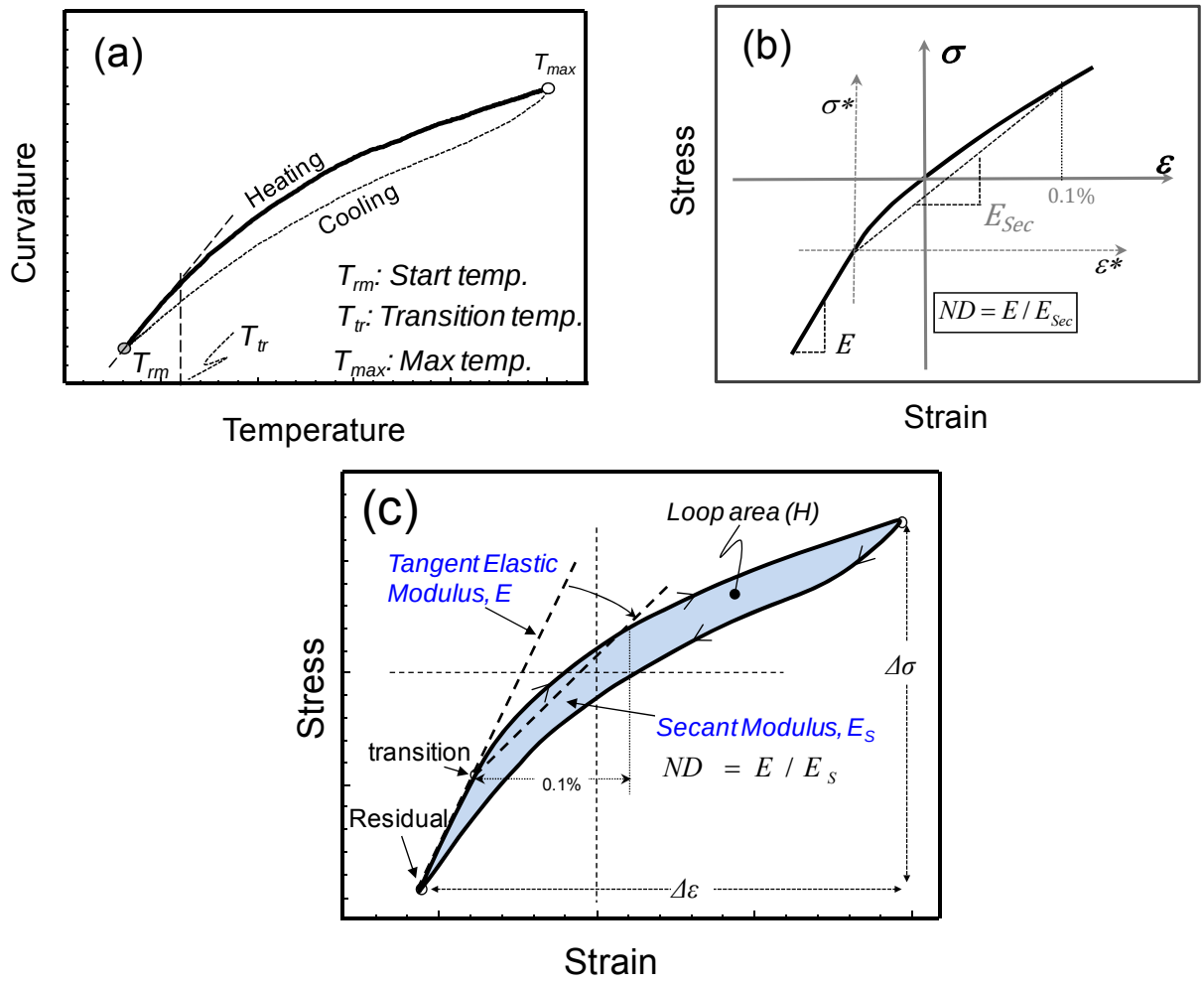

Figure 4.12: Stress-strain calculation scheme from a curvature-temperature data of a coating. (a) a typical curvature-temperature plot obtained from BCT measurements. The data is processed to calculate the stress-strain relationship (b) from the heating part of (a). (c) shows the complete stress-strain cycle corresponding to (a). Note that the *E* and *ND* are calculated only from loading or heating part of the stress-strain curve.

Following is the model that is used to convert the curvature temperature plot to a stress strain curve. This model considers temperature dependent Elastic modulus of substrate.

$$\varepsilon = \begin{cases} \dfrac{\sigma}{E} - \dfrac{\left|\sigma_T\right|^n}{E\sigma_N^{n-1}} & \text{for} \quad \sigma < \sigma_T \\ \dfrac{\sigma}{E} + \dfrac{(\sigma - \sigma_T)^n - \left|\sigma_T\right|^n}{E\sigma_N^{n-1}} & \text{for} \quad \sigma \geq \sigma_T \end{cases} \qquad \text{Eq. (4.4)}$$

Here E is the Young's modulus of coating, n is the power-law exponent and σ_N is the reference stress. Smaller σ_N indicates higher degree of non-linearity, while σ_N approaches towards infinity for the case of linear elastic materials. σ_T is the transitional stress corresponding to linear to nonlinear transition, which is mostly negative (compressive) for the case of YSZ on Al. Further, the non-linearity is associated with cracks opening and closing, and some cracks continue to close below σ_T, and hence the transition from linear to non-linear regimes is not very distinct. The schematic of stress-strain curve according to (4.4) is shown in Figure 4.12. Here the stress-strain axes ($\sigma^* - \varepsilon^*$) centered at $\sigma = \sigma_T$ separates the linear and nonlinear regimes. This relation turns out to be very versatile in describing the stress-strain behavior of thermal spray coatings with minimum number of parameters (E, σ_N, n and σ_T). Under multi-dimensional condition (e.g., plate bending), the Poisson's ratio ν is also required. Also note that E is appropriately described as the *elastic tangent modulus* near room temperature since it is not the modulus at $\sigma = 0$[65].

This model considers the following three facts [26, 61].

- The stress-strain relation is expected to be asymmetric under tension and compression
- Under very large compression, the response should be nearly linear because many cracks and thin defects are closed
- The transition from linear to nonlinear generally does not occur under zero stress ($\sigma_T \neq 0$) in the coatings.

There are also certain limitations to this model

- The model is only good for a material which first behaves linearly and then exhibits non linear behavior later and not the other way round
- The residual curvature must be negative, which implies that the coating should be in compressive stress state at the room/ initial temperature.
- The transition curvature should be negative.

- The absolute curvature at the maximum temperature should be positive. In other words, the specimen should experience a zero curvature state between the transition and maximum temperatures.
- In our results the stress-strain relation is estimated from the heating curve of thermal cycle data. The four unknown material properties (E, n, σ_N and σ_T) are obtained as the result of non-linear analysis.

Furthermore, to differentiate the coatings based on their non-linear properties, another parameter, namely the nonlinear degree (*ND*) is introduced[47].

$$ND = \left(\frac{E}{E_{\sec}} \right) \qquad \text{Eq. (4.5)}$$

Where, E is the room temperature elastic modulus, Equation (4.4), extracted from linear region of simulated stress-strain curve, and $E_{\sec}$ is the secant modulus between the transition and the 0.1% strain points on the curve. ND=1 corresponds to a linear elastic coating. Larger values of ND correspond to coatings with greater nonlinearity. Finally the two parameters, E and ND, obtained from the stress strain curve of a coating (Figure 4.12 (b)), are mapped onto ND vs E space.

In order to generate a closed loop stress-strain relation, it is important to process the cooling curvature data to get the stress-strain curve for the cooling curve. The heating and cooling curvature data is processed separately and joined by matching the two room temperature residual stresses from heating and cooling stress-strain curve. The section of the curvature-temperature curve, from the start of cooling up to the point where it remains concave upwards, cannot be converted to stress-strain. Hence once the residual stresses are matched, the maximum stresses of the two stress-strain curves are joined by a linear approximation (Figure 4.12(c)). From the stress-strain loop curve, three key parameters which quantify the anelastic behavior can be defined. The aforementioned parameters describe the extent of non-linearity present in the system. These can be calculated from the heating portion of the curvature-temperature curves obtained from third version of BCT measurement setup. However, the cooling of specimen inside the furnace in the fourth version of BCT measurement sensor enables the utilization of enclosed loop area for parametric characterization of the coating. Therefore, another parameter "Hysteresis Degree (*HD*)" can be introduced to represent the complete quantification of anelasticity in a coating. This parameter is obtained from the ratio of enclosed area of stress-strain curve $A_{\sigma-\varepsilon}$ over the rectangular area given by $\Delta\varepsilon \times \Delta\sigma$ (i.e., $HD = A_{\sigma-\varepsilon} / \Delta\varepsilon \times \Delta\sigma$) as shown in the Figure 4.11(c)[50]. Although the cooling/unloading of the specimen governs the total loop area in curvature-temperature

plot, the variability among different load cycles is reduced when it is normalized by $\Delta\varepsilon\Delta\sigma$.

Another way of quantifying the *HD* is by normalizing the loop area of curvature-temperature over the rectangular area of $\Delta\kappa \times \Delta T$, i.e. $HD_{\kappa-T} = A_{\kappa-T}/\Delta\kappa \times \Delta T$. This approximation is applicable for the data obtained from the coatings with significant non-linear properties. It does not require tedious stress-strain analysis or any linear approximation for the start of cooling curve. However, it could be erroneous to use it for comparing the coatings with subtle differences in anelastic behavior. A comparison between the two *HD*s will be presented in section 5.4.2. Nevertheless these three parameters, *E*, *ND* and *HD*, are valuable in quantifying the characteristics and differentiating anelastic responses of plasma sprayed coatings.

4.5. Summary and understanding of the anelasticity parameters

The three parameters, E, ND and HD, provide a complete description of the anelastic behavior of a given coating. The elastic modulus parameter of the coating (E) is the slope of the linear section of the modeled stress-strain curve at lower strains. Therefore, it can easily be assumed that *E* represents the mechanical response of coatings when most of the defects are compressed or immobile. When the applied tensile strain due to heating of the specimen provides sufficient stresses to bring the defects in motion, the coating starts behaving non-linearly. This stage is referred to as the transition from linear to non-linear. It is important to note that due to the nature of the coating microstructures, it is expected that there is no clear "transition" from linear to nonlinear regimes since some cracks continue to be closed above σ_T.

The second parameter, non-linear degree (*ND*), which is the ratio of *E* and the secant elastic modulus at 0.1% strain, can shed light on the pore and crack density in the coating. In general, a porous coating would exhibit higher values of ND. It is important to remember that the ND is a relative measure of the coating's compliance with respect to its initial stiffness, and hence can only be used as a first approximation to describe the coating's compliance. For example, if the specification for a coating design is set to be X MPa stress or Y GPa tangential modulus at Z% strain, this can be achieved both by producing a coating with low *E* and low *ND* as well as with high *E* and high *ND*. Hence a direct correlation between the ND and coating's compliance should be made carefully.

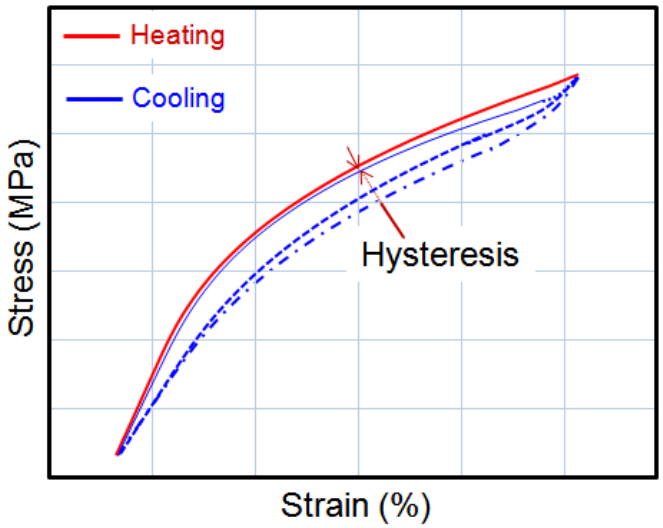

Figure 4.13: Illustration of possible behavior of a coating on the reversal of loading for coatings with three different crack densities. The area of hysteresis loop, and hence the HD, can significantly differ even for the same loading curve.

Degree of hysteresis (HD), the third parameter, is a measure of crack density in the coating. If a heating curve shows non-linear behavior, the return path during cooling will depend on the number of cracks contributing to the non-linear response of the coating. A lower crack density may result in reduced hysteretic response in the coating Figure 4.12. Later in section 5.4.3 we will see that the coefficient of friction at crack surfaces can also govern the degree of hysteresis.

In short, a complete understanding of the three parameters can provide insights to discern the contribution from the different types of defects embedded in a coating.

5. Sensitivity of anelasticity and its application in coatings repeatability assessment

The anelasticity in plasma sprayed ceramics is attributed to the opening or closure of the cracks and sliding friction between interfaces during thermo-mechanical sliding. While the former contributes to non-linearity, the latter introduces hysteresis in the mechanical response of a coating. Simulation on coating mechanical behavior requires understanding of the contribution of different defect geometries on the mechanical response. However, due to complex geometry, distribution and architecture of the defects, the modeling of coating structure in order to determine its property becomes extremely complex.

In order to understand the effect of embedded cracks on anelasticity, Liu et al[26] initially used an analytical single crack model to examine the stress-strain relationship of a single crack with a coating under compressive loading. The model provided insights on the dependency of anelasticity on the crack characteristics, such as crack opening dimensions and friction at sliding faces. It was observed that the single crack could exhibit significant anelasticity under mechanical loading and the response was sensitive to the crack geometry as well as surface properties. In the case of plasma sprayed coatings, the defect structure can be significantly modified by minor alterations in process conditions, which, from the observations from single crack model, can affect the anelasticity of coatings. The following chapter first discusses the results presented by Liu et al from the single crack model, which has allowed for model guided design of experiments presented in this thesis. Furthermore, examining the experimental results within the context of such analysis provides enhanced interpretation of the experimental findings.

5.1. Single crack model

Figure 5.1 shows an embedded crack in a square domain of uniaxial compressive stresses as used by Liu et al. The details of the model equations and input parameters are discussed in ref [26]. Results discussed here mainly focus on the two main parameters: the coulomb friction coefficient (μ) across the crack faces and the opening between the faces (δ) at the center of elliptical shaped crack. Other parameters for the model such as the relative crack length and its orientation were kept constant. Also, the material was considered as linear elastic and the stresses were applied under plane stress condition. During the compressive loading cycle, four stages with different effective modulus of the system were defined (Figure 5.2).

I. Closing – closing of an initially open crack until the two crack faces are in contact.

II. Sliding – crack closure with crack face sliding against friction until maximum stress.

III. Sticking – crack faces sticking after the reversal of loading. The friction changes from dynamic to static.

IV. Back Sliding – crack faces slide back until separated.

To return to the zero stress state, another stage which follows Stage I will be needed. Also, a stress-free state at zero strain is assumed.

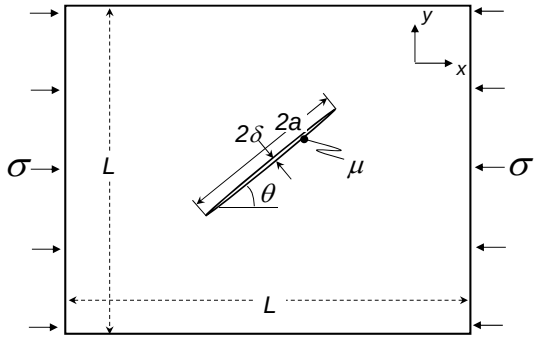

Figure 5.1: Schematics of the embedded crack under compression used by Liu et al. The angle (θ), coefficient of friction (μ), crack face openings (δ), and crack length (a) were used as inputs to the model for the stress-strain calculations[47].

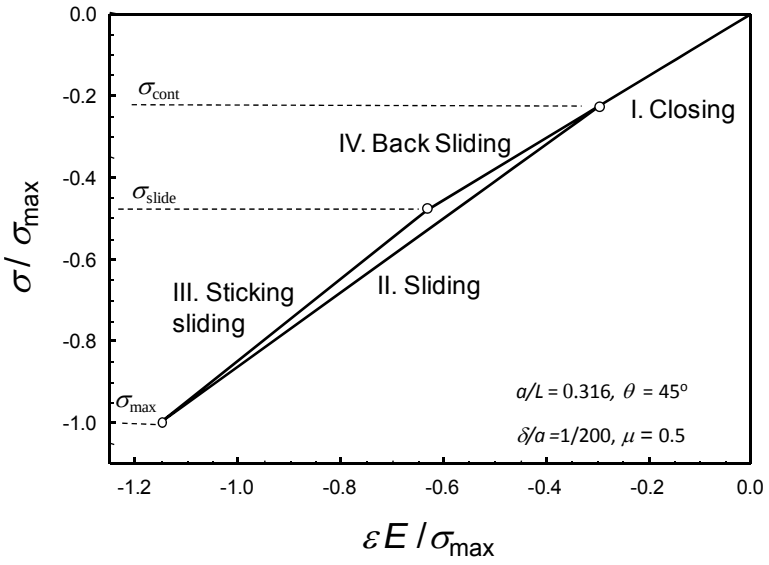

Figure 5.2: The four stages of the response of the single crack under compression. Note that after stage IV, another stage I would be required to bring the crack to its starting (zero) stress state[47].

From the results of the single crack model, the effects of various parameters were quantified (Figure 5.3). There was no hysteresis or non-linearity produced with the "no friction" case, while with the friction being maximum hysteresis was again zero. However, some non-linearity was observed at the higher stresses (Figure 5.3 (a)). The initial crack opening showed influence on the nonlinearity as well as hysteresis as shown in Figure 5.3 (b). From the Figure, one can observe that the hysteresis was largest when μ= 0.5 and δ= 0. In a plasma sprayed ceramic coating, there exist many cracks and weak interfaces with different opening dimensions, orientations and crack length ratio, and each contributes differently to the overall mechanical behavior.

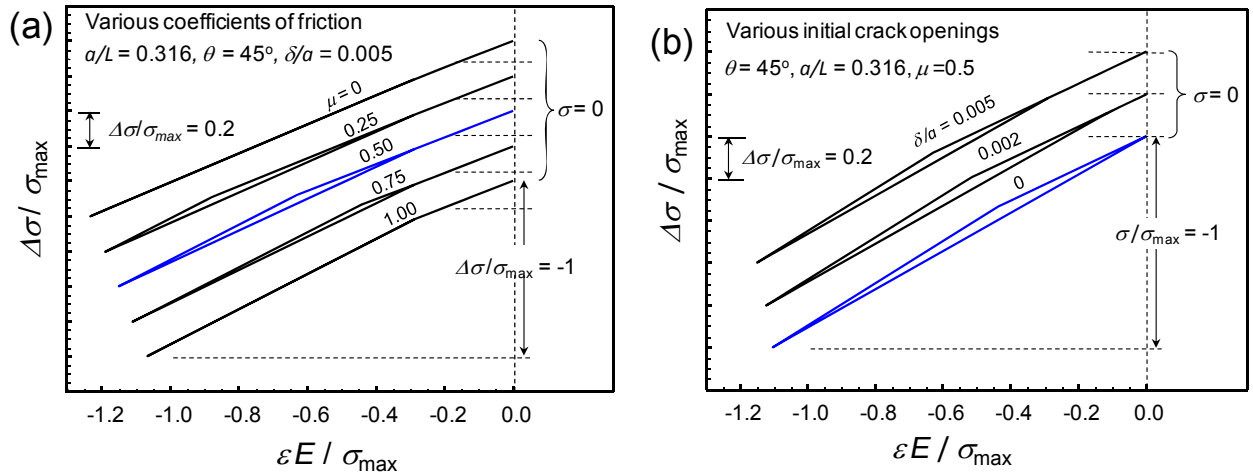

Figure 5.3: (a) effect of different coefficient of friction on the single crack's response. (b) effect of different crack face openings. The hysteresis is largest for the case of $\mu = 0.5$ and $\delta = 0$[26].

5.2. Multiple crack model applied on a crack matrix

Given that plasma sprayed coatings exhibit a complex microstructure full of embedded cracks, rigorous anelastic models that accommodate multiple cracks of various sizes and parameters would be even more complicated. Nevertheless, an operational definition to approximate the effective stress-strain relations of a multiple crack system was introduced as follows[26].

$$\frac{d\sigma(\varepsilon)}{d\varepsilon} = \frac{\sum_{i=1}^{N} a_i \left(\frac{d\sigma(\varepsilon)}{d\varepsilon} \right)_i}{\sum_{i=1}^{N} a_i} \qquad \text{Eq. (5.1)[26]}$$

Here, $(\ )_i$ denotes i^{th} crack of a model with N number of cracks. Essentially, the above expression is the weighted average of many cracks and the factor is proportional to the length of each crack. This average did not incorporate the coupling and the influences of neighboring cracks in a three dimensional coating structure. However, it did offer a simple estimation of approximate stress-strain behavior for the coating.

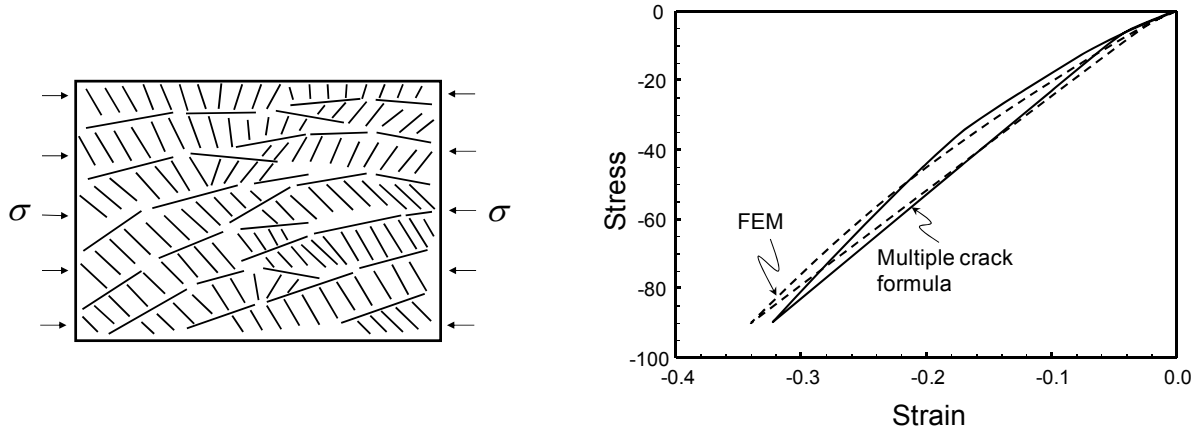

Figure 5.4: (a) multiple cracks mesh modeled from a PS YSZ coating. (b) stress-strain relations obtained from the approximated multiple crack formula and FEM analysis[26].

In order to examine the applicability of the above formula, a rectangular domain containing multiple cracks, closely approximated to a given plasma sprayed YSZ coating, was created as shown in Fig. 5.4 (a). Figure 5.4 (b) shows the stress-strain

relation estimated from Eq. 5.1 with the constant crack opening and coefficient of friction set as, μ= 0.5 and δ= 0.01 respectively. A detailed FEM analysis was also performed to calculate the stress-strain behavior of the crack matrix (Figure 5.4 (b)). The similarity between the model and FEM stress-strain relationships was remarkable despite the fact that the estimated averaged formula does not take into account the coupled effects of neighboring cracks.

5.3. Simulation of curvature-temperature plot for the given crack matrix

Most of the experimental results presented by Liu et al, produced by thermal cycling of a standard ICP substrate with coating on only one side, exhibited a changing beam curvature with changing temperature. Therefore, a simulated curvature-temperature response of a coating is more relevant than a stress-strain curve under compressive loading to the understanding of the coating's anelasticity. In order to examine the validity of the multiple cracks model for a coating with a substrate under thermal stresses, the model was modified to include a substrate as shown in Figure 5.5 (a). The input conditions for the model are mentioned in ref [26]. The results obtained from the model with different coefficients of frictions are shown in Figure 5.5 (b). Although the magnitude of nonlinearity and hysteresis were less than those shown in Figure 5.4 (b), the results clearly indicate that embedded cracks were sufficient to produce the anelastic behavior observed in a typical thermal cycle of a coated beam.

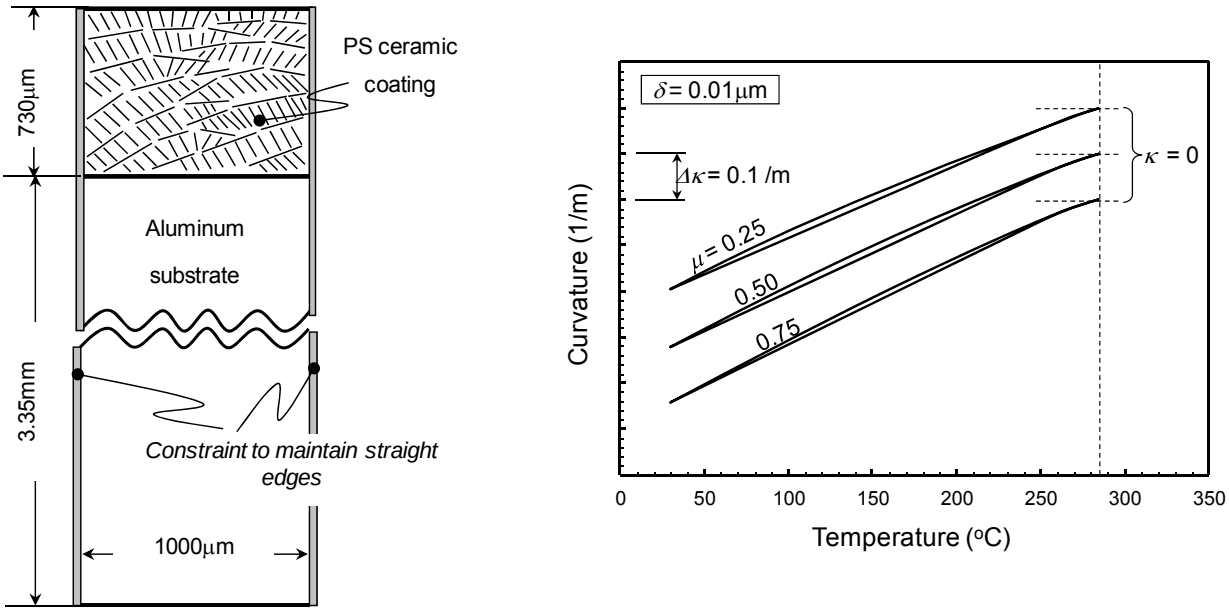

Figure 5.5: (a) multiple cracks mesh on an aluminum substrate to be analyzed for its curvature-temperature response. (b) results obtained from multiple-crack model analysis of the configuration under temperature change. Not only, cracks are capable of introducing anelasticity, but also the anelasticity degree can be changed by modifying the coefficient of friction between crack faces[26].

The above analytical study by Liu et al provides a significant background on the influence of cracks on anelasticity of a coating. These results can be extrapolated to predict the degree of anelasticity in different coating architectures and can serve as an initial framework for model guided design. The above results also show that the anelasticity is highly sensitive to crack characteristics such as crack face friction and crack opening dimensions. The following subsection discusses the experimental results obtained from BCT measurement of four coatings with different microstructures representing different crack geometries and densities, to investigate the sensitivity of anelasticity towards microstructure.

5.4. Experimental results on sensitivity of anelasticity to process excursions

In their earlier work, Liu et al have shown the process dependence of anelasticity in plasma sprayed ceramic coatings[47]. However, the results discussed by them were obtained from the very first version of BCT measurement sensor, in which the specimen is heated using a hand-held flame torch. The non-linear curvature-temperature data,

recorded during the cooling, was used to obtain the anelastic parameters. The measurements were highly influenced by the environmental conditions, which also introduced through thickness thermal gradient to the specimen. Nevertheless, the trends observed in those results were sufficient for a coarse comparison between the coatings' non-linear properties, E and ND.

With further advancement in the BCT measurement sensor (version 2), a complete description of anelasticity can be presented. In this version the specimen was heated using a heat blower from one side of the substrate. In contrast to the measurements using previous version of sensor, the non-linear properties were calculated from the data obtained from the heating part of thermal cycle. Moreover, the new version eliminated noise generation due to moving flame torch which revealed the hysteresis information in the curvature-temperature plot. Therefore, the 2nd version of BCT measurement sensor was used to examine the sensitivity of anelasticity on coatings sprayed with different processing conditions.

Two different feed stock powder morphologies, HOSP and FC were used for deposition of four coatings. Two coatings were produced with two different feed rates, 60 and 30 g/min, using HOSP morphology powder. The remaining two were sprayed with two different powder cuts of FC powder (10-45 and 45-75 μm). The plasma parameters were kept constant for the coating deposition. Figure 5.6 presents a comparison between the two powder morphologies and the polished as well as fractured SEM micrographs of their corresponding coatings. Different morphologies provide distinct splat flattening and melting of powder particles in plasma. Also, particles with different powder cut can achieve significantly different temperatures and velocities. On the other hand, powder feed rate governs the number of particles approaching towards substrate, which can drastically change the coating formation pattern and hence the defect architecture.

Specimen	Powder	Feed rate (g/min)	Coating thickness (μm)	Substrate thickness (mm)	Particle Temp. (°C)	Particle Vel. (m/s)
HOSP- A	HOSP	64.5	488	3.256	3,050	156
HOSP- B	HOSP	28.2	450	3.311	3,085	154
FC- C	FC	33.6	704	3.269	2,548	197
FC- D	FC	32.1	526	3.312	3,062	172

Table 5.1: shows the details of powders used for the coating depositions, and their corresponding particles temperature and velocity measured by AccuraSpray sensor[26].

Figure 5.7 (a, c) and 5.8 (a, c) show the curvature-temperature responses of the four coatings. It is clearly observable that the four coating respond differently under the BCT measurement test. However, any interpretation based on the curvature-temperature plots could be erroneous, as these plots strongly depend on the coating thickness, which were not similar for all the coatings. Therefore, for a true comparison of anelasticity among the coatings, their stress-strain relationships were calculated (section 4.4) and plotted (Figure 5.7 (b, d) and 5.8 (b, d)). Two conclusions can be made from the figures. First, the four coatings exhibit different degree of hysteresis, i.e. the loop areas are different. Second, the initial slopes of the curves for the coatings are not same, which indicate that the stiffness of the coatings are different.

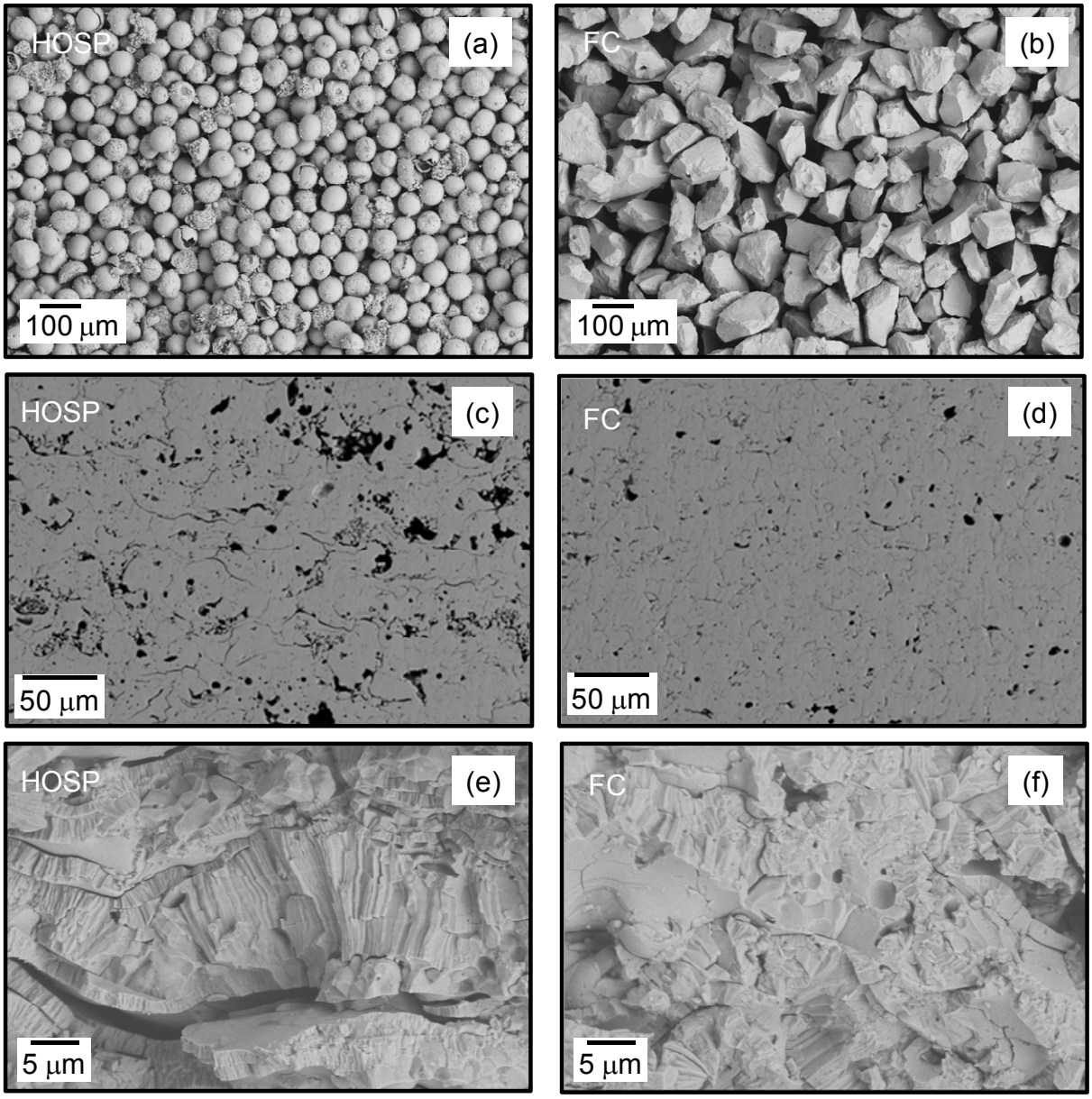

Figure 5.6: : SEM micrograph for powders with (a) Hollow Sphere (HOSP) and (b) Fused and Crushed (FC) morphologies. Polished ((c) and (d)) and fractured[26] ((e) and (f)) cross sections of HOSP and FC coatings sprayed at similar processing conditions. It is interesting to note how different powder morphologies form coatings with different defect architectures. HOSP coating exhibits more number of interfaces and cracks than the FC coating.

These visual observations enable assessment of sensitivity of coating anelasticity to processing conditions; however the quantified parameters of anelasticity, E, ND and HD, can reveal finer details on the coatings. Figure 5.9 positions the four coatings on the E-ND space with the HD numbers next to the individual points. It is clear that coatings

sprayed with HOSP powders have higher non-linearity and lower elastic modulus than those sprayed with FC powders. In addition to that, the hysteresis degree, in general, is higher in the case of HOSP powder coatings. Microstructural examinations of these coatings (Figure 5.6) reveal the presence of higher density of cracks and splat interfaces in HOSP powder coatings than FC powder coatings. This can be attributed to higher degree of defect interactions resulting in larger anelasticity in HOSP coatings.

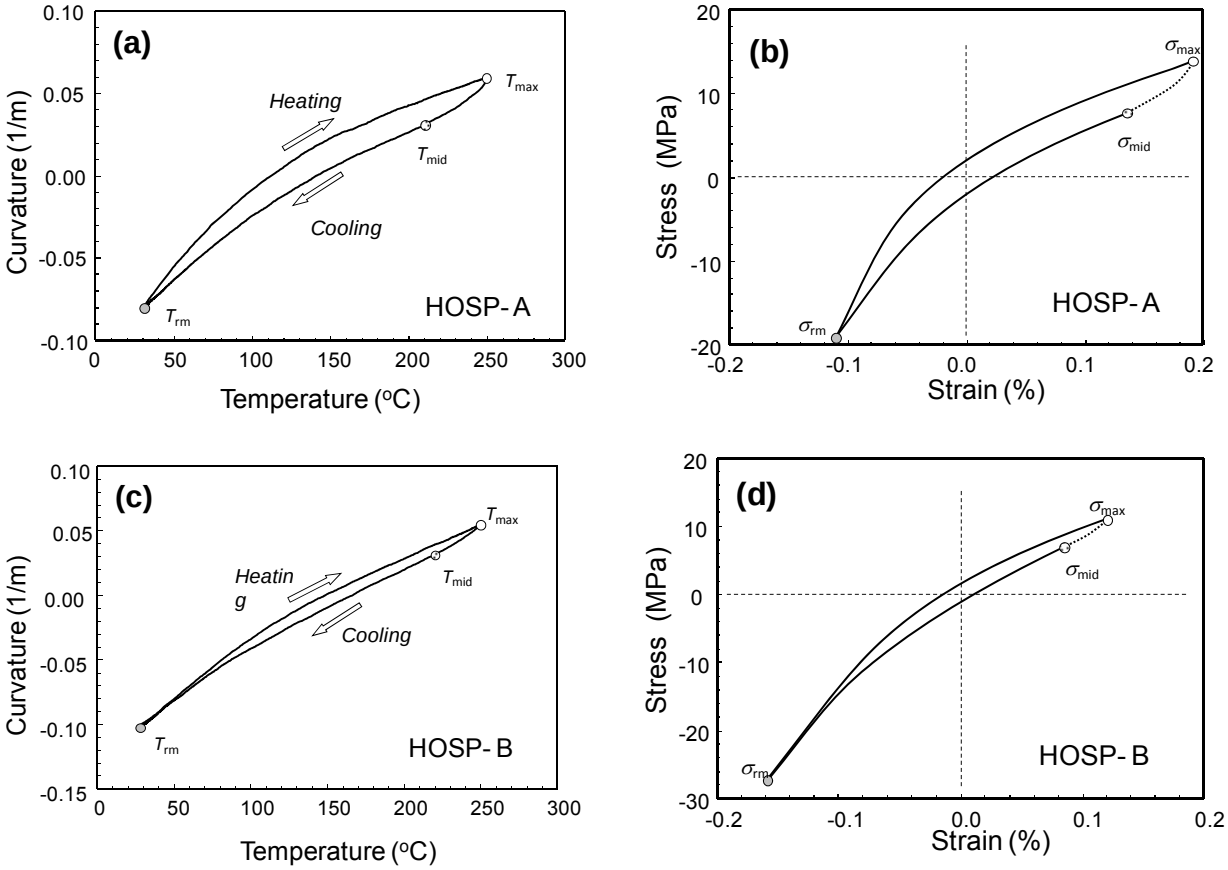

Figure 5.7: Curvature- temperature responses ((a) and (c)) and their computed stress-strain relations ((b) and (d)) of the two HOSP coatings. HOSP- A was sprayed with higher feedrate than that used for HOSP- B. The two coatings show significantly different anelastic responses both in curvature-temperature as well as stress-strain relations[26].

Coating sprayed at high feed rate (HOSP-A) is stiffer and more non-linear as well as more hysteretic than sprayed with lower feed rate (HOSP-B). The high stiffness can be attributed to the local microstructure which is likely to be denser due to high feed rate deposition. On the other hand, more non-linearity and hysteresis associated with HOSP-A coating could simply be due to higher number of splat interfaces and

microcracks. The particles temperature and velocity for the FC coatings are significantly different for the two powder cuts. The powder used for FC-C reflects higher particle velocity and lower particle temperature measured than the one used for FC-D. This could be attributed to the different powder size distribution used for deposition.

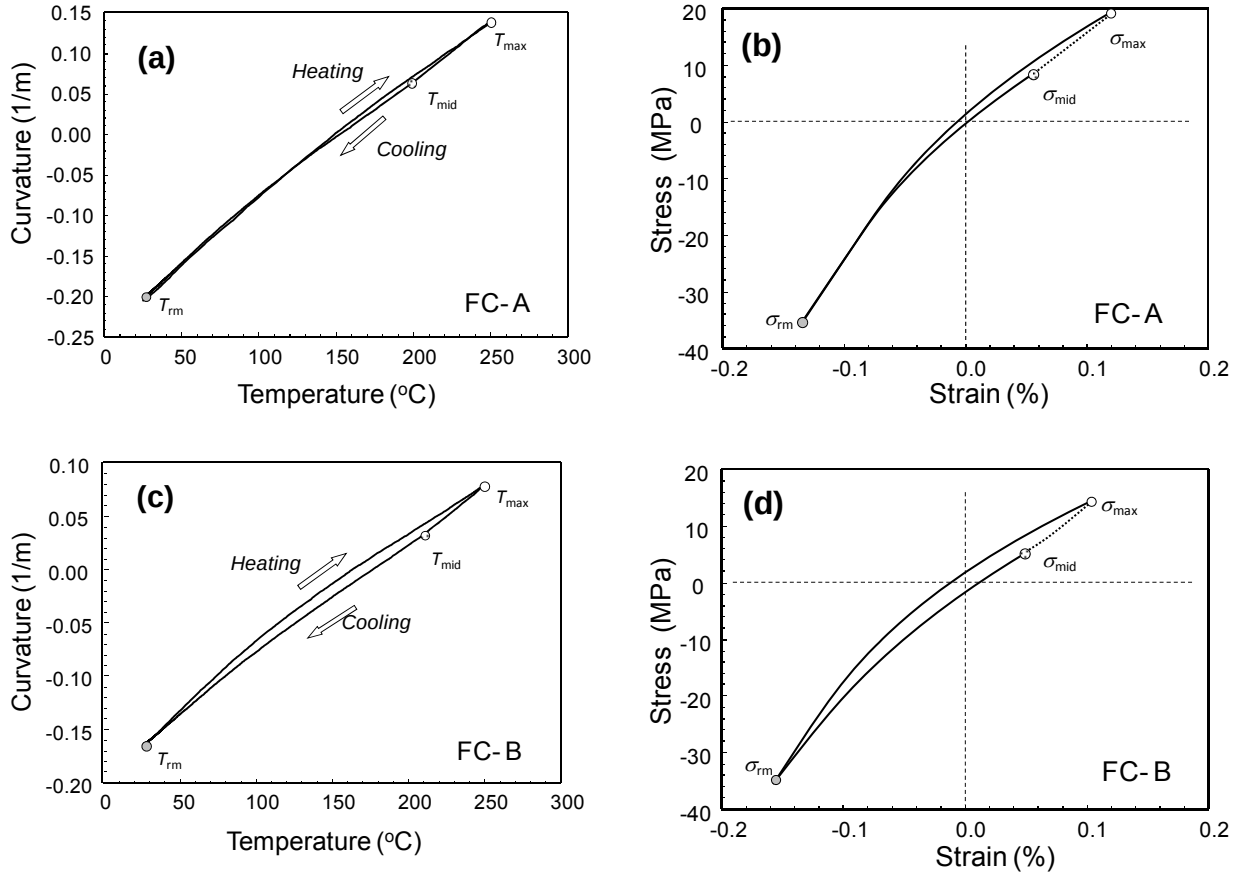

Figure 5.8: Curvature- temperature responses ((a) and (c)) and their computed stress-strain relations ((b) and (d)) of the two FC coatings. For FC- A, a finer powder cut was used than that used for FC- B. The coating sprayed with fine powder cut shows lesser hysteresis than that sprayed with coarse powder cut[26].

Above experiments and model results provide a first stage assessment on the sensitivity of anelasticity of coatings processed with different conditions. Hence, the anelastic parameters can be used to discern microstructural differences in coatings. Due to the high sensitivity and repeatability, these parameters may also be used to assess the repeatability of coatings sprayed with a constant process condition. Additionally, the

information revealed by the single as well as multiple crack models provide various means of controlling anelasticity such as, starting microstructure, feedstock material,

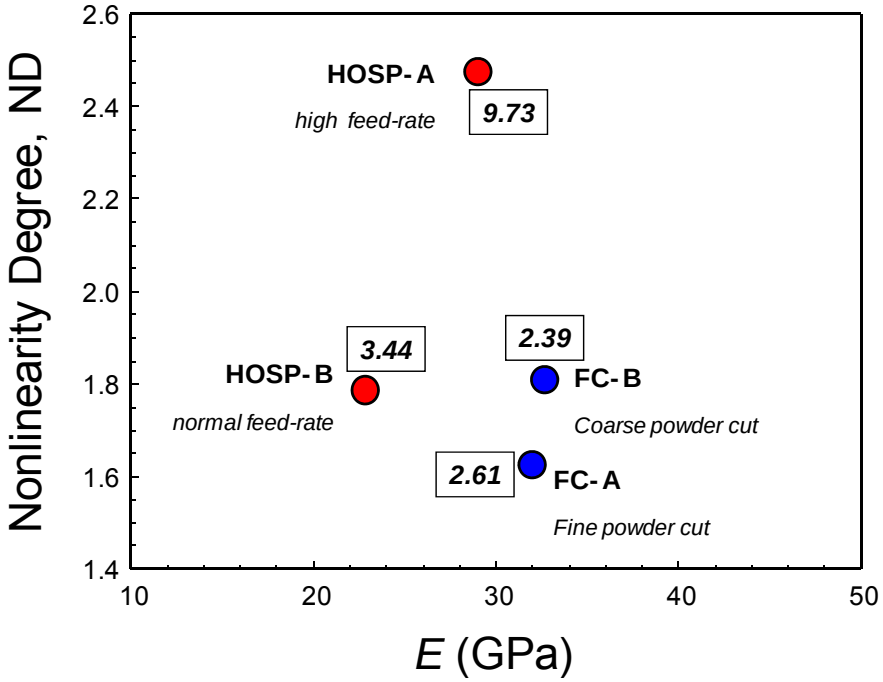

modification of crack surfaces by introducing different media, etc.

Figure 5.9: The non-linear parameters, E, ND and HD, of the four coatings along with their hysteresis degree (HD). The coatings are mapped on to the E-ND space for a better comparison[26]

5.5. Repeatability assessment of coatings using anelastic parameters

A plasma spray process consists of a number of steps to perform a coating deposition. A small variability introduced at any of these steps could alter coatings' properties significantly. Figure 5.10 illustrates a schematic of coating deposition scheme. As it can be seen, any minor alteration in inputs is capable of inducing some degree of variability in the coating property, and hence its performance. This issue related to process and coating reliability continues to confound academic and industrial researchers. This is particularly true for thermal barrier coatings (TBCs) applied on hot

section of a gas turbine engine. The coatings are sprayed on parts to provide a thermal protection to the material underneath. The detailed study on TBCs is beyond the scope of this study; however one of the chronic problems with these coatings is their reliability with regard to processing and performance. In general, the life of present TBCs, deposited at a constant process condition, invariably show a wide distribution with a high proportion of the population about a median value but a significant proportion failing at a much earlier service time[66] (Figure 5.11). This raises the question of "prime reliance" of the coatings, or the repeatability of coatings produced with constant processing conditions.

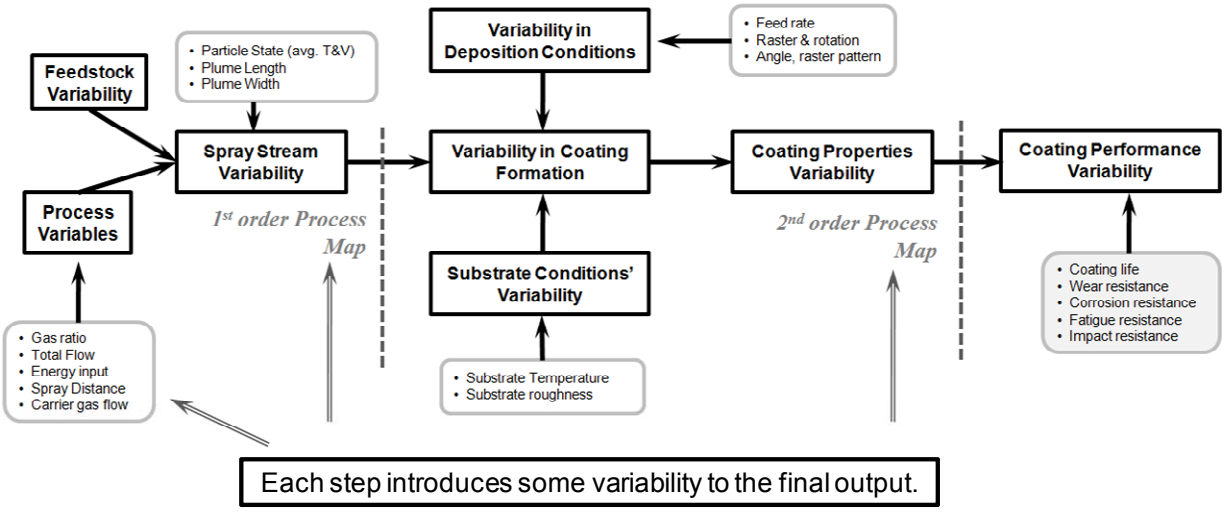

Figure 5.10: Schematic illustration of the steps involved in a coating deposition process. Variability introduced at any stage of these steps can change the coating properties, and hence its performance[67].

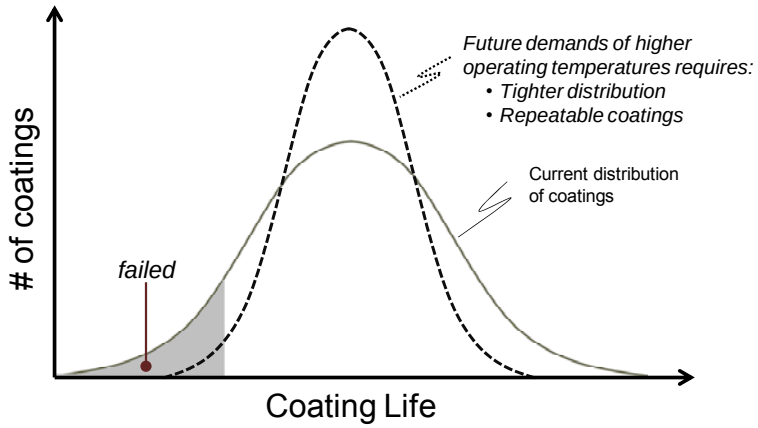

Figure 5.11: Illustration of TBCs distribution over their life cycle. A large number of coatings show much lower life cycle. A better reproducibility of a process can narrow the distribution.

The measured variability in a set of coatings is a combined effect of process variability, intrinsic variability of the coatings and the variability in the measurement unit or procedure. Process variability can be introduced due to various reasons and at several steps of a deposition scheme, such as powder size distribution and its feedrate, substrate conditions, plasma fluctuations, ambient conditions during deposition etc. On the other hand, intrinsic variability among the coatings can be induced due to the coatings' defect architectures which may significantly vary from one location to another within a coating. The variability of measurement unit or procedure will depend on the resolution of the unit as well as the contribution from the intrinsic variability of the coating. For example, Figure 5.12 shows the variability of room temperature thermal conductivity measurement performed on a bulk reference specimen (standard pyroceram), single plasma sprayed YSZ specimen and multiple (six) specimens prepared from a single YSZ coating. The first one describes the resolution of measurement technique (1.8% variability), while the latter two depict variability associated with a coating (up to 8% from a single coating). From this above example, one can conclude that to examine the variability in an overall process or in different coatings, it is important to know the variability associated with the measurement technique.

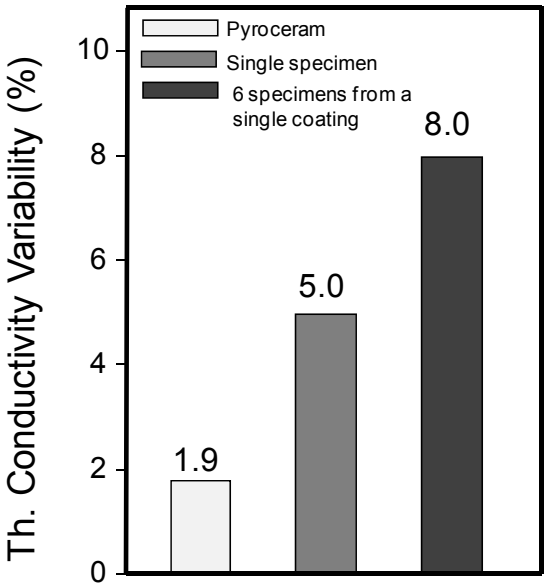

$$\% \text{ Variability} = \frac{Max - Min}{Average} \times 100$$

Figure 5.12: % variability in thermal conductivity measurements of a standard sample, a single PS YSZ and six different PS YSZ coating specimens from a single coating. The data clearly represents the intrinsic variability associated with the instrument (1.9%) and the coatings (8%)[44, 67].

A study conducted on the repeatability of plasma plume over a course of time suggested that the particles state produced by plasma spray process can have significant variability in it. It has been reported that the average particles temperature and velocity can vary notably over a course of long spray run. Not only that, the variability can be different from one combination of average particles temperature and velocity to another over the period of time. It has also been observed that different powders introduced deferent degree of variability to the spray plume. Therefore, the coatings produced even by a constant process condition are prone to exhibit significant variability in their properties. In the following section, a study is conducted to establish a baseline coating reliability, based on the measured properties of coatings sprayed at constant processing condition during a single spray run as well as over several days.

5.5.1. Design of experiment

In order to examine the coating repeatability over a temporal variation, three batches of YSZ coatings (four coatings each) were sprayed at similar process conditions using a single feedstock powder (YSZ-HOSP). However, the spray raster pattern was modified as per requirement of the experimental design. All the samples were sprayed on the standard ICP beams with similar thickness of 3.2 mm. The first batch (batch- 1) was prepared on ICP sensor (section 3.1.2.3) over the course of 4 consecutive days, while the

other two (batch-2 and 3) were sprayed on a carousel setup (Figure 5.13 (a)) having the stage spun at 72 rpm with torch movement (5 mm/sec) parallel to the rotation axis. The angular speed of carousel as well as the linear speed of torch was chosen so as to keep the spray pattern and particle flux similar to what was used for spraying of batch- 1. The spray distance was kept constant for all the cases at 100 mm. The deposition of first batch was designed to judge the "reproducibility of process" over different days, which includes the difference in day to day ambient conditions and the variability introduced due to start-stop of the plasma torch. No significant degradation of hardware was expected during this very limited usage of the system.

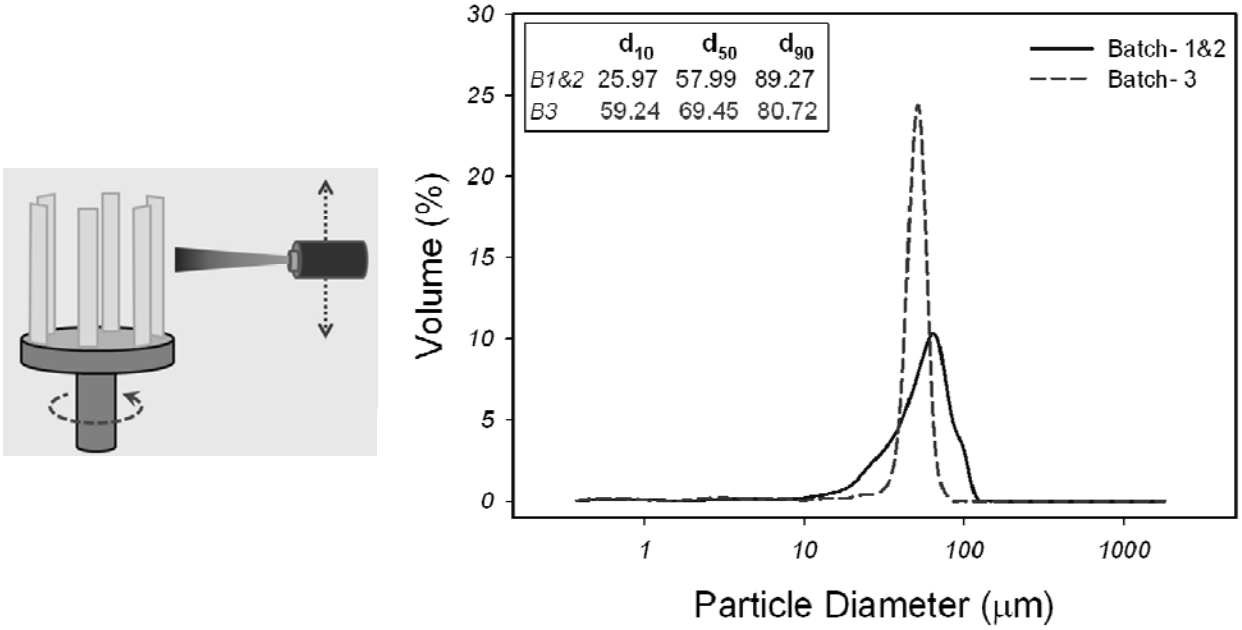

Figure 5.13: (a) schematics of carousel setup used for spraying of batch- 1 and 2. (b) the particle size distributions of the powder used for fabrications of batch- 1,2 and 3. Batch-3 was sprayed with a narrow size distribution powder[67].

The second and third batch were produced to examine the "repeatability of coatings" sprayed at the same time and spray run. This eliminates the chances of variability, which might have been introduced in the first batch, and provides intrinsic variability present in the coatings. Processing of batch- 2 and batch- 3 differed in the particle size distribution of the feedstock powder. A comparatively narrow distribution was used for fabrication of batch- 3 (Figure 5.13 (b)).

5.5.2. Characterizations and repeatability assessment

Subsequent to deposition, the thicknesses, weights and post deposition residual curvature was measured. The BCT measurement was performed and non-linear analysis was conducted on the coatings. Further, coatings' thermal conductivities and micro-indentation elastic modulus (as well as hardness) were measured. Since, the sample preparation for aforementioned measurements require cutting of a sample , these properties were measured for only three randomly chosen samples from batch-1, and one sample was kept for our future reference. Each of these post deposition characterization techniques provides information about certain aspects of the coating microstructure. To start with, the density obtained from the thickness and weight measurement provides an idea of the apparent porosity in the coating as compared to the bulk material. The post deposition residual curvature, as a first approximation, represents the overall residual stresses present in the coating. The thermal conductivity value is a comparative measure of interlamellar spacing and in plane defects embedded in the coating, while the indentation modulus is indicative of the response of the coating subjected to a localized load or stress. Therefore, exploring the coatings' repeatability based on different measurement may provide a better understanding of variability in properties at different scales. Also, it can also be used to address the fidelity of the measuring technique towards minute changes in coatings properties.

Figure 5.14 presents a comparative picture of different coating properties of specimens from same as well as different batches. The absolute values of the numbers obtained from different characterization are perhaps not readily comparable; however relative comparison of variability among the various sets of coatings can be made to shed light on the process. The error bars shown in the figure are the representation of variability in the measurement made on a single specimen repeatedly.

Figure 5.14 (a) shows thickness numbers of the three batches. As expected, batch-1 shows more variability in thickness as it was sprayed over many days, while batch-2 and batch-3 show quite repeatable coating thicknesses resulting from a single spray run. There is a slight difference in the degree of variability in batch-2 and batch-3, which is attributed to different powder cuts used for fabrication of the coatings. For batch-3 a finer powder cut was investigated to examine the effect of particle size distribution on variability. Variability in densities (Figure 5.14 (b)) in the coatings from a same batch as well as different batches is less than the error associated with the thickness and weight measurements, and is not significant enough to be compared.

The data from Figure 5.14 (c) suggests that coatings have significant variability in their thermal conductivity. However, this may be related to the intrinsic variability in the measurement techniques. Figure 5.14 (d) shows the variability in the thermal conductivity measurement using the Laser-Flash technique. From Figure 5.12 we have

learnt that specimens made out of a single coating showed a variability of 8% in its thermal conductivity values, which has both the effect of technique's intrinsic variability as well as the microstructural variability at different spots of the specimen. Therefore, it is unclear at this stage whether any conclusion can be drawn on the intrinsic variability of thermal conductivity of the three batches. . Improved measurement techniques with low testing variability will be required for sorting out the coating attributes.

The elastic modulus and hardness numbers (Figure 5.14 (e and f))) for the various coatings, obtained from micro-indentation technique appear different, suggesting some local variability among the coatings associated with each batch. Batch-2 displays highest variability among its coatings, while variability within batch-1 is higher than that in batch-3. Coatings from batch-2 are more porous than batches - 3 & 1. Since, micro indentation is a property characterization technique highly influenced by the local architecture of coating surrounding the indenter; higher porosity level is expected to give higher uncertainty in measurement and thus the measured variability. Additionally, one of the requirements of the indentation technique is the surface finish of the coating. With ceramic coatings, it is highly probable that the coating has some pullout (de-bonded splats) regions which can affect the coating behavior against the indentation locally, and coatings with higher porosity are more prone to have pull-outs as they have poor cohesions between the splats. In short, it is difficult to reach any significant conclusion about coatings' repeatability based on these measurements.

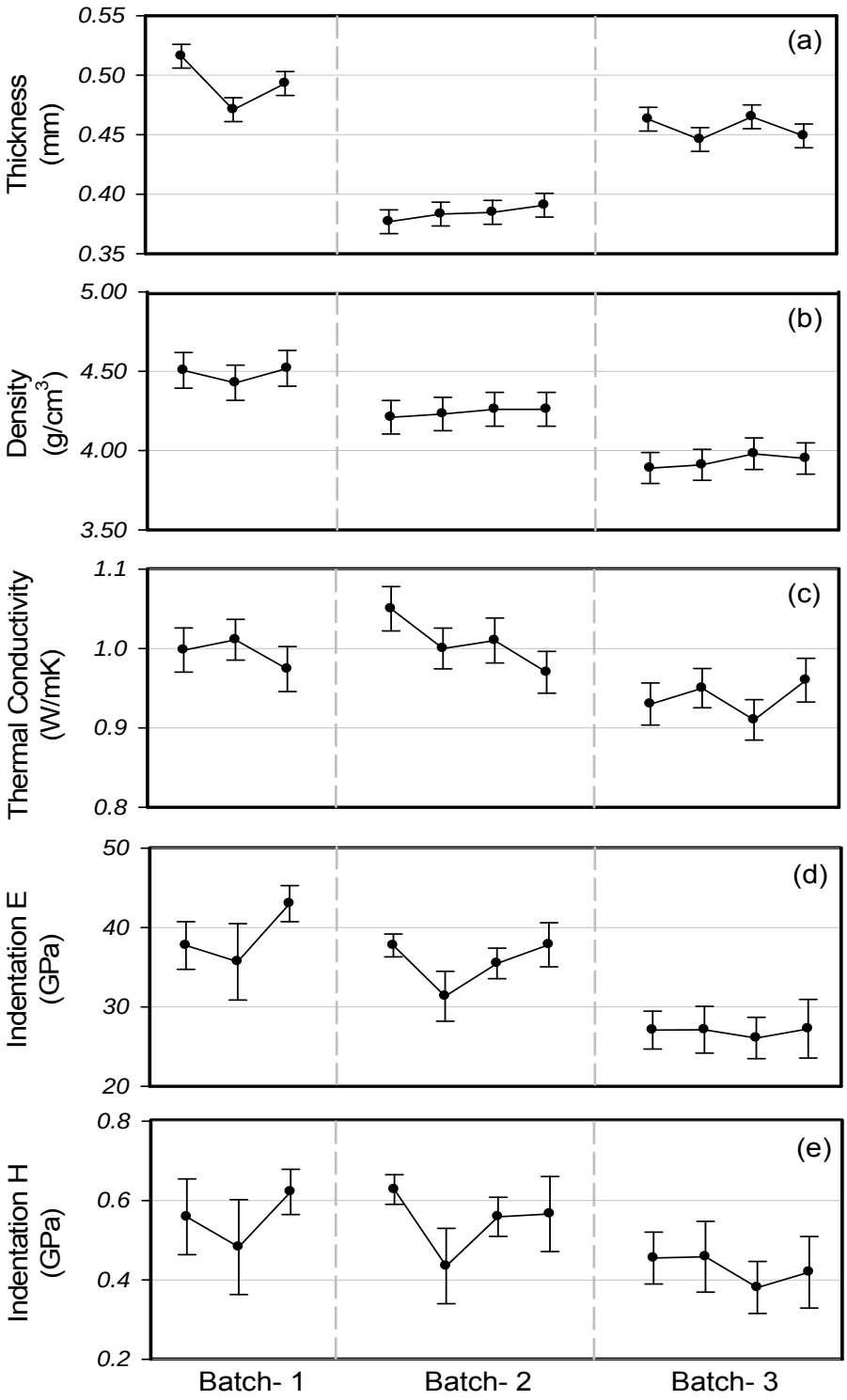

Figure 5.14: Post-spray deposition analysis and characterization for the three batches of YSZ coatings. Each measurement displays different order of variability in the coatings of that batch.[67]

Assessing coating property repeatability through measurement of non-linear properties

Post spraying characterization using metallography, indentation and thermal conductivity are prone to higher intrinsic variability; associated not only with the technique but the need for destructive specimen preparation which itself can introduce artifacts. On the other hand, the BCT measurement, based on a non destructive method, will minimize the source of errors associated with several multi-step characterization techniques. Not only that, the curvature-temperature response obtained from a large sampling volume of the coatings adds more confidence to the analyzed data. Based on extensive testing it has been observed that the sensitivity of the non-linear analysis is restricted to the error range of 2 GPa and 0.2 for E and ND respectively.

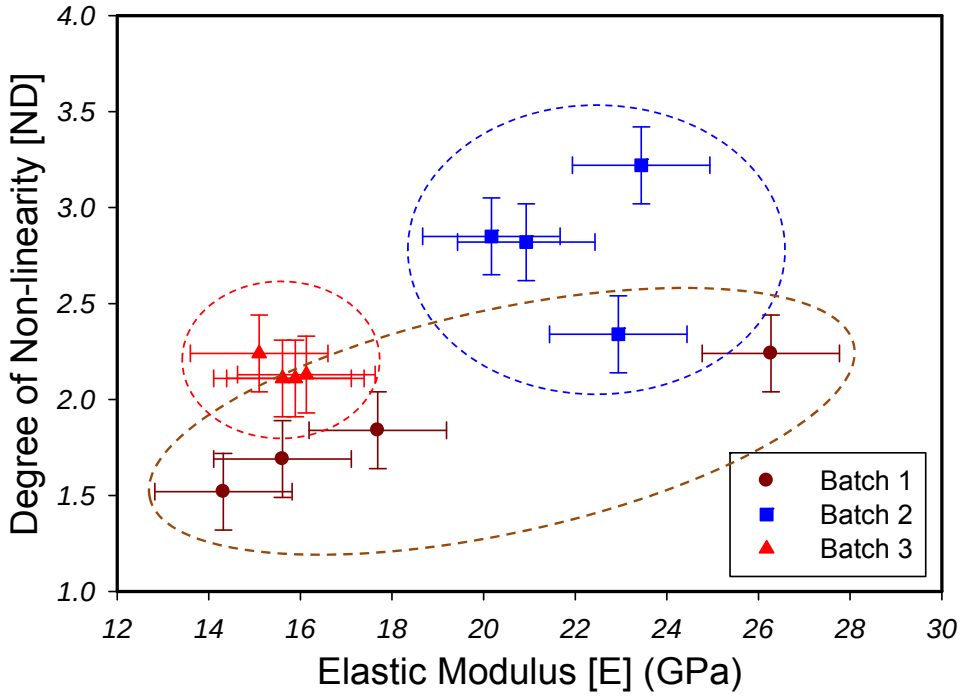

Figure 5.15: Map of non-linear elastic properties of plasma sprayed YSZ coatings from the three batches. Batch- 3, sprayed on carousel and with narrow powder cut, shows highest repeatability among the three batches[67].

Figure 5.15 provides the map of two anelastic parameters, E and ND, of all the samples from batch- 1, 2, and 3. The third anelastic parameter, which is degree of hysteresis, HD, was not calculated as the 3rd version of BCT measurement setup was used in which the part of the cooling of the samples was done outside the furnace and

which does not provide a clean unloading/cooling curve. Nevertheless, the two non-linear parameters *(E, ND)* provide several important observations

- All the coatings show a non-linear elastic response consistent with what was observed in previous sections. Different batches show different level of variability in their non-linear elastic properties. The resolution of non-linear analysis technique provides sufficient fidelity for comparing subtle changes in process and coatings.

- There can be significant local variability in properties of sprayed YSZ coatings even when sprayed in a single run (batch- 2 and 3). These local effects can introduce global variability in properties.

- Since, batch -2&3 were made on the carousel, the coating formation mechanism is different from the case of batch-1. They show higher non-linearity presumably due to lower splat impact interval period, which resulted in a weak splat bonding. The substrate temperature for these two batches is expected to be lower as the hot plasma plume was not always directed to a single specimen; for each rotation of the carousel, each specimen came in contact with the plume only for a very short period of time, otherwise it was being cooled by the exhaust air flow present in the booth. On the other hand for the batch- 1, since it was fabricated on the ICP sensor, the plasma torch was always directed at some part of the specimen.

- The variability among the coatings within the same batch, is maximum for batch-1 made over different days, and which includes start-stop of the plasma torch, different ambient condition (humidity, temperature etc.), and many other factors that can increase the variability. Batch-3 was identical in all aspects except for powder cut compared to batch-2. This resulted in different ND and E values and notably also showed a much smaller variability. From this observation it can be concluded that powder cut has more profound effect on the reproducibility of coatings in terms of their properties.

The above experiments suggests that the intrinsic variability in coatings sprayed with a constant processing condition depends on many external factors, such as day-to-day variability in plasma chemistry, particle size distribution of feedstock powder, deposition pattern and many more. Certainly, by minimizing these factors, from day-to-day to single run on carousel and from wide powder cut to narrow powder cut, the variability in the coatings can be controlled.

6. Controlled introduction of anelasticity via processing parameters

The results shown by Liu et al in section 5.1 suggested that anelasticity produced by single crack can be controlled by changing the crack opening dimensions. Furthermore, the experimental results discussed in section 5.3 presented strategies for modifying the coating architecture by changing the processing conditions, such as powder morphology and particle size distribution. Both the results showed that anelasticity is highly sensitive to the process conditions and the anelastic parameters can discern subtle differences in coatings. In this section, experiments were conducted to control anelasticity by tuning the processing conditions such as spray distance (distance between plasma torch and substrate), the plasma enthalpy (plasma power) and the deposition pattern (raster pattern used for deposition). Here, the spray distances were varied to change the dwell time of the particles in the plume so as to have different particle melting states. On the other hand, the plasma enthalpies were changed to achieve different energy transfer from plasma to particles. Lastly, different deposition pattern was chosen to deliberately change the time period for which plasma torch was against the substrate.

6.1. Spray distances

Three coatings with significantly different porosity as well as interface microstructures were produced for this investigation. The coatings were produced using YSZ-HOSP powder at a constant set of process input parameters (center condition) and feed rate. The microstructural changes were introduced by changing the spray distances, which were kept at 60, 100 and 150 mm, with corresponding coatings labeled as YSZ-A, YSZ-B and YSZ-C, respectively. Following observations can be made based on the particles diagnostics conducted by DPV2000 sensor, the cross-sectional SEM micrographs and the thermal conductivity measurements of the coatings.

1. The average particle T&V changes with increasing spray distance (Figure 6.1 (a)). Also, the melting states (MI) and kinetic energy (KE) distribution of the particles show a shift towards higher melting state and higher momentum with decreasing spray distances (Figure 6.1 (b)). These changes in particle states lead to coatings with different microstructures. The lower particle T&V result in a coating with greater pore content due to less melting of particles (YSZ- C), while particles with better melting states provide a more compact coating (YSZ- A).
2. The lower particle impact velocity also reduces the effective interfacial interactions and a widened spray plume causes reduced particle flux with concomitant change in number of sprayed layers (YSZ- C). YSZ-A is most dense among all three coatings, while YSZ-C has the highest porosity. It can be also observed that the density of splat interfaces is the highest in YSZ-C and decreases for shorter spray distance.
3. The through thickness thermal conductivities of the three coatings measured by laser flash technique show that YSZ-A has the highest thermal conductivity (0.99 W/m-K) followed by YSZ-B (0.82 W/m-K) and YSZ-C (0.69 W/m-K) (Figure 6.2). This also confirms that YSZ-C has the highest number of inter-splat boundaries or openings among the three coatings, as more in-plane defects reduce the thermal transport of a material due to phonons scattering.

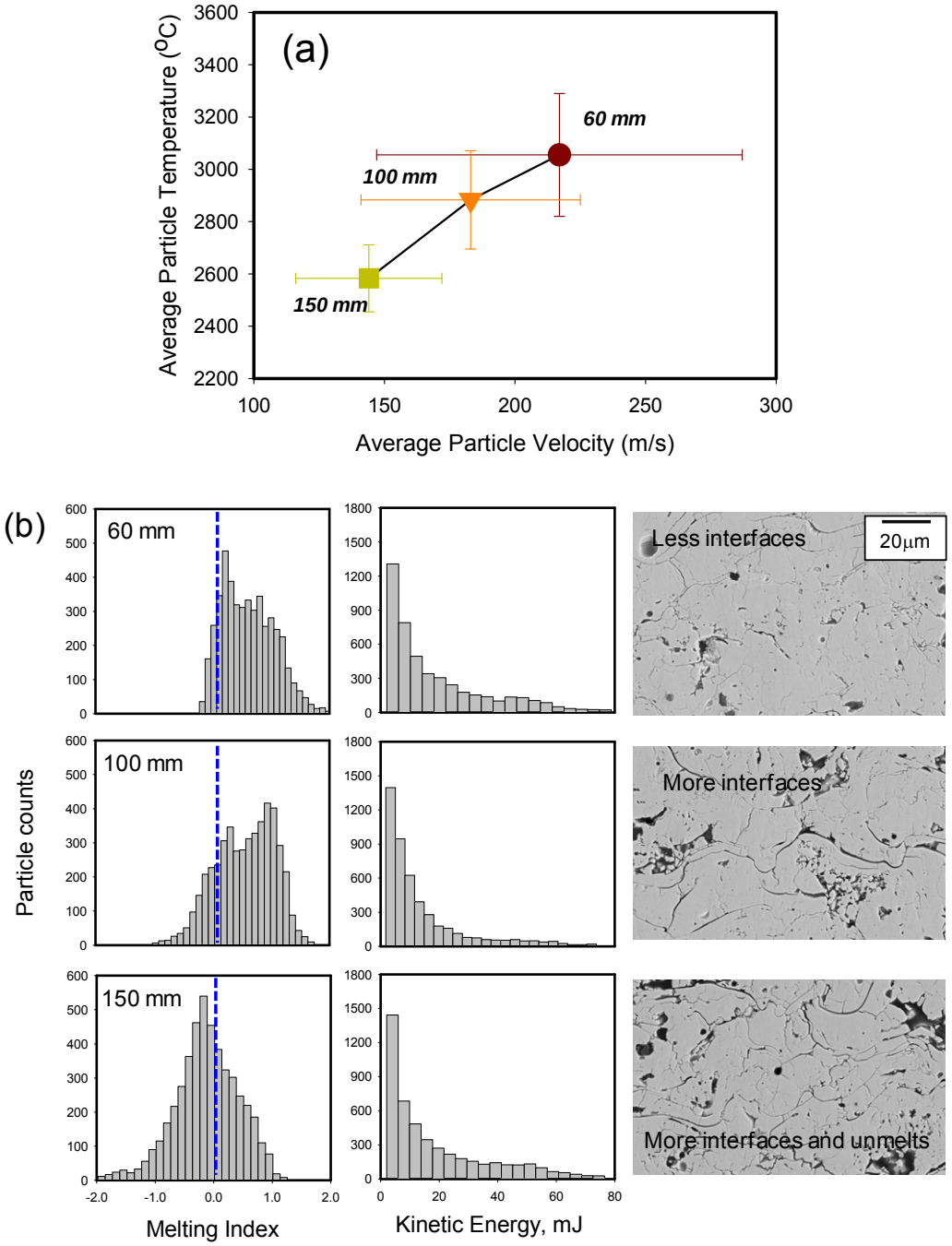

Figure 6.1: (a) Average T & V measured with DPV2000 sensor for coatings sprayed with three spray distance: YSA-A (60 mm), YSZ-B (100 mm) and YSZ-C (150 mm). (b) shows the melting index and kinetic energy distribution of the particles corresponding to the three coatings with their microstructures. The zero melting index is shown by dotted line. One can easily observe that coating sprayed with longer spray distance contains higher number of interfaces and unmelts attributed to the lower melting index of the particles.

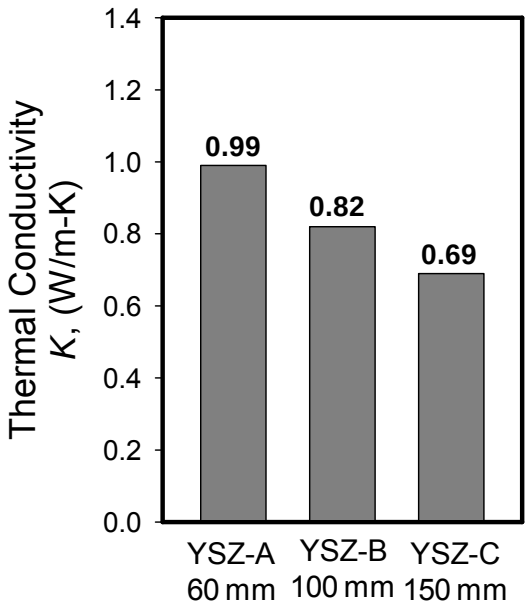

Figure 6.2: Thermal conductivity of the three coatings sprayed at different spray distances.

Figure 6.3 shows the anelastic curvature-temperature plots of the three coatings. The effective curvature change is governed principally by the microstructure and resultant coating stiffness, as the differences in thickness and thermal expansion among these coatings are minimal. The stress-strain relations were estimated from the curvature-temperature records for these coatings (Figure 6.3). Similar to the curvature-temperature data, all specimens exhibit distinct nonlinearity as well as hysteresis in their stress-strain curves.

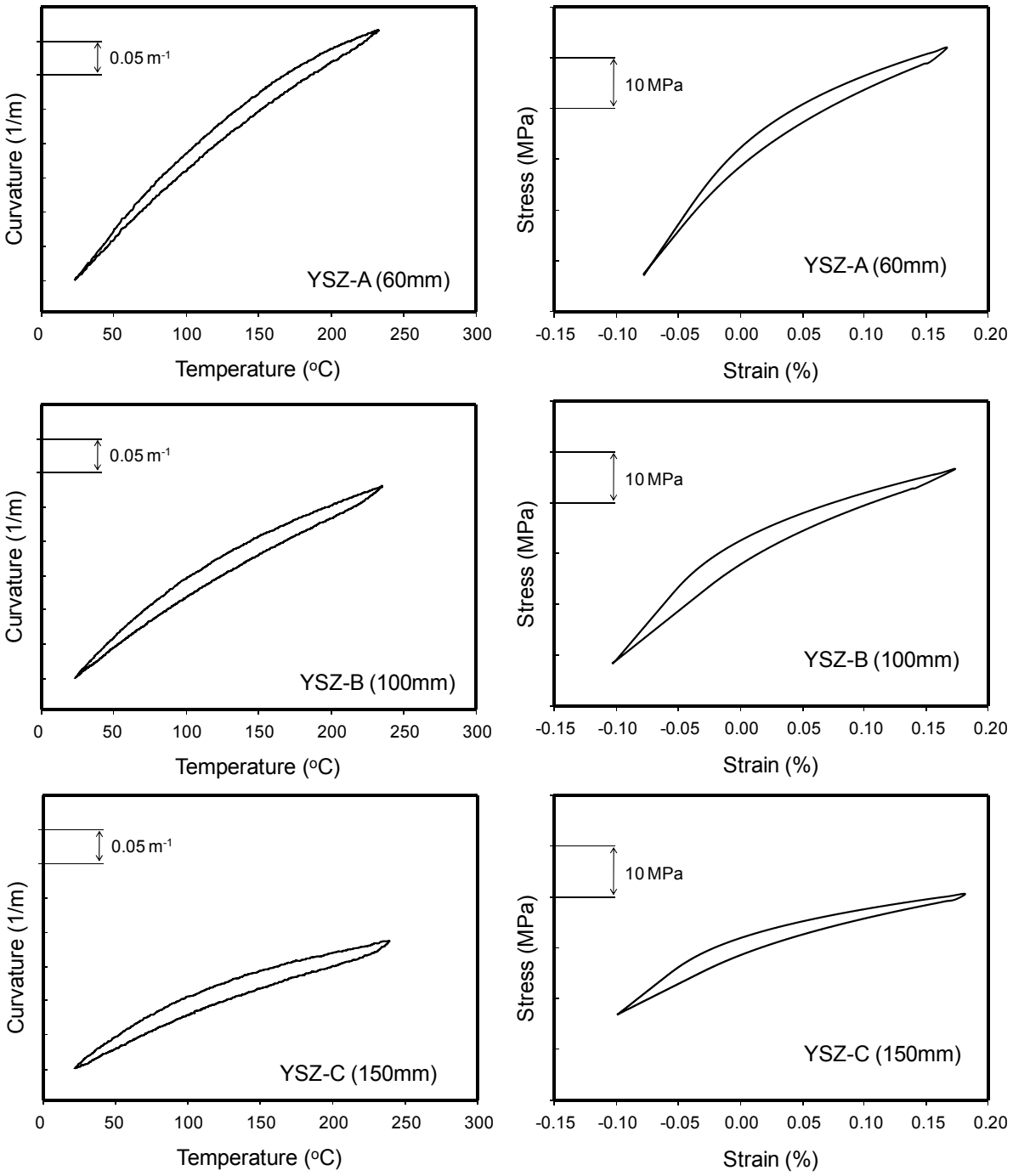

Figure 6.3: Curvature-temperature and stress-strain curves for the three coatings, YSZ-A, YSZ-B and YSZ-C. YSZ-B exhibits larger hysteresis area than YSZ- C, however the hysteresis degree is higher for YSZ-C as the area is normalized to the total stress-strain change[50].

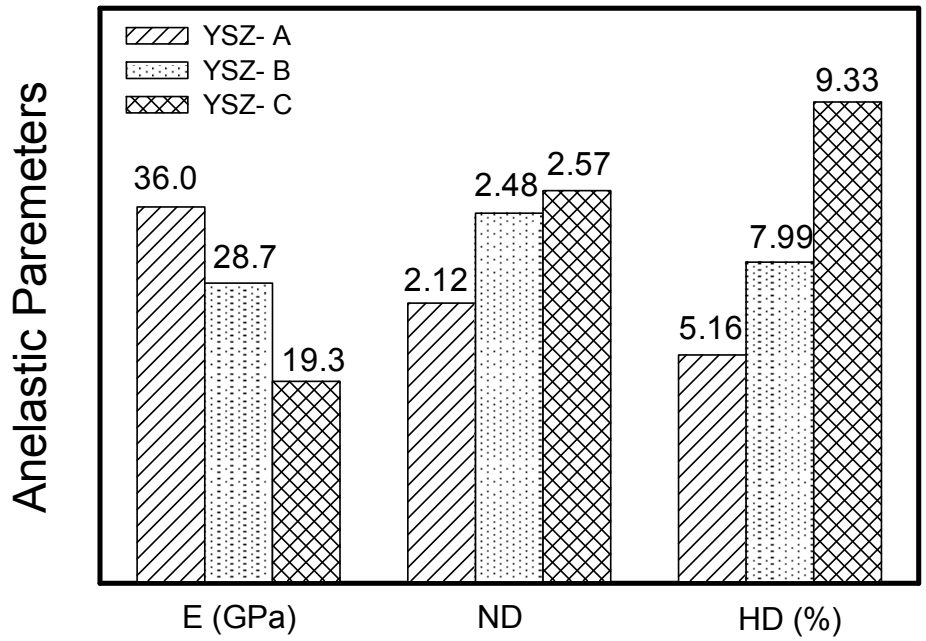

Figure 6.4: The three anelastic parameters for the YSZ- A, B and C coatings sprayed at three different spray distances, 60, 100 and 150 mm respectively[50].

In Figure 6.4, all three parameters show clear and consistent trends as the spray distance is changed. For the linear elastic tangent modulus at lower strains, YSZ-A is nearly twice as high as YSZ-C. The lower porosity and fewer interfaces in YSZ-A as observed in Figure 6.3 produce stiffer response. As opposed to the modulus, non-linear degree (ND) increases with spray distances. This parameter is primarily attributed to the density of thin micro-cracks and the results suggest higher density of such cracks in YSZ-C. A larger variation is observed in the hysteresis degree (HD), which is the normalized closed area of the stress-stress curves. The largest *HD* in YSZ-C specimen indicates greater presence of interfaces, intra-splat boundaries and cracks. Essentially, a greater frictional sliding causes a larger difference between the loading and unloading stress-strain curves.

The above HD values were extracted from the stress-strain loop area of the coatings. However an alternative approach can be considered for HD calculation from curvature-temperature data of the coatings, where the loop area of curvature-temperature plot is normalized to the total change in curvature and temperature experienced by the coatings. Figure 6.5 presents the two different HD values obtained from the stress-strain and curvature-temperature plot for coatings YSZ-A , B and C. The two HD values are different for each case; nevertheless their trends are notably similar. Both the HD values increases with shorter spray distances.

These results provide a simple method to compare coatings' HD extracted from curvature-temperature plots eliminating the data processing associated with stress-strain curves calculations. In the following sections of the dissertation, the later approach will be used for HD calculations.

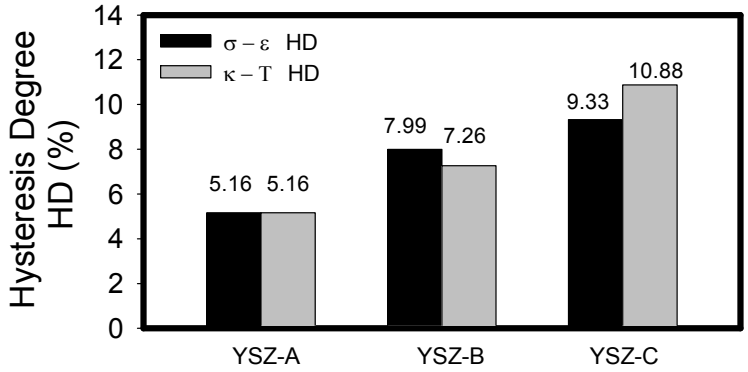

Figure 6.5: Hysteresis degree obtained from curvature-temperature plot and the stress-strain curves for the three coatings, YSZ-A, B and C. The absolute values from the two different calculation methods are somewhat different; however their trend is almost similar.

6.2. Spray particles energies

Controllability of anelastic behavior was also examined by varying particle states (particles' T&V) during spray processing. This was accomplished by changing the plasma power and the total gas flow of the plasma plume. Three specimens were fabricated with three different plasma energies labeled as low energy (YSZ-D), medium energy (YSZ-E) and high energy (YSZ-F). Again YSZ-HOSP powder was used to process the coatings. Table 6.1 shows the input parameters used for the deposition. All other processing parameters, including the spray distance, were kept constant. Figure 6.6 shows the particles T&V distributions for the three conditions, and similar to section 6.1, melting index and kinetic energy distributions were also plotted for analysis.

Figure 6.6 (a) shows the average T &V values for low, medium and high conditions. The three conditions were designed to be equally spaced in the T&V process map. However, a careful investigation of the MI-KE plot reveals somewhat different

interpretations (Figure 6.6 (b)). The MI distributions for the three cases are comparable with Med-E and High-E conditions showing almost identical distribution. The Low-E condition shows a broader distribution indicating that a large number of particles were less molten during spraying. Additionally, from the KE distribution of the particles it can be inferred that particles in Low- E conditions could not achieve higher KE (max KE ~ 1.5 mJ). In short, the low-E condition was significantly different from the Med- E or High- E conditions, and these fine details could not be interpreted from the average values of T & V.

Condition	Ar (slpm)	H_2 (slpm)	Current (A)	Output Power (kW)
Low	35.2	2.6	450	24.3
Med	47.5	6	550	33.9
High	59.7	11.1	650	45.5

Table 6.1: The plasma input parameters and measured output power for the three conditions. The spray distance and raster speed were kept constant at 100 mm and 500 mm/sec.

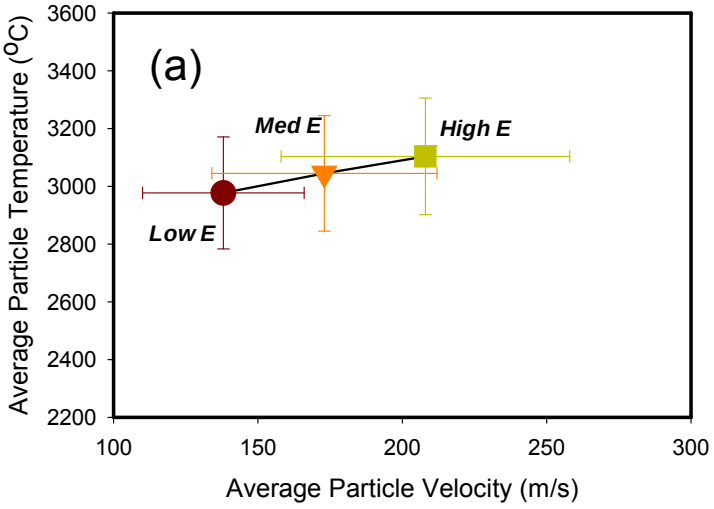

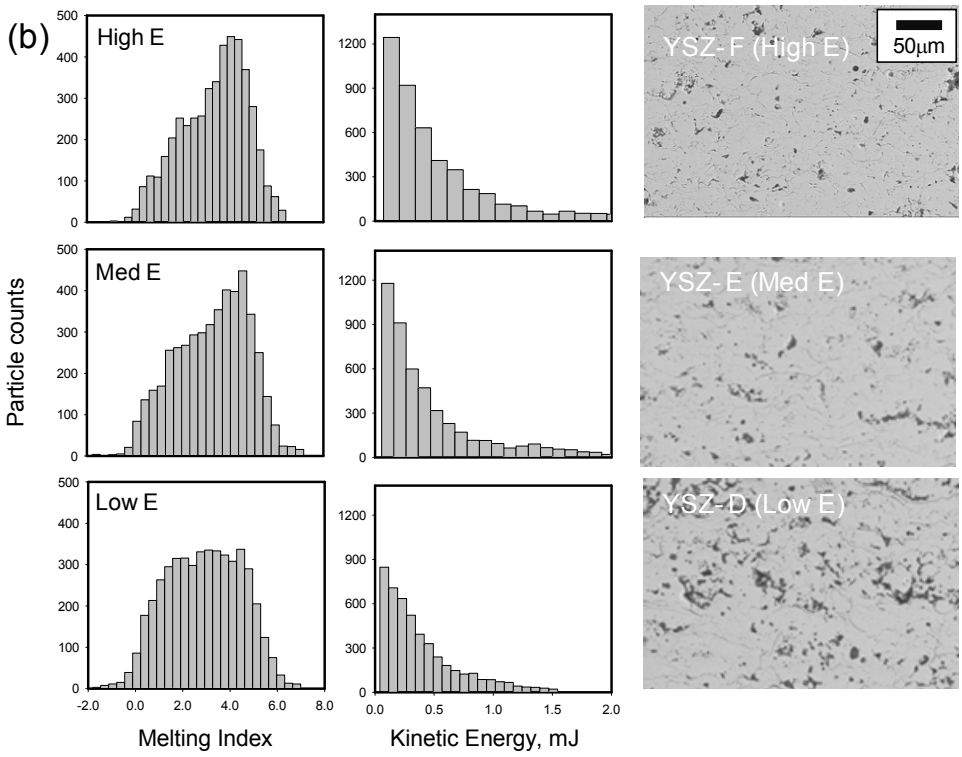

Figure 6.6: (a) Average T & V measured with DPV2000 sensor for coatings sprayed with three spray distance. YSA-D (Low E), YSZ-E (Med E) and YSZ-F (High E). (b) shows the melting index and kinetic energy distribution of the particles corresponding to the three coatings with their SEM micrographs. YSZ-D coating shows higher porosity and splat interfaces due to overall low melting index among the three coatings

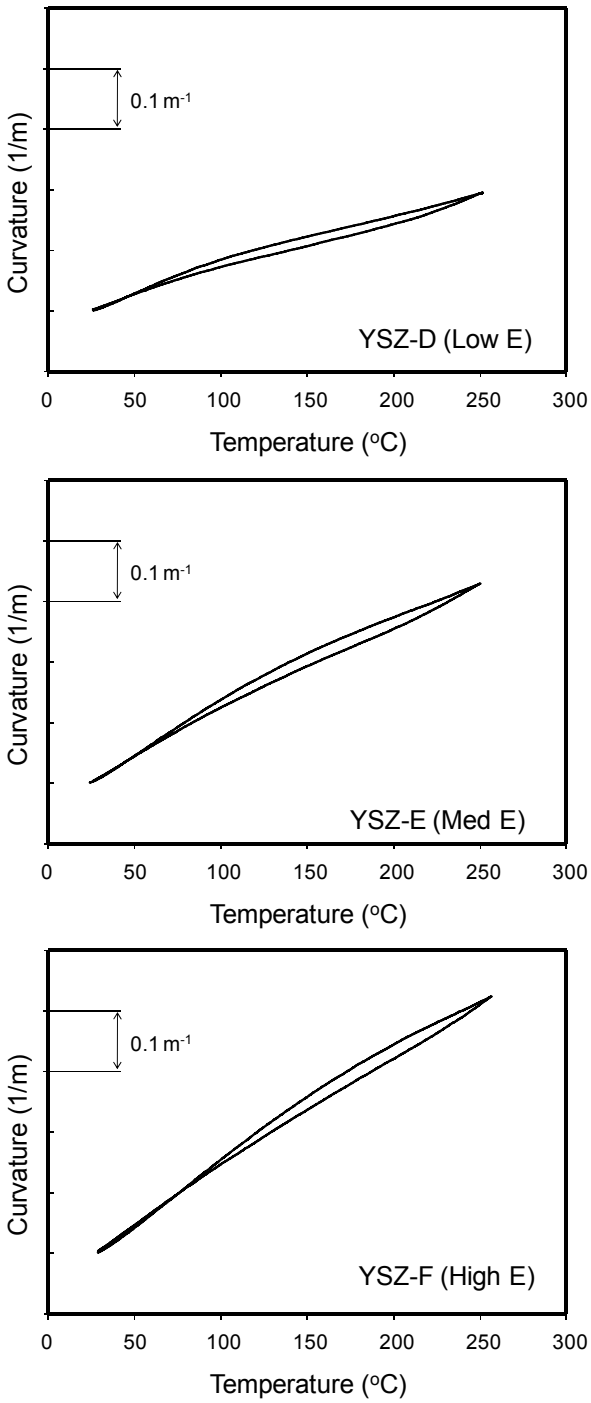

Figure 6.7: Curvature-temperature curves for the three coatings sprayed with three different plasma energies, YSZ-D, YSZ-E and YSZ-F[50].

The measured curvature-temperature records (Figure 6.7) were processed, and their stress-strain relations were obtained to compute the anelastic parameters for the three coatings (Figure 6.8). The HD values were calculated from the curvature-temperature

curves rather than from their processed stress-strain data. Figure 5.30 shows the SEM images of the three coatings.

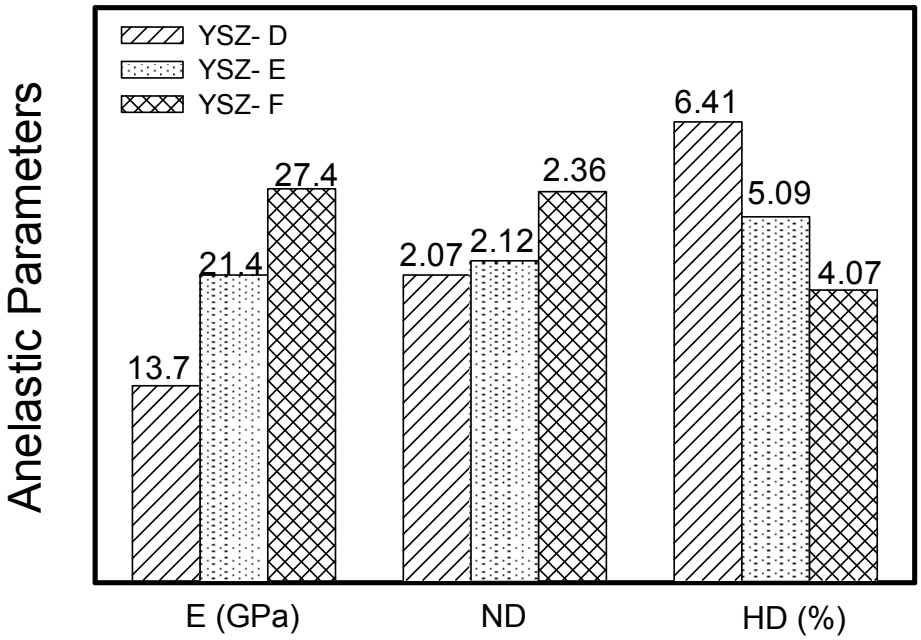

Figure 6.8: The three anelastic parameters for the coatings sprayed at three different plasma energies. YSZ- D, E and F corresponds to Low, Medium and High energy conditions respectively[50].

YSZ-F has the highest *E* as the high energy particle impacts produce lower porosity and stiffer coating. The non-linear degree (ND) parameters are more uniform among the specimens, which could be due to the high thickness of the coatings. However, as opposed to the trend shown in Figure 5.25 for YSZ- A, B and C coatings, it increases slightly as the modulus is increased (from YSZ-D to F). With largest *ND*, a higher density of thin micro-cracks is predicted in the high energy specimen (YSZ-F), as the particles with high melting flatten better and produce larger number of microcracks within the splat during solidification. This trend is clearer in *HD* results as the hysteresis is reduced in YSZ-F specimen. Perhaps, large energy impacts caused stronger bonding at interfaces and inhibited frictional sliding during loading cycle, and lower hysteresis.

6.3. Coating deposition Pattern

Three coatings YSZ-G, YSZ- H and YSZ- I, were sprayed with different raster patterns using YSZ-HOSP powder. Figure 6.9 displays the details of deposition pattern and raster speed of the plasma torch used for fabrication of these three coatings. Two of

the coatings were sprayed on ICP sensor; one with robot raster along-the-length of substrate (YSZ- H) and another with raster along-the-width (YSZ- I) of substrate. On the other hand, the third coating (YSZ-G) was sprayed vertically on a spinning carousel (72 rpm) with robot movement (5 mm/sec) parallel to the spinning axis of the carousel (batch- 3 in section 5.5). This pattern provided an along-the-width deposition at an angle (~ 3^{o}). Also, for each revolution of the stage, the specimen was against the torch only for 0.21 seconds, which is ~1/6th of the time for one revolution. Therefore, the coating was significantly cooled between the two consecutive contacts with the plume. Clearly the three patterns are significantly different among themselves. The other processing parameters and conditions including gas flow rate, gun current, feed rate and spray distance were kept constant.

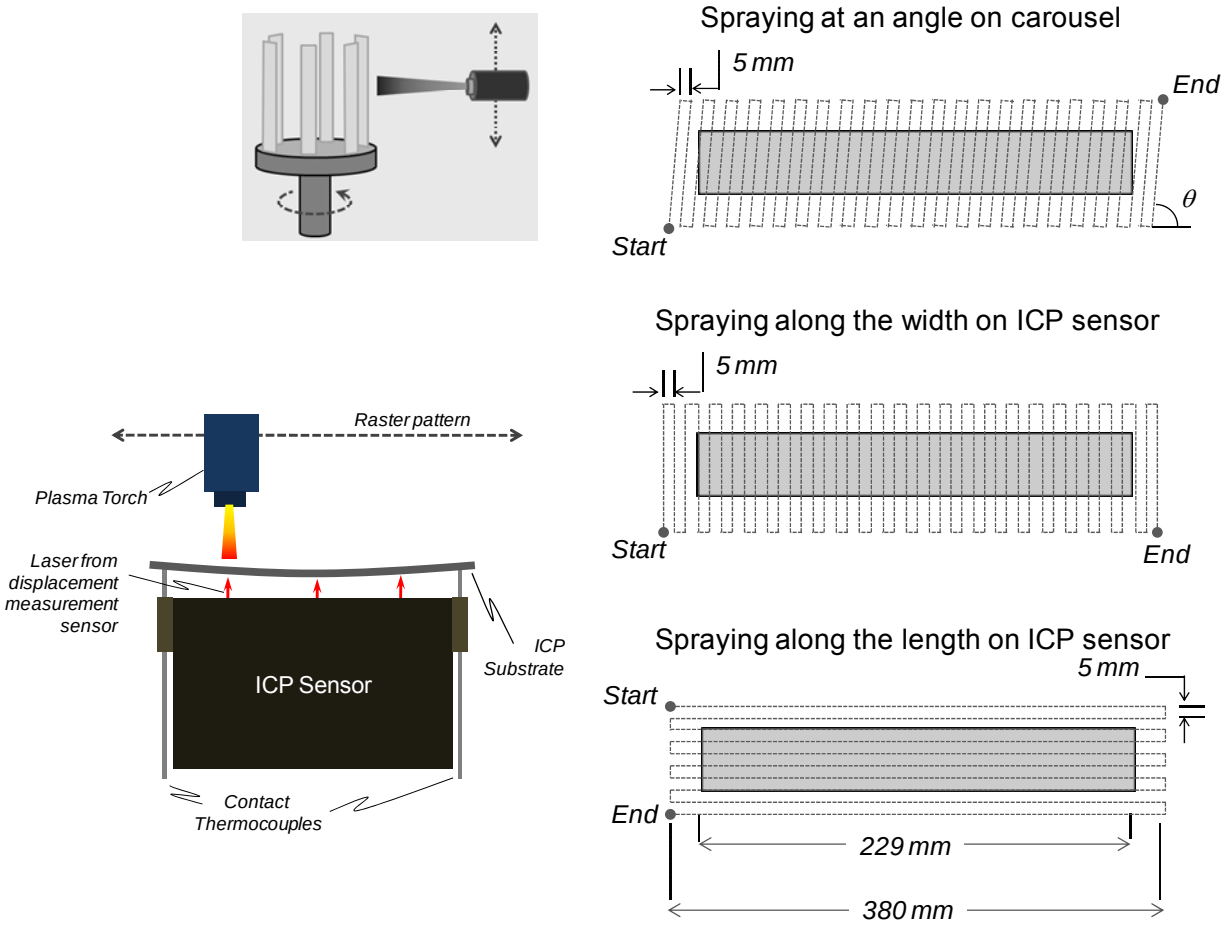

Figure 6.9:: Schematics of raster pattern used for the deposition of coatings YSZ-G, H and I.

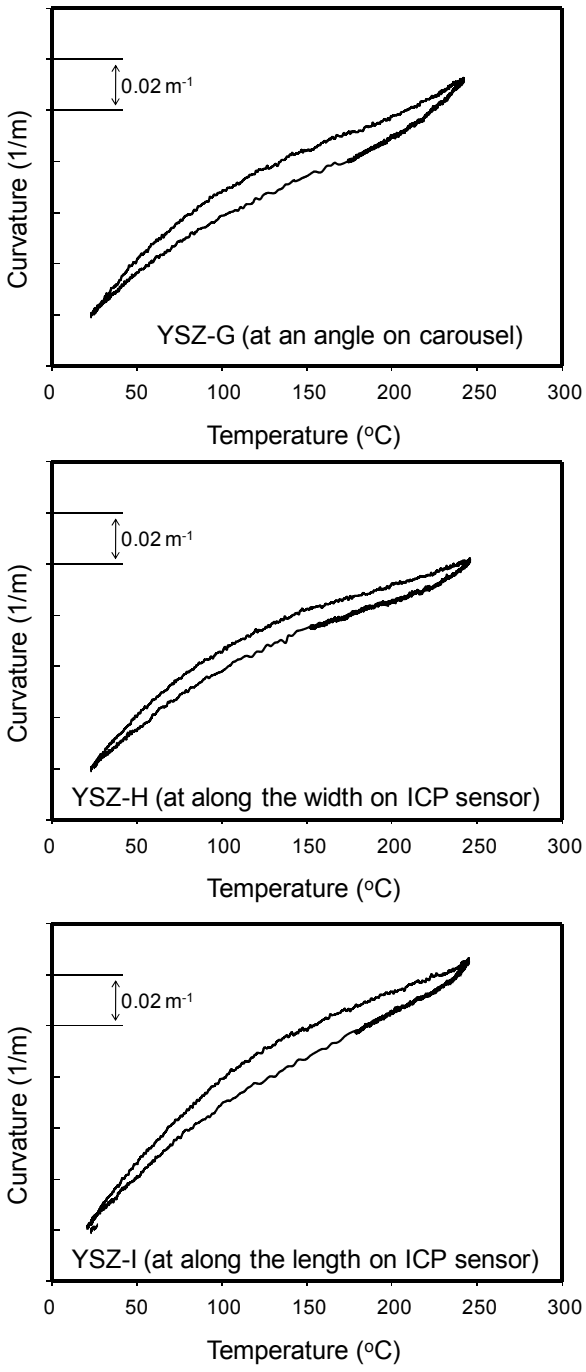

Figure 6.10: Curvature-temperature curves for the three coatings, YSZ-G, YSZ-H and YSZ-I. The visual inspection of the curves suggests that the coating sprayed with different deposition pattern exhibit different anelastic response.

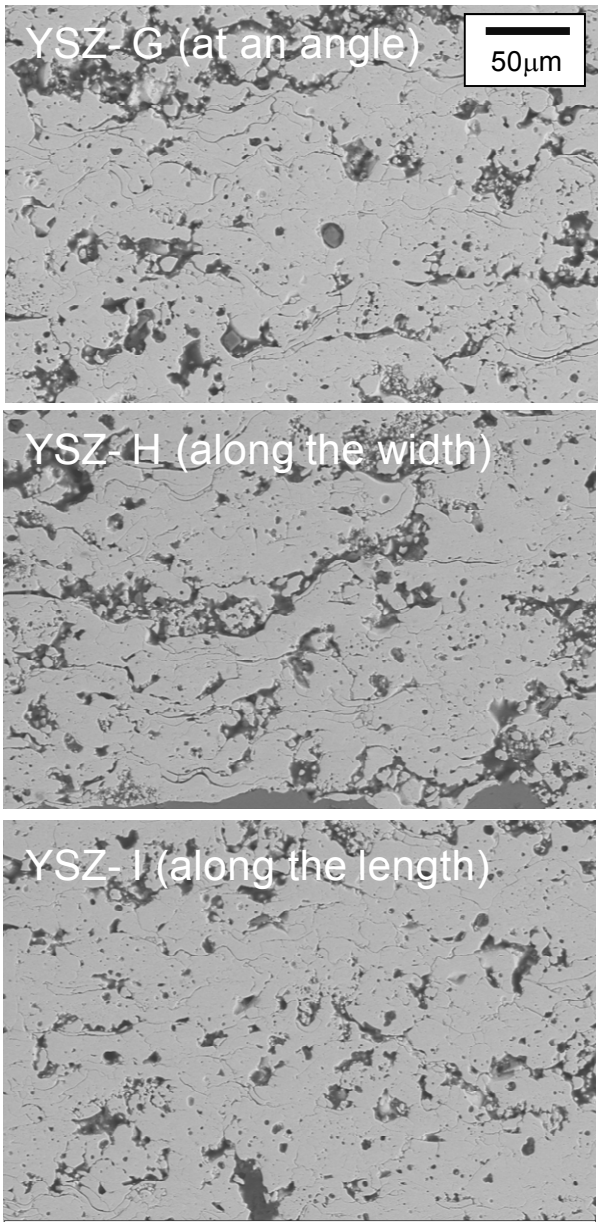

Figure 6.11: The anelastic parameters of the three coatings sprayed with different deposition patterns. The coatings sprayed on ICP sensor display significantly different microstructures.

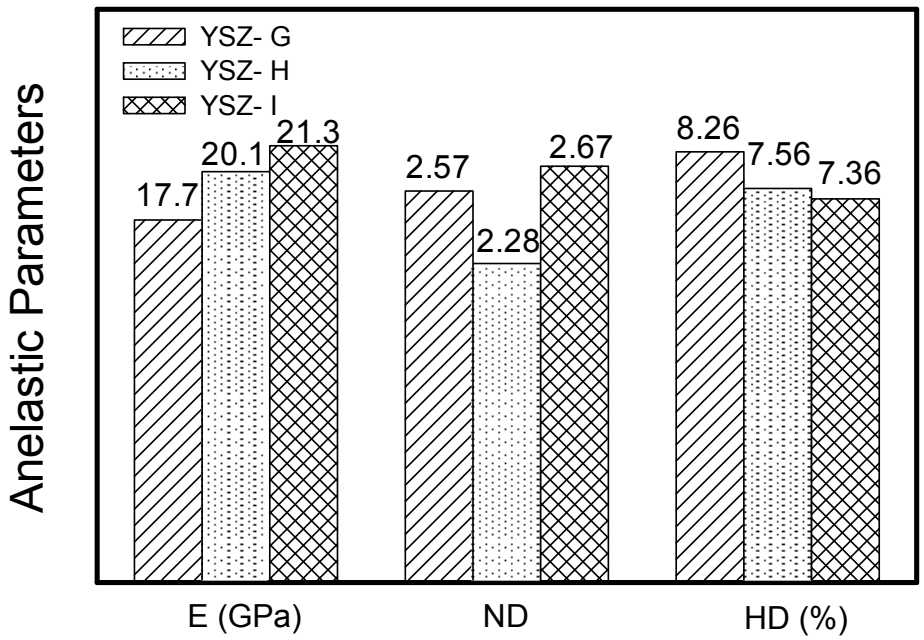

Figure 6.12: The anelastic parameters of the three coatings sprayed with different deposition patterns.

Figure 6.10 shows the curvature-temperature plots for the three YSZ coatings obtained from the thermal cycle test. Figure 5.34 exhibits the anelastic parameters calculated by processing the curvature-temperature plots, and Figure 6.11 displays the SEM micrographs for the three coatings. Figure 6.12 shows the differences in the anelastic properties of the three coatings. The relatively lower value of ND for coating YSZ- I as compared to the other two suggests that the number of crack density is lowest in this coating, which can also be seen from the SEM micrograph of the coating. YSZ- G has the lowest E among the three, which can be attributed to the higher porosity level (Figure 6.11) achieved due to time lag between two consecutive spraying strokes by the torch. The cooling of specimen in one revolution of carousel stage would have lowered the substrate temperature, which eventually led the depositing particles to poor flattening.[56] On the other hand, the ND parameters of YSZ- G and YSZ- H exhibit an interesting difference. The former one with low E shows higher ND than YSZ- H. This can again be attributed to the higher porosity in YSZ- G. The YSZ-I coating shows highest ND and E and lowest HD. This coating was sprayed with along-the-width pattern, which must have raised the local deposition temperature significantly and provided a locally denser coating. On top of that the coating might have gone through microcracking to compensate the local residual stresses. That is why this coating shows higher ND. There could be several other factors, such as overall and local deposition temperatures of the substrate etc, which may contribute to the overall anelasticity of the

coatings. Nevertheless it is worthwhile to note that different deposition patterns can provide different degree of anelasticity of a coating.

Industrial relevance of above results

The above three case studies of 9 different coatings also have significant industrial relevance. For example, the turbine parts are not flat; therefore it is highly possible that the spray distance between plasma torch nozzle and the part's surface is not constant during deposition, which is relevant to the study in section 6.1 Also, the change in plasma enthalpy for a given process parameter is also possible. For example, hardware degradation during extended operating time of the torch can change the plasma chemistry and consequently the particle-plasma energy transfer (section 6.2), which can produce coatings with different microstructures. Furthermore, it is quite common in practice to spray a part on a rotating table, where one surface of the part appears to get coated after one rotation (section 6.3). Though, the above experiments exhibit only certain conditions of geometric process variability that can take place during an actual turbine part deposition, it points to potential sources of intrinsic spatial variability in coating properties due to subtle changes in processing conditions.

7. Role of interface character on anelastic behavior

7.1. Topological modification of defect surfaces

In the single crack model by Liu et al, it was concluded that the frictional characteristics of the crack faces governs the hysteresis component of the anelastic behavior of the ceramic structure. Therefore, in plasma sprayed coatings, the surface texture of interfaces and defect faces can affect frictional energy loss during the thermal cycling, which can influence the hysteretic response of a coating. In the case of crystalline materials such as YSZ, splat surfaces comprise of nanoscale roughness associated with uneven grain terminations arising from columnar solidification (Fig. 7.1). Furthermore, the cracking within a splat due to rapid solidification can provide wavy surfaces which can alter the frictional sliding mechanics among the splat interfaces. However, there are certain ceramic materials which produce amorphous structures due to the rapid quenching occurring in plasma spray, where lack of any columnar grain eliminates the existence of any grain terminations while retaining other microstructural defects such as globular pores interfaces. This provides a methodology to investigate the role of interface roughness and character on the anelastic response of otherwise similar plasma sprayed ceramics. The following study is thus focused on the anelastic behavior of a class of ceramic materials, such as Mullite ($3Al_2O_3.2SiO_2$), Cordierite ($Mg_2Al_4Si_5O_{18}$) and Forsterite (Mg_2SiO_4), which are well known for producing amorphous coatings during deposition.

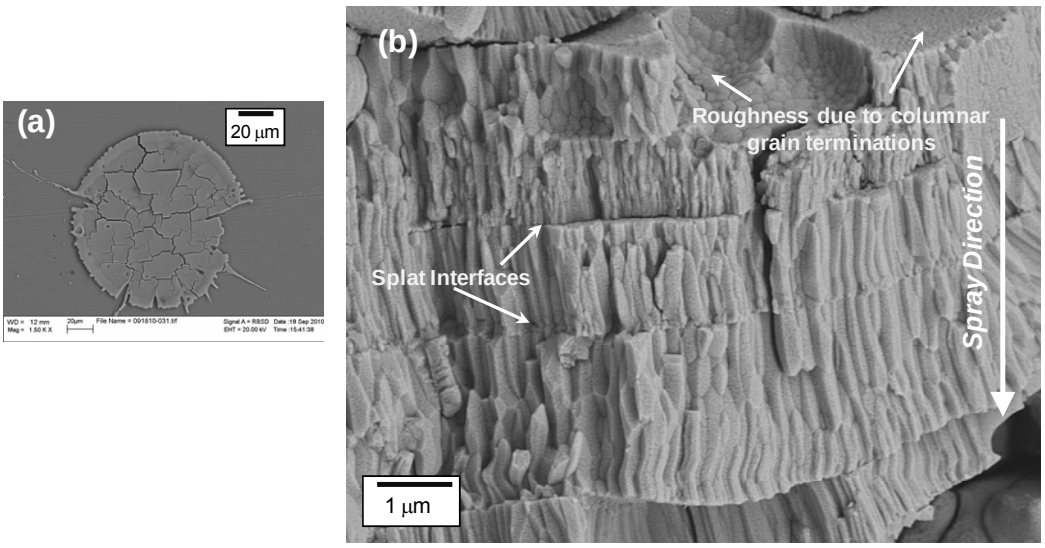

Figure 7.1: (a) exhibits surface roughness introduced due to cracking within a splat. (b) fractured surface of PS YSZ coating showing the nano-scale roughness on the splat surface due to columnar grain termination[50].

To investigate the effect of surface roughness on coating anelasticity, coatings with the two aforementioned materials were deposited on the standard ICP substrates. The processing conditions were kept constant at their standard values (center condition of the process map). Figure 7.2(a) shows the splats morphologies of three powders and one can easily observe that none of these powders underwent crystallization; therefore the mechanism of cracking within a splat was missing. The sizes of splats are different in each case, which can be attributed to the different size distribution of the powders. An XRD study conducted on the two coatings exhibited the amorphous nature of the coatings (Figure 7.3). The degree of crystallinity appears to be different in the three cases, with forsterite coating showing higher number of crystalline peaks than mullite coating followed by cordierite coating. The XRD pattern of the three feedstock powder exhibited the presence of crystalline phases, therefore the peaks observed in the coatings correspond to the crystalline nature of unmolten particles. The peak identification is outside the interest of this study, nevertheless our focus here is the splat roughness attributed to the crystallanity associated with the coatings.

The high magnification micrographs of fracture surfaces of the three coatings (Figure 7.2 (a and c)) show smooth splat surfaces as well as no intra-splat columnar grains and cracks, generally observed in crystalline coatings. Figure 7.2 (b) shows the higher porosity in cordierite coating than the other two. Additionally Figure 7.1(c) exhibit the presence of crystalline splats in the case of forsterite coatings, which can be correlated with the peaks observed in its XRD plot (Figure 7.3).

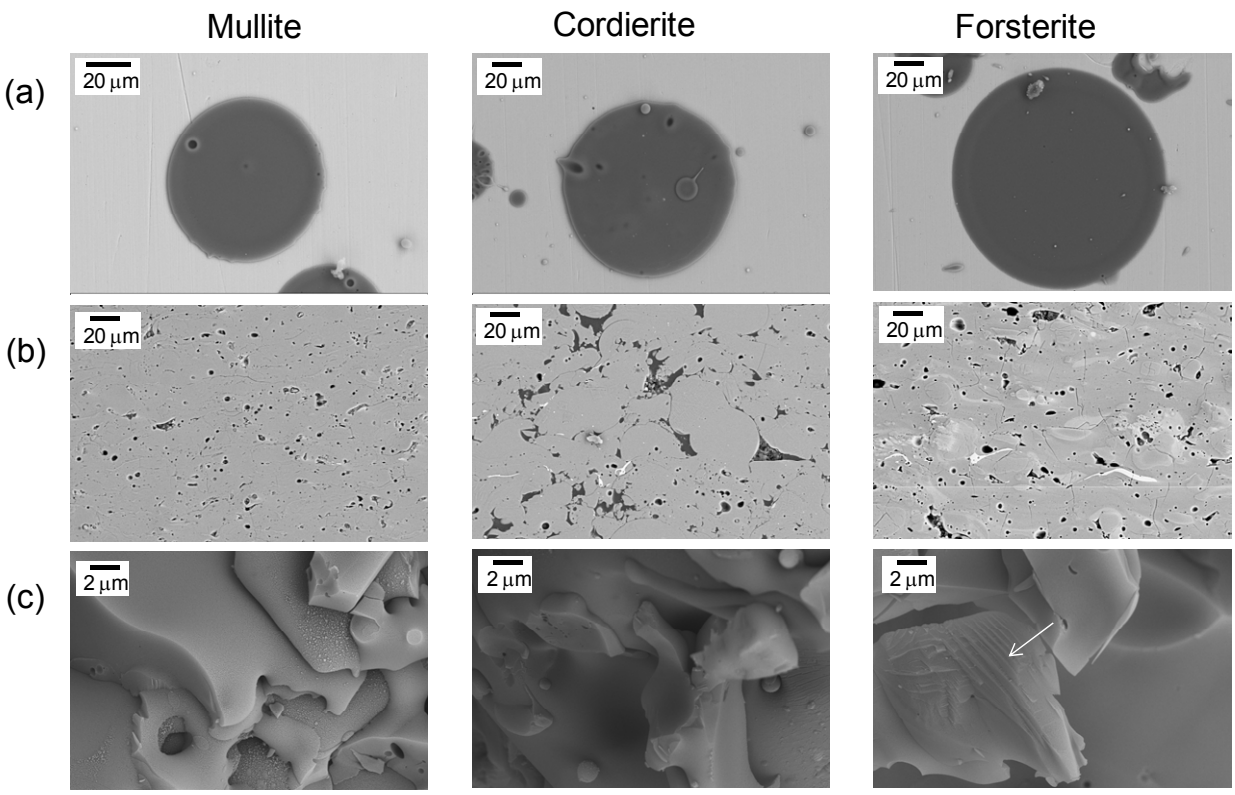

Figure 7.2: SEM micrographs of (a) splats morphology and (b) polished and (c) fractured cross sections of the three amorphous coatings, mullite, cordierite and forsterite. None of the three coatings display any sign of cracking at splat levels, however some crystallinity can be observed in forsterite coating.

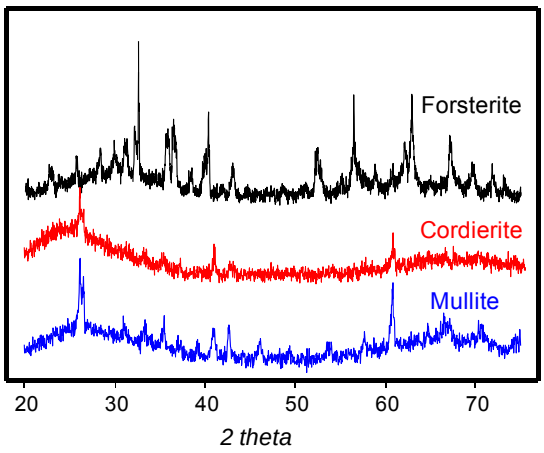

Figure 7.3: XRD data of the three amorphous coatings. Forsterite coating shows more number of peaks than Mullite and cordierite coatings indicating higher degree of crystallinity associated with it.

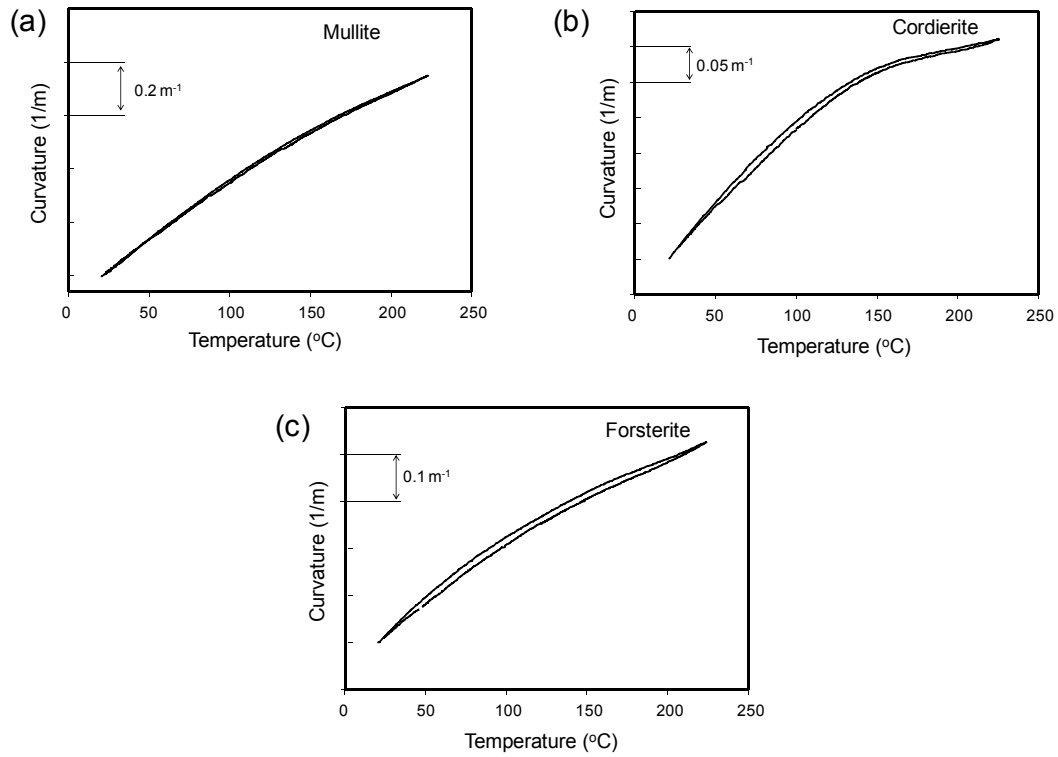

Figure 7.4: Curvature-temperature responses of three amorphous coatings obtained from BCT measurements. Cordierite coating shows highest non-linearity among the three attributed to its high porosity content. All three coatings exhibit limited hysteresis in their anelastic behavior.

The BCT measurement tests produced interesting curvature-temperature data for all three specimens as shown in Figure 7.4. Like the curvature-temperature of YSZ specimens, they all are clearly nonlinear with respect to the temperature change; however the observed hysteresis is very limited in the case of mullite and cordierite coatings. The forsterite coating, however, exhibits noticeable degree of hysteresis in its curvature-temperature plot. A preliminary explanation for the overall low hysteretic responses of these coatings is that the low roughness of the glassy surfaces within the interlamellar interfaces in amorphous materials offer little or no friction during cooperative sliding, and thus does not contribute significantly to energy dissipation. The hysteresis loop area appears to increase with the increase in crystallinity of the coating, which can be attributed to the presence of crystalline phase presence in the the coating offering relatively rougher interfaces. The nonlinearity, on the other hand, is produced by many existing micro-cracks and unbonded splat interfaces, and it was largest for the case of cordierite coating.

Coating	Coating Thickness (mm)	Coating CTE, x 10^{-6} (/°C)	Substrate Thickness (mm)

Mullite	0.39	5.4	2.23
Cordierite	0.33	3.8	2.25
Forsterite	0.41	10.5	2.25

Table 7.1: Thickness and CTE value used for the calculation of anelastic parameters of the three amorphous coatings

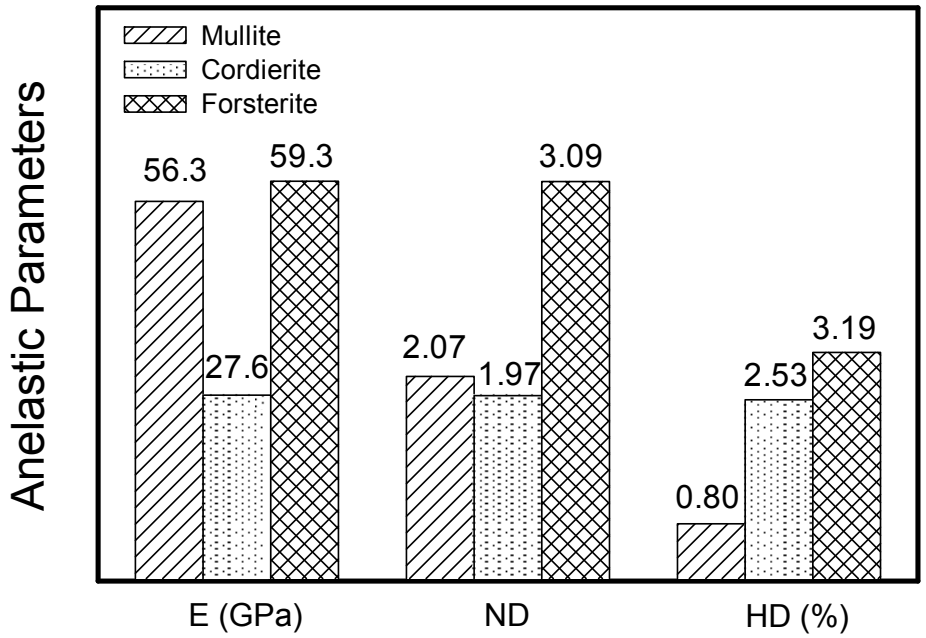

Figure 7.5: Anelastic parameters of the three amorphous coatings. Both the ND as well as HD are lower in the case of mullite coating.

The substrate and coating thicknesses and CTE values for these coatings are reported in table 7.1, and the anelastic parameters of these three materials are summarized in the bar graphs in Figure 7.5. The quantified parameters represent a true comparison among the coatings. Both the coatings show lesser HD than a typical crystalline YSZ coating (HD > 5%). The HD was higher for the forsterite coatings as it possessed the highest degree of crystallinity among all three as observed in the XRD measurements. The comparison of these amorphous coatings with the crystalline coatings, such as YSZ, supports the fact that interfacial frictional sliding is the primary contributor to hysteresis. The above results indicate an interesting possibility of controlling anelasticity of coatings through combination of materials and process modifications.

7.2. Interface surface modification by introduction of salt to the coatings

7.2.1. Immersion of a PS YSZ coating into a salt solution

The porous nature of the plasma sprayed materials allows introduction of secondary phases via aqueous or chemical infiltration treatment, which can alter the frictional properties at the defect interfaces, and hence the anelastic properties. In other words the deviation in anelastic properties can confirm the presence of a foreign media. This phenomenon is quite relevant to TBCs, as the coatings face a variety of environmental conditions with traces of salt, ash, dust etc. Therefore, this demands an extra measure of care in coating design which may change due to a short exposure to a different media. To understand this, a 0.27 mm thick YSZ coating (YSZ- J) on a standard ICP substrate with a thickness of 1.6 mm was deposited and then dipped in a 2M NaCl solution for 36 hours. This allowed the salt solution to effectively penetrate the interlamellar regions of the sprayed microstructure. The BCT measurement was made before and after the salt immersion. After that, in order to wash out the salt, the coated specimen was further immersed in water for 18 hours. Again the specimen was thermal cycled and its anelastic properties with different solution treatment were calculated. Since, the first cycle of the day shows a different curvature-temperature response; only second cycles for all three cases are used for the comparison (Figure 7.6). The HD was estimated from the curvature-temperature plot, while the non-linear parameters (ND and E) were calculated only from the heating part of it (Figure 7.7).

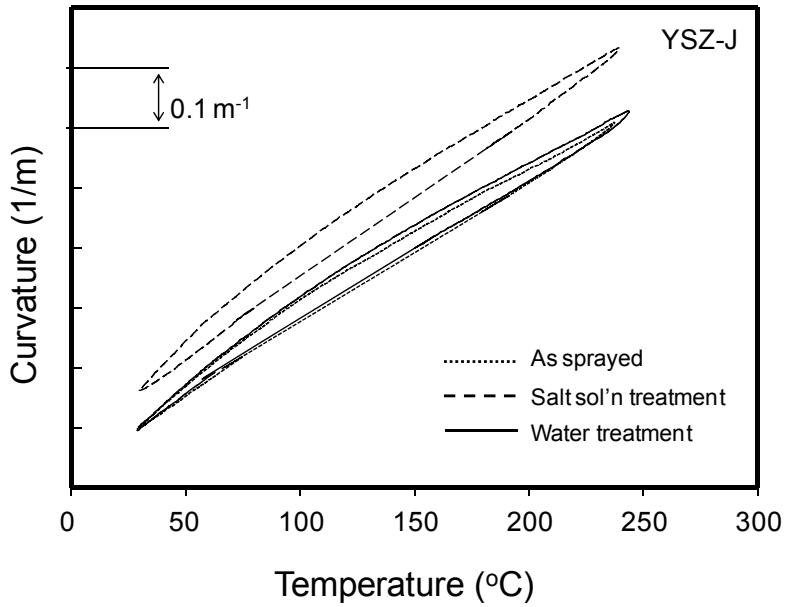

Figure 7.6: Curvature-temperature response of YSZ- J coating after treatment with salt solution followed by water. The response after salt solution treatment is shifted in Y-axis for clarity

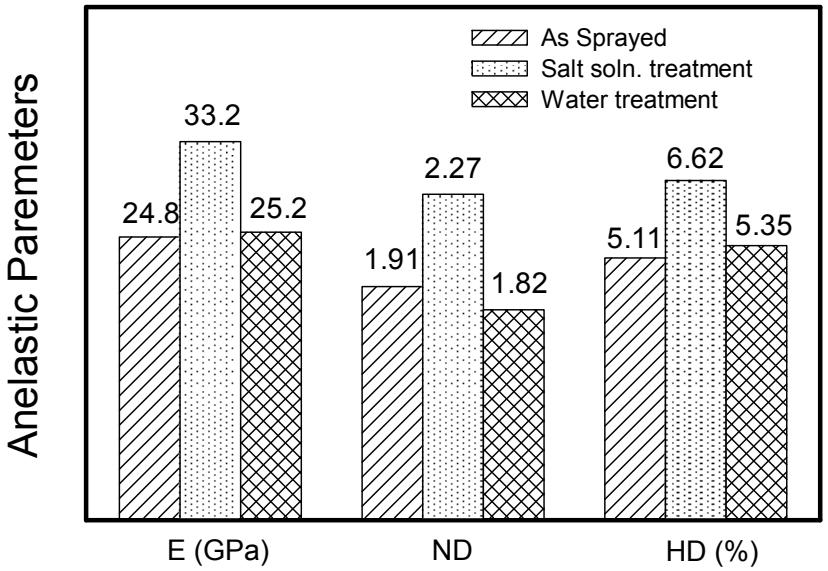

Figure 7.7: Curvature-temperature response of YSZ- J coating after treatment with salt solution and then water. The response after salt solution treatment is shifted in Y-axis for clarity.

The specimen immersion in two different solutions exhibited many interesting characteristics. Since all the measurements were conducted on a single specimen, hence

a direct comparison of curvature-temperature behavior of the coating-substrate system with different treatments could easily be made without any erroneous interpretations. Following observations can be made from the Figure 7.6 and 7.7.

- During the first thermal cycle, water evaporated from the specimen, leaving behind residue of salt within the interfacial regions of the coating. Due to water evaporation, this first thermal cycle was significantly different in terms of curvature-temperature relations as compared to the as-sprayed materials, it was a transient phenomenon.

- The second, third and additional cycles resulted in highly repeatable curvature-temperature relations and behaved in ways similar to the as-sprayed material. However notable differences were observed in both stiffness and the magnitude of the hysteresis loops compared to the untreated material.

- The curvature-temperature results shown in Fig. 7.6 indicate stiffer response with the salt solution immersed coating. In addition, the hysteresis loop area was larger for the case of immersed coating. On the other hand, the temperature-curvature records for 18 hours water immersion after salt treatment suggests that the coating tries to behave like as-sprayed coating as salt washes out.

- Figure 7.7 shows the quantified values for these changes. As noted in the figure, the elastic modulus, E, increased about 30% after salt immersion and reduced back to the value for as-sprayed coating. Similarly, the hysteresis effect exhibited an increase of about 30%, indicating a greater frictional dissipation with salt phase deposited along the interfaces and cracks, and it returns back to 4 % as salt at the interface gets dissolved in water.

The above design of experiment enhances the understanding of the contribution of defect surfaces to coating anelasticity. To a first approximation, it provides evidence of change in anelastic behavior of coating with a slight change in ambient condition (media), and it also exhibits that up to a certain extent this modification is reversible. This experiment opens up an opportunity to design structural as well as functional composites by introducing an appropriate media to these coatings.

7.2.2. Effect of salt immersion on the anelasticity of amorphous coatings

In section 7.1 we discovered that the hysteresis present in a coating depends on the degree of crystallinity, and later in section 7.2.1 we concluded that this hysteresis can be altered by introduction of a foreign media. Another set of experiments was designed to examine the effect of salt solution immersion on crystalline/amorphous coatings. For that, the two amorphous coatings, mullite and forsterite discussed in section 7.2.1 were immersed in 2M salt solution for 36 hours. The BCT measurements were conducted and their curvature-temperature records were plotted (Figure 7.8). By visual inspection of the plots it can be observed that salt residues were not able to affect the hysteresis in mullite, while the change appears significant in the case of forsterite coatings. Figure 7.9 compares the anelastic parameters for these coatings before and after the immersion, and changes in all the three parameters were higher for the case of forsterite coating. As discussed above, the forsterite coating has more number of crystalline defect sites to produce higher anelasticity, and therefore the effect of salt gets magnified as it changes the characteristics of those defects. On the other hand, mullite coating is almost indifferent to the salt solution treatment. Remarkably, for both the coatings, all the three anelastic parameters were affected by the presence of salt residue in coatings, with forsterite showing higher degree of changes.

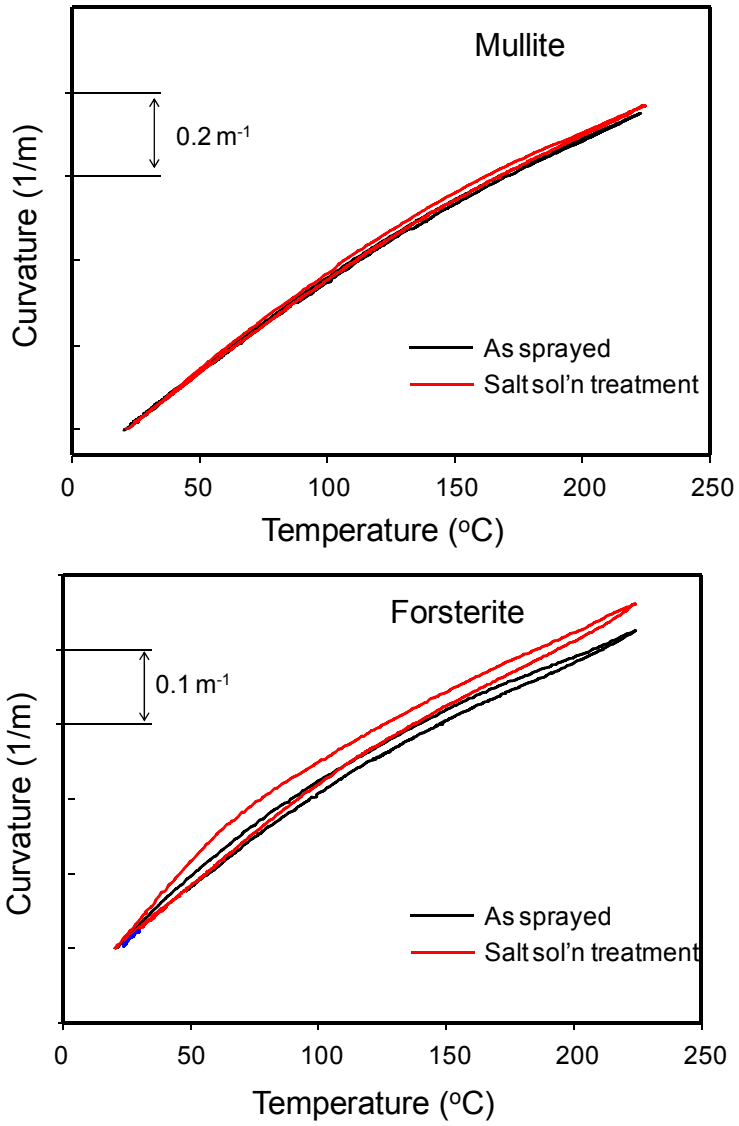

Figure 7.8: Curvature-temperature response of mullite and forsterite coatings before and after salt solution treatment. Forsterite shows higher degree of change in anelasticity than mullite.

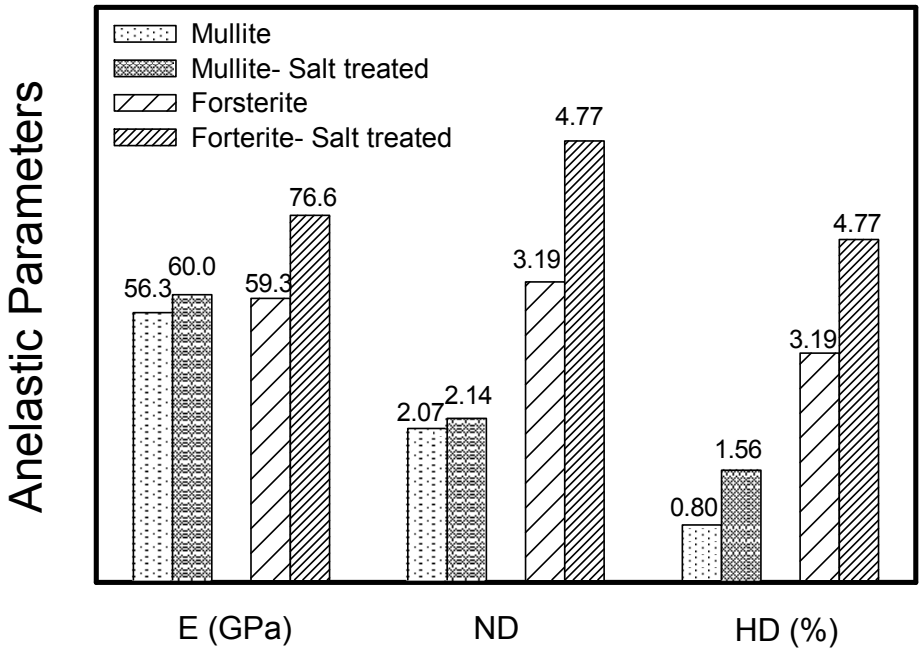

Figure 7.9: Anelastic parameters of the two amorphous coatings before and after salt solution treatments.

From these observations it can be concluded that the presence of foreign media itself cannot introduce hysteresis, however it is capable of changing it, in case it already exists in the coating.

7.2.3. Change in anelasticity due to introduction of salt during deposition

Apart from the immersion in a salt solution, another method to introduce a foreign media is by co-spraying along with the depositing material. A YSZ coating (YSZ- K) was sprayed on a 2.24 mm thick standard ICP Aluminum substrate (Figure 7.10 (a)). A jet stream of 2M salt solution at 0.2 liter per min was attached with the plasma torch aligned parallel to the plasma plume. The solution jet was turned on during every third pass out of the total 24 passes of the torch used for deposition, which amounts to total 8 passes being combined with solution spraying. The selection of salt solution spraying scheme was made after a couple of trial runs until the substrate temperature and coating thickness were similar to that of a routine deposition process. To compare the changes in anelasticity, another YSZ coating (YSZ- L) was fabricated with processing condition similar to the previous one (YSZ- K) except for the deposition with salt solution jet.

Figure 7.10 (b) shows the curvature temperature plots of the two coatings obtained from BCT measurements. Since, the thickness of the two coatings are comparable (~300 μm), a direct comparison of curvature-temperature plot is possible. The complete non-linear analysis could not be done on the salt-solution specimen due to limitations in the application of Nakamura's non-linear model to extract non-linear degree; however the elastic modulus and hysteresis loop area was calculated (Figure 7.11).

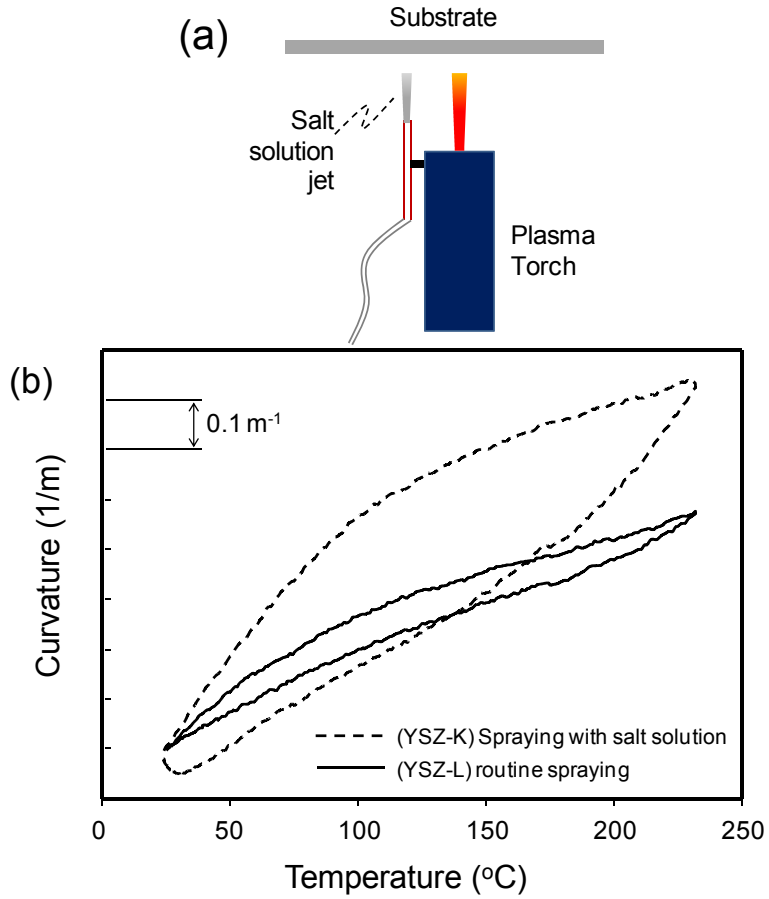

Figure 7.10: (a) schematic of salt solution spraying with coating deposition. (b) the curvature-temperature responses of the coating, YSZ-K and L. Coating sprayed with salt-solution jet shows very high degree of anelasticity.

The coating sprayed with salt solution exhibits a significantly stiffer, increasingly non-linear and larger hysteretic response than the coating with standard spraying. The deposit formation mechanism was completely different for the two deposition schemes, as the spraying of solution along with coating deposition might have reduced the local substrate temperature which can produce weak splat interfaces or intersplat bonding. Additionally, when the solution came in contact with a depositing particle it changed the particle melting state and the flattening ratio of the particle, which will change the overall architecture of the deposit.

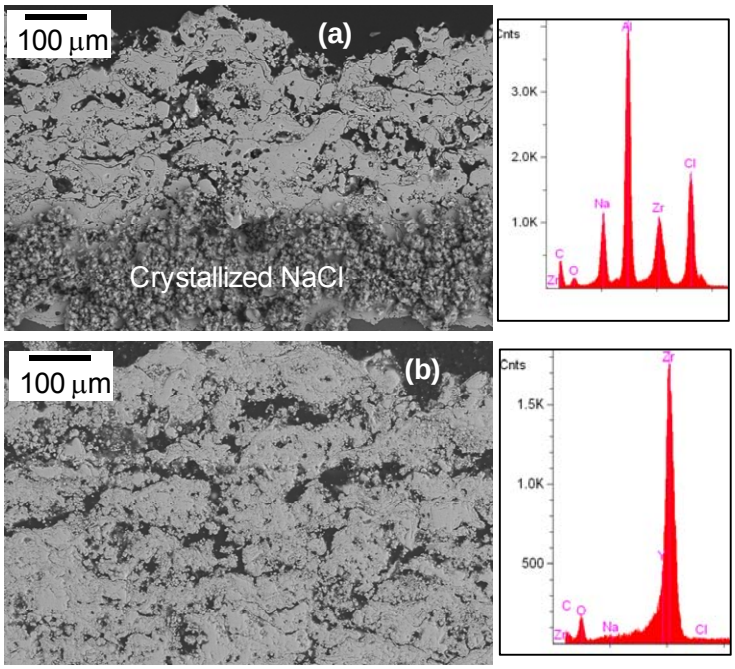

Figure 7.11: The SEM micrographs of YSZ-J coating cross section polished under (a) wet and (b) dry conditions. The EDS spectra of polished surfaces show presence of Na in the cross section polished under wet conditions. On the other hand the dry polished cross section does not show a significant Na peak suggesting a uniform distribution of salt in coating.

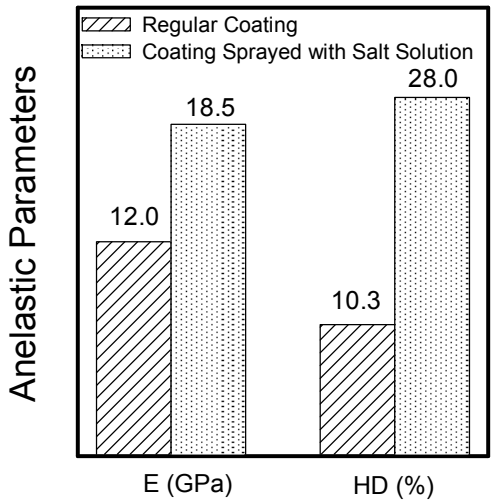

Figure 7.12: E and HD values for YSZ-J and K coatings. Both the parameters were higher for the case of coating deposited with salt solution stream.

Figure 7.11 shows the cross section SEM micrograph of the coating polished under dry and wet conditions. The figure 7.11 (a) shows a fluffy presence of NaCl (confirmed by EDS spectrum) at coating-substrate interface, which must have got dissolved during polishing and then crystallized upon drying of the mounted specimen. On the other hand, Figure 7.11 (b) does not show any such strong peaks of Na or Cl present in the EDS spectrum of the coating, which suggests that NaCl was homogenously present in the coating after deposition. Additionally, due to interactions between depositing particles and the spray stream, particles underwent quenching and re-solidification before reaching the substrate, which eventually introduced high porosity to the coatings (Figure 7.12). Furthermore, it is possible that due to high local deposition temperature the salt, remained after water evaporation, may have liquefy and instead of solidifying as crystals at defect surfaces, it formed a thin uniform layer at defect surfaces. In either case, the presence of salt at defect interfaces provided adequate friction to the sliding faces of the defects so that the coating was not only capable of providing almost 300% more hysteresis, but it also increased the elastic modulus more than 50% higher than in the case of the coating sprayed with no salt residue. Though, all these experiments belong to an extreme condition of salt solution spraying, the ability and understanding of controlling the anelasticity in this fashion is highly valuable. Also, the microstructural observations of the coatings provide a way to increase the porosity of a coating by spraying salt during deposition and then rinsing it away using water.

8. Mechanical equivalence of bi-layer curvature measurement at room temperature

The non-linear coating properties extracted from the curvature-temperature data during thermal cycling contains information on coating microstructure in terms of defects embedded in the coating. However, it is also important to characterize a coating's response against pure mechanical loading at an ambient temperature to eliminate any temperature effects. In the past, many researchers have reported the non-linear behavior of plasma sprayed ceramic coatings under mechanical loading [22, 47]. Not limited to the ceramics, the non-linear stress strain relation in through thickness tensile loading has also been investigated for thermally sprayed Ni-45Cr metallic coatings[25].

Among the various characterization techniques commonly used to evaluate elastic properties of materials, the four-point bend (4PB) test was adapted for the experiments. This loading method provides in-plane stress states similar to those present during thermal cycle test, which in turn enables a direct comparison of stress-strain results obtained from the two different types of loadings. Additionally, it demands limited additional sample preparation apart from the actual coating deposition; essentially coatings were separated from substrates as free-standing forms. Contrary to other techniques, e.g. uniaxial loading, and indentation tests[68, 69], the constant strain region obtained between the load span in 4PB test apparatus enables the extraction of coating properties with a sampling of sufficiently large volume of coatings. In the following section, some of the results on non-linear properties of coatings under mechanical loading will be discussed. Also, a comparison will be presented with the properties obtained from thermal cycle data.

8.1. Results and discussion

Following extensive experimental evaluation on the four-point bend setup (section 3.7), it was observed that the unloading curve is more sensitive to the crosshead reversal

towards the initial state. Therefore, only the loading section was considered for further stress-strain analysis. The load displacement records were converted to obtain corresponding curvature-moment curves for the coatings. Figure 8.1 (a) shows the curvature-moment curve obtained from load-displacement curve measured by the 4PB test. The moment and curvature data is then processed for the calculation of stress-strain curve of the coating (Figure 8.1 (b)).

Similar to the BCT thermal cycle test, the non-linear analysis of load-displacement data yields two main parameters, elastic modulus (E), and degree of non-linearity (ND) from the stress-strain relationship. The details of the formulation and calculation associated with the stress-strain processing have been reported in reference [57].

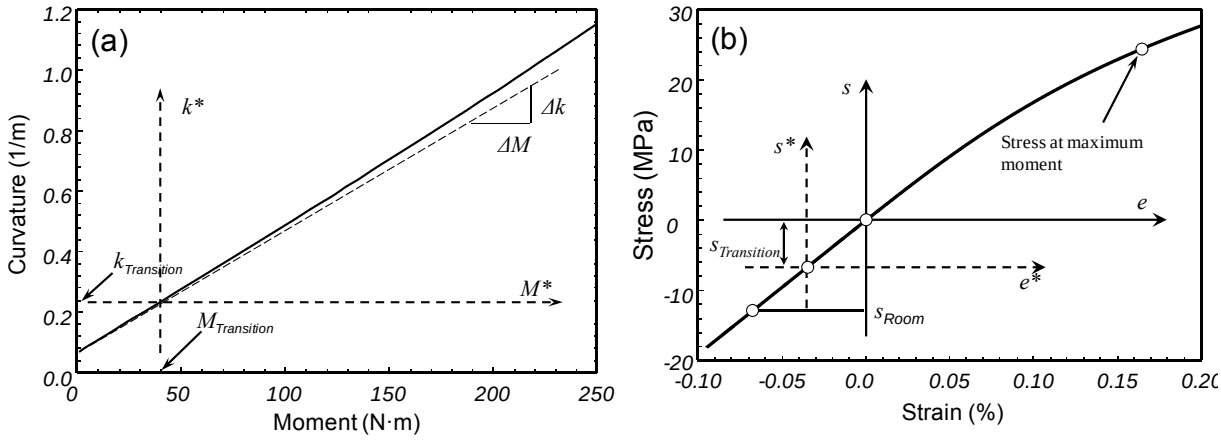

Figure 8.1: Extraction of non linear properties of coatings from 4PB test; (a) a typical curvature-moment plot obtained from test. The careful selection procedure of transition moment is depicted in the figure. (b) stress-strain curve obtained from the processing of moment-curvature plot shown in (a)[57].

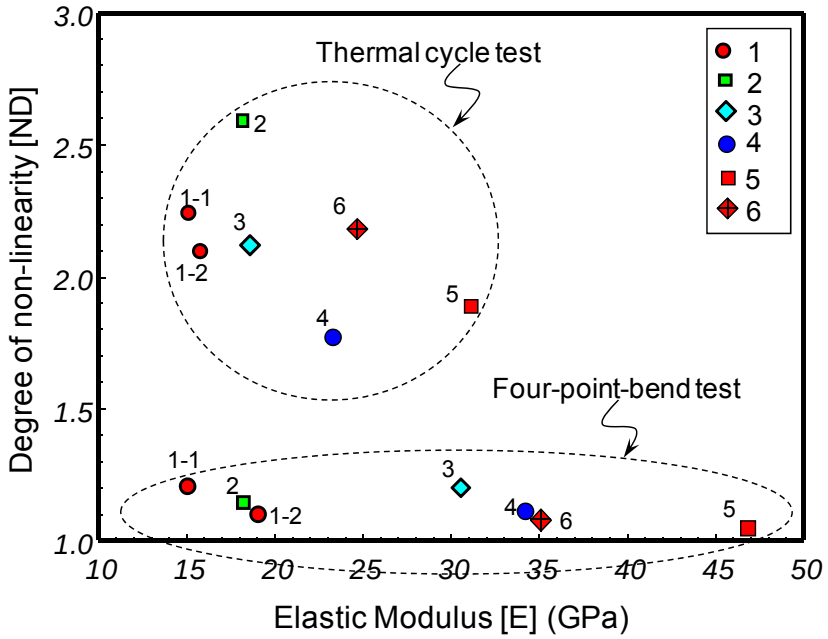

Figure 8.2: The E vs ND map for comparative study between the non-linear properties obtained from BCT thermal cycle as well as 4PB test. The E values from 4PB data are more scattered than those from thermal cycling data, which can be attributed to a higher sensitivity to errors in 4PB test as well as temperature change involved in the BCT thermal cycle test[57].

As preliminary experiments, a few selected specimens were used for 4PB test after having them thermally cycled on BCT measurement sensor. The non-linear elastic properties (E and ND) were determined for both the cases of thermal and mechanical loading and coatings were mapped on the E vs ND plot (Figure 8.2). The key observations from the Figure 8.2 so obtained are

- The non-linear elastic properties extracted from the mechanical loading data and from the BCT thermal cycle data are different, and the same batch of coatings can belong to two different regimes on E vs ND plot. This difference can be confirmed by comparing the two stress-strain behaviors of a single specimen under two different types of loadings (Figure 8.3).
- The elastic modulus (E) was similar under both mechanical as well as thermal loading (Figure 8.2). This indicates that in compression when the cracks and other defects embedded in the coatings are closed, the properties of YSZ coatings do not get affected by introduction of temperature. Additionally, transition stresses for both the loadings are noticeably similar, which implies that the coating requires same stress to activate the non-linear phenomenon.

- Figure 8.3 also displays that overall a single coating behaves stiffer under pure mechanical loading than thermal loading, which can be attributed to the increasing temperature in the case of a thermal test. The differences between the non-linear responses also support the fact that the mechanical properties of YSZ coatings are temperature dependent. Additionally, the thermal expansion coefficient as well as stiffness of the substrate (in this case Al) also depend on temperature, which contributes to the higher non-linearity associated with thermal loading of the coated specimen.

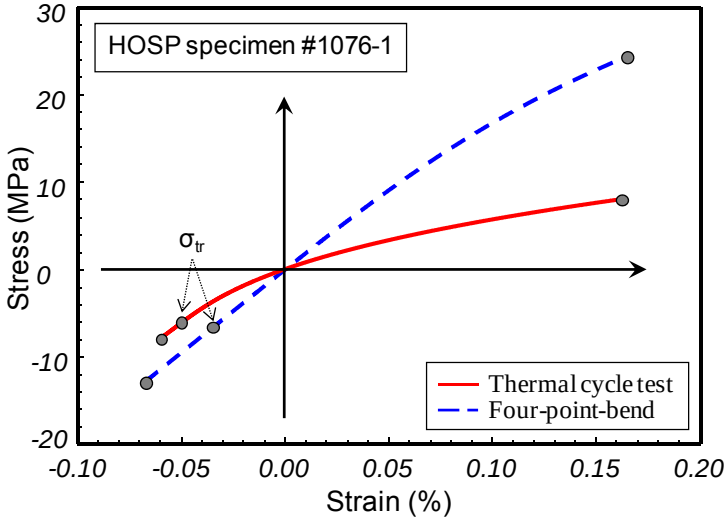

Figure 8.3: Stress strain curve estimated for curvature-temperature data from BCT thermal cycle test and curvature-temperature data from 4PB test for a single specimen. The coating suffering from mechanical load shows less non-linearity[57].

8.2. Examination of error sensitivity of elastic modulus on the input parameters to the model

For a better comparison of properties, analyses of the sensitivity of errors to the input parameters were carried out for both thermal cycle as well 4PB tests. For the purpose of illustration, only elastic modulus sensitivity calculations with incorrect as well as correct input parameters are tabulated in Table 8.1. The elastic modulus estimation from both the loadings exhibit the same degree of error (~1%) due to erroneous measurement of coating thickness (~1%). However, for both the cases, a 1% error in substrate elastic modulus magnifies to ~4.4% in coating elastic modulus estimation. On the other hand, 1% error in substrate thickness measurement can induce

errors up to 2.4% and 14.7% in non-linear properties extraction from thermal cycle and 4PB data respectively. Additionally, the error (1%) in elastic modulus raw data obtained from the test may introduce higher error values in the case of mechanical loading (~5.5) than that in the case of thermal loading.

(a)			(b)		
Parameters		**Value (Error)**	**Parameters**		**Value (Error)**
t	No error	30	T	No error	30
	+1%	29.6 (1.1%)		+1%	29.6 (1.3%)
	–1%	30.4 (1.3%)		–1%	30.4 (1.3%)
h	No error	30	H	No error	30
	+1%	30.7 (2.4%)		+1%	25.6 (14.7%)
	–1%	29.2 (2.4%)		–1%	34.6 (15.2%)
Es	No error	30	Es	No error	30
	+1%	28.7 (4.4%)		+1%	28.7 (4.4%)
	–1%	31.3 (4.4%)		–1%	31.3 (4.4%)
$\Delta\kappa/\Delta T$	No error	30	$\Delta\kappa/\Delta M$	No error	30
	+1%	30.3 (1.3%)		+1%	28.4 (5.3%)
	–1%	29.6 (1.3%)		–1%	31.6 (5.5%)

Table 8.1: Error analysis of elastic modulus calculations from (a) 4PB test and (b) thermal cycle test.

Table 8.1: Error analysis for (a) thermal test; (b) 4PB test in calculation of initial modulus induced from the errors in different input parameters[57].

Overall, it can easily be concluded that 4 point bending test is more prone to magnify the errors, introduced by the input parameters, than thermal cycle test, which is thus more reliable for extraction of true non-linear elastic properties. However, there are certain pros and issues for both the tests as listed below[57].

4PB test	BCT Thermal Cycle Test
Pros: ➢ Experimental time is short ➢ Pure mechanical loading (pure bend) ➢ Higher stress ➢ No temperature dependent CTE input ➢ Can be carried out at different temperature condition	**Pros:** ➢ Whole beam is in consistent stress-strain status (less boundary affection) ➢ Less measurement errors ➢ Analysis is less sensitive to errors
Issues: ➢ More measurement errors (loading indenter, etc.) ➢ Analysis is more sensitive to the errors ➢ Material's behavior similar under 4PB test	**Issues:** ➢ Long time to complete the process ➢ Difficult to keep the whole specimen at the same temperature ➢ CTE affection ➢ Smaller stress provided

The above preliminary results on 4PB show a good agreement with the non-linear behavior observed in thermal loading of coatings, although several other 4PB tests still need to be conducted in order to correlate the two different sets of non-linear properties more accurately.

9. Plasma sprayed ceramics and nacre like materials: similarities in mechanical response

Nacreous structure exhibits a brick-mortar like stacking assemblage of ceramic platelets (aragonite ($CaCO_3$) and thin polymeric layer serving as a mortar material to the structure. Figure 9.1 (a, b) show polished and Figure 9.1 (c) shows the fractured cross section of a nacre layer present in an abalone shell displaying a brick-mortar configuration of the structure. These naturally layered structures exhibit extraordinary mechanical properties, such as high strength and toughness[70]. A nacreous structure is 3000 times tougher than its major constituent, the aragonite ($CaCO_3$). Apart from the high strength and toughness, nacreous material also exhibit anelastic response under mechanical loading akin to that observe in plasma sprayed ceramics materials. Figure 9.2 compares the load-deflection response of a free-standing plasma sprayed YSZ coating and nacre, under three-point-bend and uniaxial tensile loading conditions reported by Currey. An interesting observation can be made from the Figure 9.2. Given that the brittle nature of YSZ ceramic, the coating does not display a brittle fracture and it shows a graceful failure onset of fracture. This can be attributed to the intrinsic strain or damage tolerance of the sprayed coatings arising from the layer by layer fracture at splat level. Although, the mode of loading is different in the two cases, the similarity between the two curves is noteworthy.

Figure 9.3 illustrates that under mechanical loading both the structures experience layer movements. It is interesting to observe that the anelastic response of plasma sprayed coatings is purely an intrinsic characteristic of the material; on the other hand the polymeric phase present in nacre is required for its anelastic response. Also it has been established that in the case of nacre, anelasticity is primarily introduced by polymer stretching, while in a sprayed ceramic the opening/closure and sliding of microstructural defects are the two main causes responsible for its anelastic behavior.

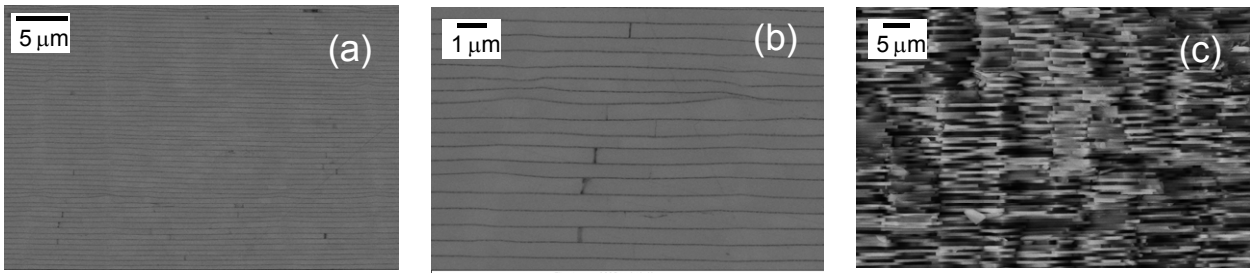

Figure 9.1: (a, b) are the polished cross section of a nacre from abalone shell at two different magnifications. (c) is the SEM image of a fractured cross section of the same nacre. All the three images display a brick-mortar assembly in the nacreous structure.

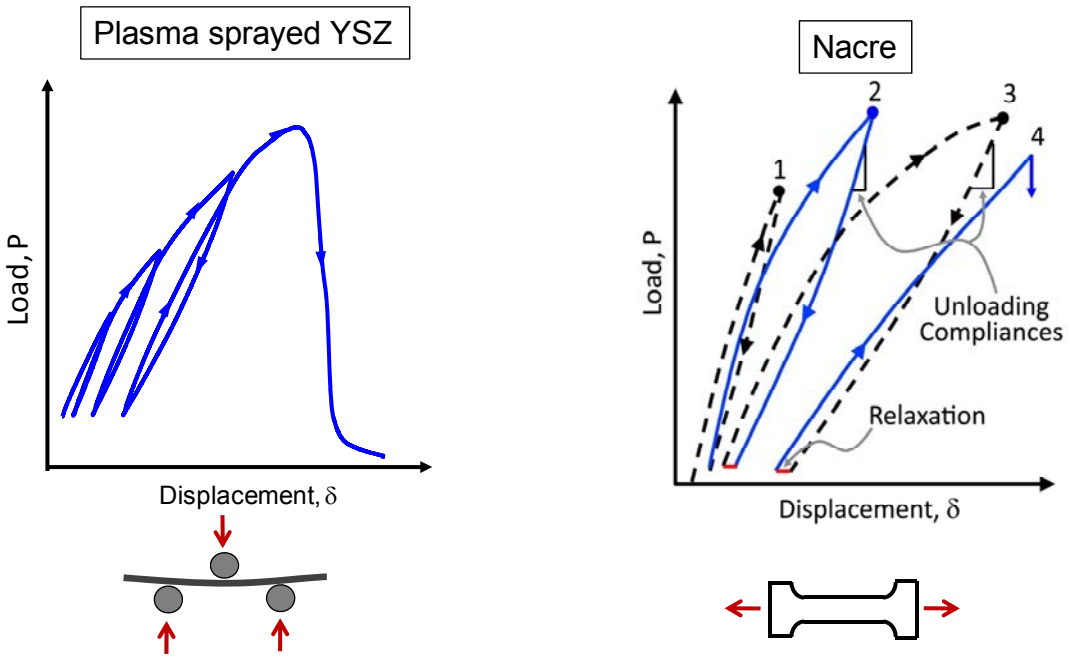

Figure 9.2: The load displacement curves of (a) a plasma sprayed YSZ coating under three-point bending and (b) a nacre under uniaxial tensile loading condition[14]. Given that the modes of loadings were different, the mechanical responses of the two structures are noticeably comparable.

The microstructural comparison of nacre and sprayed coating provides insights regarding the structural similarities between the two materials. Both the materials display architectural features ranging over an extended length scale. The intersplat boundaries in a coating resemble the platelet interfaces in a nacreous structure (Figure 9.4 (a)). Under mechanical loading, the interfacial sliding against the faces causes the energy dissipation contributing to the hysteretic response of the two materials. From a

higher magnification image of a nacre platelet one can observe that platelet surface displays a significant surface roughness of the order of nanometer (Figure 9.4 (b)). A similar kind of surface roughness (from nanometer to sub microns range) is observed on a splat surface generated due to the columnar grain termination. Earlier in chapter 7 we observed that the roughness associated with splat surfaces causes the hysteretic response of the coatings attributed to the energy dissipation on frictional sliding between the rough defect surfaces. Therefore, in the case of nacre a part of hysteresis can be attributed to these surface angulations. Moreover, there are asperities and bridges present between two nacre platelets which can contribute to the overall strength by locking mechanism of these features (Figure 9.4 (c)). Similarly, in the case of plasma sprayed coatings a splat can be restricted from movement by randomly oriented neighboring splats. The above details regarding microstructural similarities of the two classes of materials suggest that the mechanisms controlling the anelastic behavior of the coatings are remarkably similar so much so that with a better control on coating microstructure and selection of an appropriate polymeric phase, an attempt can be made towards mimicking the natural materials.

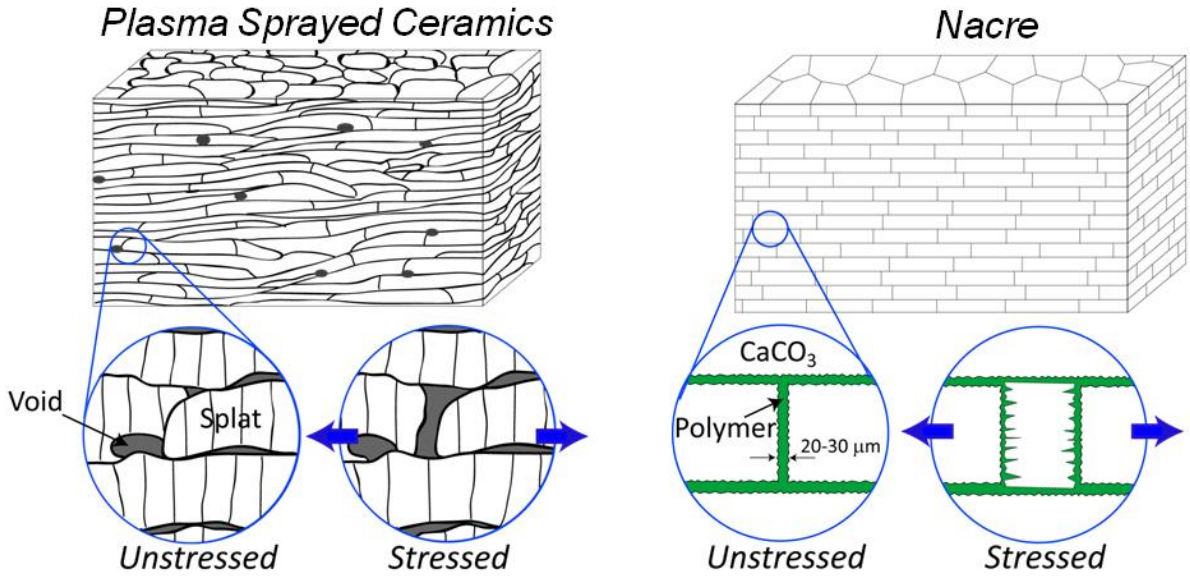

Figure 9.3: Schematic comparison of microstructure of plasma sprayed ceramics and nacre. Under loading condition, both the layered structures undergo movements between the layers(splats or platelets). *(Diagram courtsey: Prof. Christopher Weyant, Stony Brook University.)*

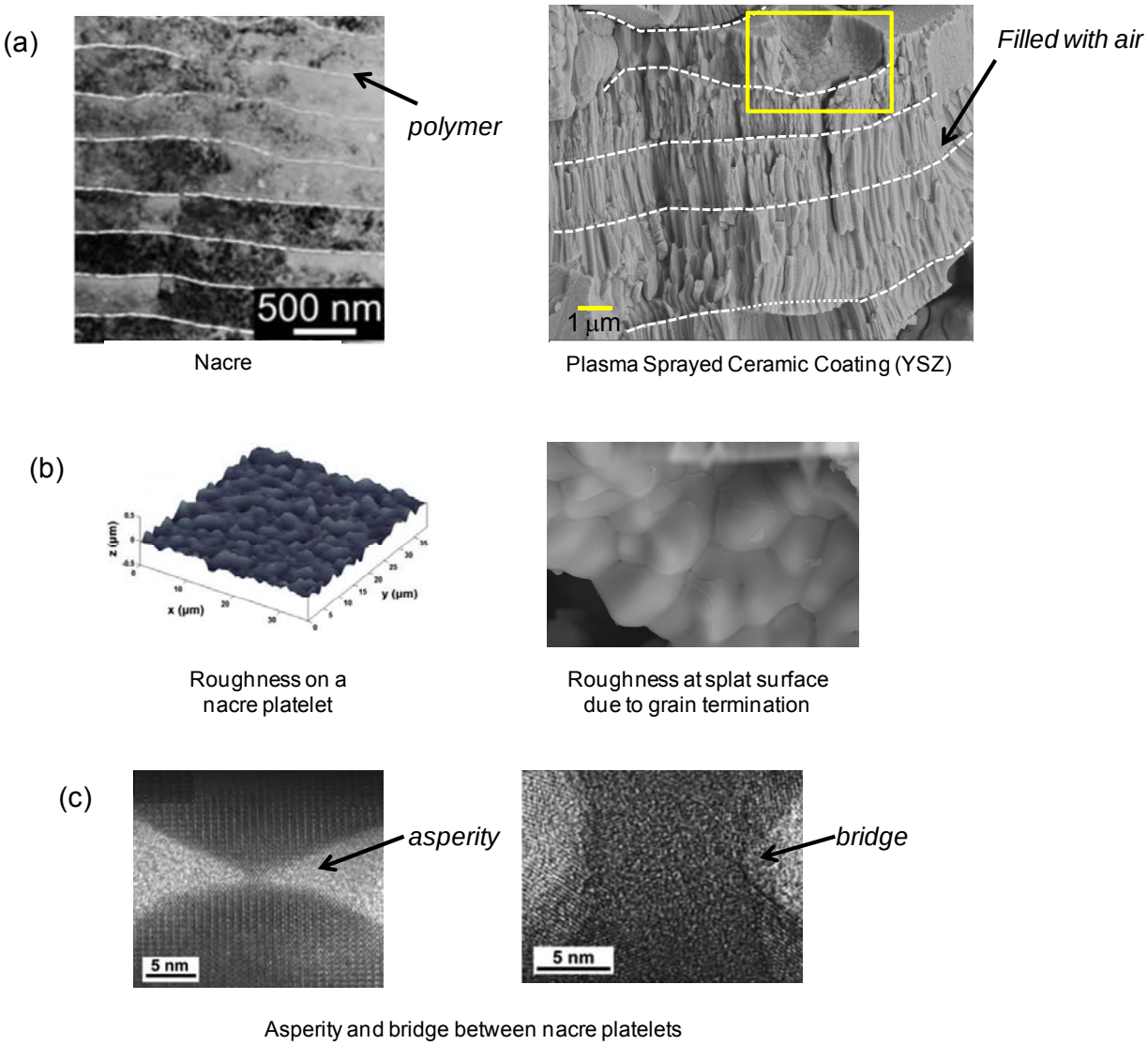

Figure 9.4: (a) comparison between the layered structure of nacre and plasma sprayed YSZ coating. Both the structures show waviness in their constitutive layers. (b) the roughness associated with nacre platelets and splat surfaces. (c) exhibits presence of asperity and bridge between nacre platelets. These features contribute to the toughening and strength of the nacreous structure[71].

As mentioned earlier, unlike nacre, the sprayed ceramic does not contain any polymeric layer between the splats. In addition to the intrinsic nacre-like mechanical response, given the porous architecture of sprayed ceramics, it is also feasible to introduce some polymeric media with higher toughness to enhance the overall anelasticity of the material. To investigate the effect of presence of polymer at defects sites of coatings, two 0.7 mm thick free standing PS YSZ coatings (width ~ 12 mm and length = 40 mm) were prepared. One of the two coatings was immersed in 1wt% PMMA solution in Toluene. The coating was taken out of the solution after 24 hours and kept in

the furnace at 60°C to evaporate the toluene from the coating. The three-point-bend test was performed on the as sprayed and infiltrated coatings at constant cross-head movement rate of 0.1 mm/min and a preload of 1 N was applied to have good contacts between coating and pins used for three-point-bend setup. At the end of each cycle the coating was taken out of the mounting stage (support span 35 mm) and placed back for next loading with higher maximum load for that cycle. This strategy was practiced for multiple cycles until the coatings failed. The load and displacement measurements were plotted.

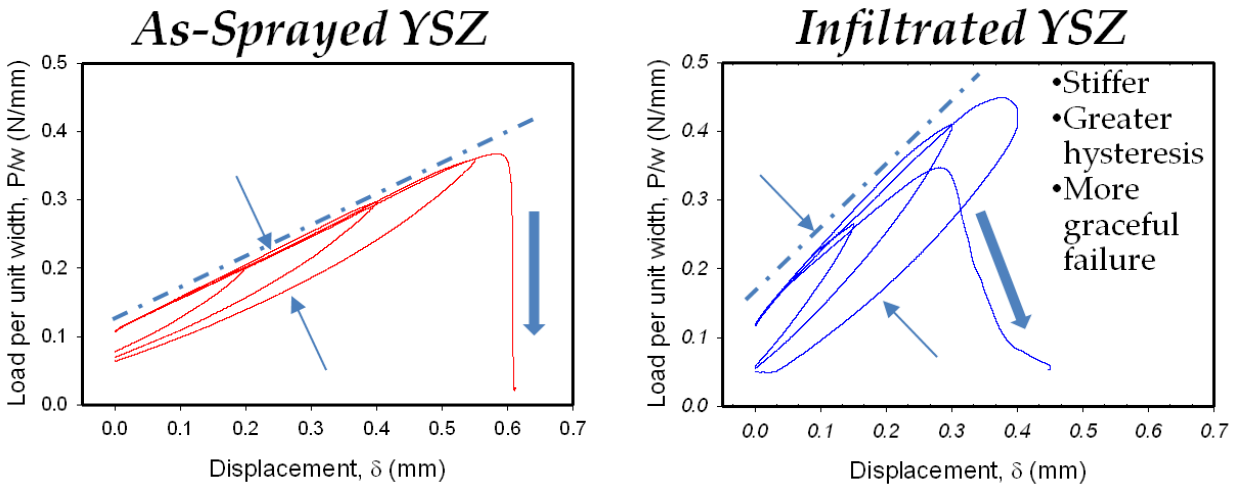

Figure 9.5: The load displacement curves of an as-sprayed and a PMMA infiltrated plasma sprayed YSZ coatings under three-point-bend loading. The infiltrated coating displays higher strength and hysteretic behavior as compared to as-sprayed one. It also exhibits more graceful failure mode than the as-sprayed coating.

Figure 9.5 shows the load-displacements plots of the two coatings. The y axis represents the load normalized with the width of the coating. One can easily observe that the presence of polymer not only provides stiffening to the coating, but also enhances its hysteretic response. The stiffer response can be attributed to the filling of pores or open defects with polymer, and the reason behind enhanced hysteresis can be the toughness introduced by the stretching of polymer. Lastly the different failure response of the coatings could probably be due to the bonding of polymer with the defects, which would have suppressed the crack propagation rate due to high toughness of polymer. Unfortunately, the limited amount of polymer in coating could not be observed under SEM, therefore there are no evidences of polymer presence between the defect surfaces for this particular set of coatings. However, later a modified

approach such as pressurized infiltration with higher wt% of PMMA in toluene was used to increase the polymer content in the coating. Figure 9.6 provides the fractographs of PS YSZ coatings with higher polymer content fractured under three-point-bend loading conditions. From the figure, it can be noted that it is feasible to introduce the polymeric media in porous plasma sprayed coating. The figure also displays the tearing and stretching of polymer during fracture of the infiltrated composite.

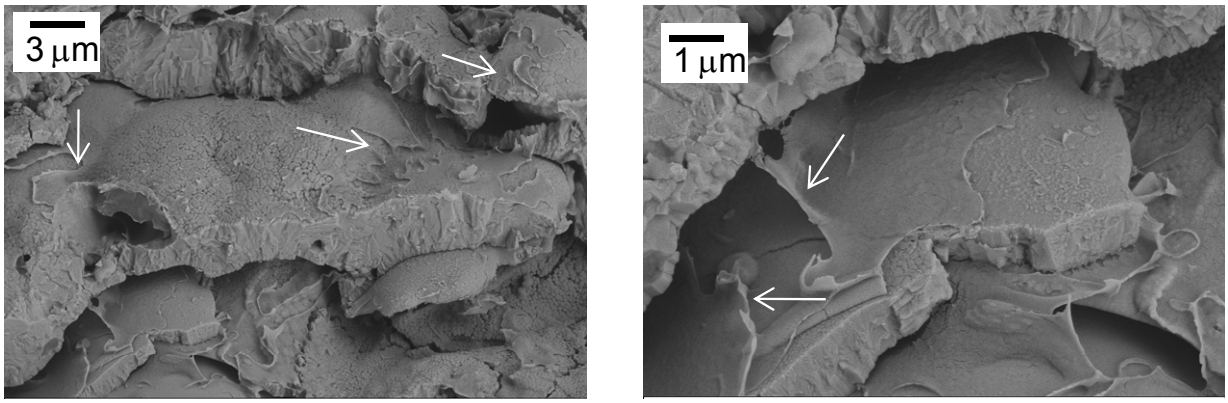

Figure 9.6: A fractured cross section of infiltrated YSZ specimen at two different magnifications. Bridging and tearing of the polymer attributes to enhanced mechanical properties of the coating.

These preliminary results indicate that free-standing plasma sprayed ceramic coatings exhibit anelastic response similar to nacreous materials under pure mechanical loadings. The anelasticity as well as the fracture properties of the coatings can be enhanced by introducing a tougher foreign media such as polymer. These results provide a platform for further research on the composite coatings to mimic natural materials. There are many attempts reported by researchers in the past towards synthesis of bio-inspired material, however they all are confined to relatively smaller length scale. The plasma spray deposition process provides not only the flexibility on choice of material but also large scale fabrication of porous ceramic templates which is valuable for certain applications. Furthermore, with the knowledge of controlled introduction of anelasticity by tuning the processing conditions it is feasible to fabricate tailored organic inorganic nacre-like composites. Such activities are currently being pursued.

10. Summary and Conclusions

The research presented in this dissertation is aimed at the understanding and application of novel anelastic mechanical behavior of plasma sprayed ceramics from a perpespective of processing and performance. Following the initial theoretical work by Liu et al, various improvements were made to the bi-layer curvature measurement technique to establish a robust methodology to observe and quantify anelasticity in coatings. These advancements with property measurement techniques enabled the application of anelasticity as a measure of both coating character and quantification of process repeatability. Moreover, based on the understanding from the analytical results of single crack model by Liu et al, experiments were designed to control anelasticity by modifying the coatings' defect architecture and physical properties.

The study conducted on the sensitivity in the measurement of the quantified anelastic parameters E, ND and HD, indicate that it is feasible to provide characteristic representation of the microstructure-property relationship. The parameters displayed high sensitivity to coating architecture which can be utilized to discern even small differences between processing conditions. For instance, the experiments on the YSZ coatings sprayed using two different powder morphologies, HOSP and FC, suggested that the FC coating exhibited a higher modulus and relatively lower anelasticity associated with a lower defect density seen in FC coatings. Furthermore, the results indicated that the anelasticity in a coating is more susceptible to powder feed rate rather than powder size distribution. HOSP coating sprayed with higher feed rate exhibited higher degree of anelasticity than the one deposited with lower feed rate. On the other hand, the anelastic properties of FC coatings deposited with two different powder cuts were comparable.

Application of anelastic parameters to assess the process and coating repeatability during multiple deposition periods and spray configuration was also conducted. The experimental design consisted of coatings preparation over 5 consecutive days with start-stop of plasma torch on ICP sensor as well as on a carousel during a single spray run. Multiple coatings sprayed in a single run on a carousel exhibited higher repeatability than those sprayed over a course of five days. This observation supported the influence of day-to-day ambient conditions on the intrinsic variability of the plasma

spray process. The repeatability was significantly improved with a narrow powder size distribution than a wider one, during a single run.

The understanding of the anelasticity in plasma sprayed ceramics based on the single crack model developed by Liu et al, suggested that the anelastic parameters can be controlled up to a certain extent by altering the defect characteristics of coatings. With the knowledge of process sciences, one can control the architectural properties of defects. Furthermore, the surface properties of defects in coatings can be altered by changing the feedstock materials. The experimental study on controlling the anelasticity of YSZ coatings suggested that the anelastic parameters of these coatings can be modified by tuning their process conditions. YSZ coatings sprayed at different spray distances showed different non-linear and hysteresis response. Spray condition with 150 mm spray distance resulted in a coating with higher ND and HD than the condition with 60 mm followed by 100 mm spray distances. Moreover, plasma energy as well as deposition pattern showed significant influence on the coatings anelasticity. Coating sprayed with high plasma condition exhibited stiffer response than that sprayed with lower energy condition. However, the hysteresis on coatings reduced with increase in plasma energies. Furthermore, the coatings sprayed on carousel and ICP sensor displayed significantly different anelastic response. Coating deposition on the ICP sensor revealed that coating sprayed with along-the-width was less non-linear and stiffer than that sprayed with along-the-length deposition pattern.

The experimental study on the role of interface roughness on anelasticity indicated that this may be a key contributor to the frictional hysteresis. It was established from the single crack model by Liu et al that the hysteresis in mechanical response of the crack depends on the friction between the sliding faces. Microstructural observations of YSZ revealed a surface roughness ranging from sub-micron to nanometer length scale leading to the columnar grains termination at the splat surface. In contrast, amorphous splats produced by plasma sprayed ceramics such as mullite, cordierite and forsterite exhibited smooth splat surfaces which in turn resulted in a limited hysteretic response of the coatings. The hysteretic response was relatively higher in the case of forsterite coating as compared to other amorphous coatings which can be a result of the higher crystallinity confirmed by its x-ray diffraction data. Interestingly, all the sprayed amorphous coatings exhibited non-linearity which can be ascribed to the defect architecture of the coatings.

An attempt to conduct extrinsic modification of coatings defect surfaces was carried out by introducing salt in to a coating by immersing it in a salt solution for a sufficient period. Coatings with salt residue exhibited stiffer as well as higher anelastic responses depending on the interfacial roughness of the coatings. An untreated amorphous

coating, mullite or cordierite, remains unaffected by the salt introduction, while the forsterite coating with limited or a YSZ coating with high crystallinity appeared to be highly influenced by the presence of salt residue at sliding interfaces. An alternative way to introduce the salt in a coating was explored by spraying the salt solution along with the coating deposition. The result suggested that the change in anelasticity was more prominent in this case than with a salt solution immersed coating.

Coatings subjected to pure mechanical loading (4PB) confirmed presence of anelasticity although the degree of the anelasticity was lower. The elastic modulus of a coating was comparable in magnitude for both the loadings, although the non-linear degree was significantly lower with pure mechanical loading. Additionally, the error analysis conducted on two different types of loadings suggested that the extraction of non-linear parameters from 4PB data was more prone to magnifying the errors in input parameters than thermo-mechanical loading data.

Lastly, preliminary investigation conducted on microstructural as well as mechanical response similarities between nacre and plasma sprayed ceramics revealed that both the structures exhibit not only remarkably similar brick-wall arrangement but also display anelastic behavior under mechanical loading conditions provided that the nacre contains polymeric phase up to 5vol%. Moreover, owing to the porous microstructure of coatings, an attempt was made to infiltrate polymer into a YSZ coating. The coating not only showed an enhanced anelastic response as compared to an un-filtrated one, but also exhibited a graceful fracture contrary to the brittle failure of ceramics.

Understanding the three anelastic parameters

The three anelastic parameters, E , ND and HD are unique for a given coatings. The low temperature elastic modulus, E is the slope of stress-strain curve in the linear elastic region of a coating. The magnitude of E depends on overall defect density and quality of welding/bonding of splats. A coating with high defect density will have lower elastic modulus than a denser coating. On the other hand a good splat-splat welding/bonding will provide a higher overall stiffness to coating structure. Furthermore, the frictional characteristics of defect interfaces may influence the E value of coating. The surfaces with higher coefficient of friction will require higher stresses/strain to initiate relative movement between the two defect surfaces in contact, which can make a coating perform stiffer.

The degree of non-linearity is a parameter which represents the relative non-linearity with respect to its E value. Higher the value of ND will represent a coating which undergoes greater non-linearity for a given E. It is important to realize that to

achieve a certain stress at a given strain, especially in the non-linear regime, various combinations of E and ND can be chosen. For example, for a given strain (ε_o), the stress (σ) will be calculated as following

$$\sigma = E_{\text{sec}} \times \varepsilon_o$$
$$\sigma = \left(E \diagup ND\right) \times \varepsilon_o \qquad \text{Eq. (10.1)}$$

From equation 10.1, it is clear that the absolute value of σ depends on the two anelastic parameters and which can be achieved by several combinations of E and ND parameters. This reveals an interesting fact about coatings' mechanical properties, which is that it is possible that the coatings with different E and ND parameters can experience similar stress at a given strain. However, the coatings can be significantly or slightly different among each other and these differences can be captured by the two parameters.

The physical significance of the ND parameter is related with the density of different types of defects in coatings. Beyond the transition point, with increasing strain a class of defects, such as globular pores and interlamellar pores, will start increasing their opening dimensions. This will result in softening of coating architecture affecting both E and ND parameters of the coating. On the other hand, another class of defects which includes microcrack and columnar grain boundaries will experience sliding, which will influence the ND and HD parameter. Therefore, the magnitude of ND will represent the degree of movable defects which govern compliance in a coating. In short, for a given E, a higher value of ND will correspond to a more compliant coating.

The third parameter, HD depends on density of the defects which undergo sliding mechanism with increasing strain. For a given material, higher density of these defects will result in higher value of HD. It is important to realize that the HD is defined as the ratio of hysteresis loop area (A_H) and the product of total stress and strain change ($\Delta\sigma$ x $\Delta\varepsilon$). This means that two coatings with same hysteresis loop area may not have same HD.

The frictional characteristics of the sliding interfaces have a great influence on the HD parameter of a coating. Defect surfaces with higher coefficient of friction dissipate more energy during sliding than those with relatively smoother surfaces, resulting into higher hysteresis loop area. Additionally, the HD will depend on the mobility of the surfaces. An immobile interface will not be able to contribute to the hysteresis. Therefore, both frictional properties and mobility of the interfaces decide the magnitude of HD.

In conclusion, it can be established that, up to a certain extent, the three anelastic parameters are able to provide an estimate regarding the density of different types of defects in a coating. Figure 10.1 illustrates the influence of defects on the three anelastic parameters. Although, at this stage, it is not possible to decouple the contribution of each defect type on the individual anelastic parameter, yet the estimation of the defect types will help in understanding their effect on other mechanical properties of coatings.

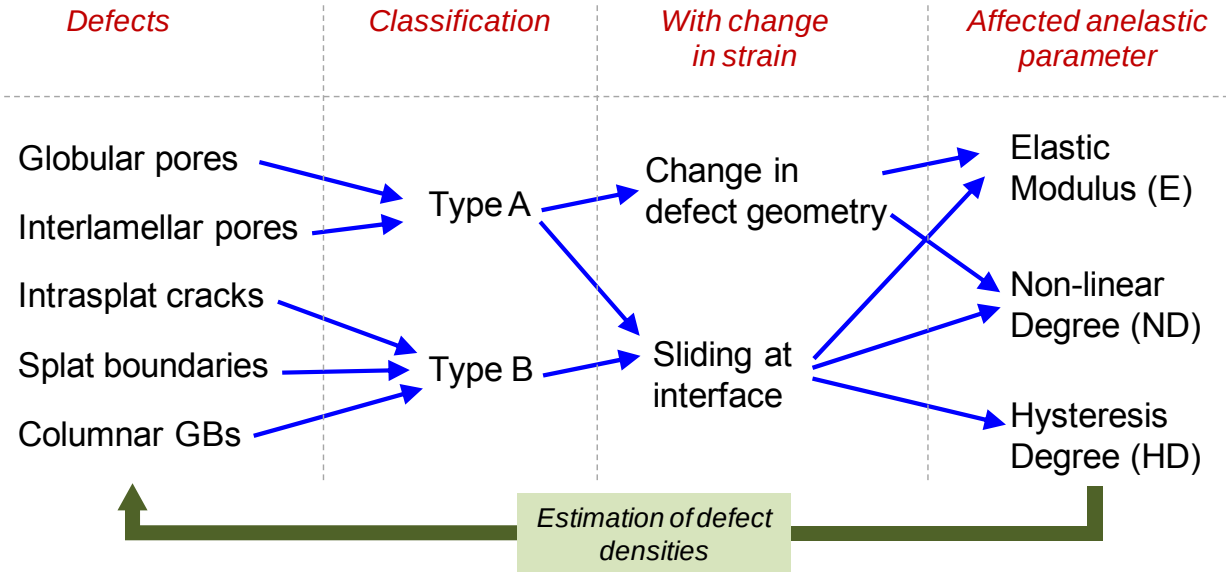

Figure 10.1: Effect of different types of defects in a coating on the three anelastic parameters.

11. Suggestions for future work

The principle focus of this dissertation is the understanding and control of the anelastic behavior of plasma sprayed ceramics. However, there exist many other aspects, both on understanding as well as applications of this novel phenomenon, which will benefit from further exploration. The knowledge gained in this work not only provides a platform for continuing research on plasma sprayed ceramics, but also direct us to investigate anelasticity in other materials-processing systems. The following suggestions for future work propose some areas of interests, which will broaden our understanding and capability to utilize the intrinsic anelastic behavior of the thermal spray structures in multiple dimensions.

11.1. Anelasticity and mechanical damping in plasma sprayed YSZ coatings

A significant amount of research has been conducted in the past on plasma sprayed coatings for their high damping capacity [72-74]. The TBCs applied to the gas turbine engine parts help the metal withstand vibratory load generated due to very high revolutions of the turbine rotors. The wakes created by gases flowing through stator vanes and struts can also impart significant vibration when a turbine blade passes through it. This vibration can cause serious cyclic fatigue damage to a part when the system operates with an excitation frequency from the vibration that matches with the natural resonance frequency of the part[75].

The source of mechanical damping phenomenon is expected to be energy loss in a real solid. On the other hand the hysteresis present in the anelastic behavior of plasma sprayed coating indicates that the energy dissipation is due to frictional sliding at the crack surfaces. Though, the modes of loading for vibrational and quasi-static loadings are different, hysteresis in anelastic behavior as well as the dampening associated with plasma sprayed coatings seem to follow a similar mechanism, which is frictional energy loss at crack sites.

Figure 11.1 shows the damping properties of three coatings sprayed with different plasma enthalpy, similar to coatings analyzed in section 6.2. The parameter tanδ represents the phase difference between the applied stress and its strain response under cyclic loadings. Detailed description on tanδ is beyond the scope of this section, however, it can be considered as a damping indicator. It is interesting to observe that the damping properties and the hysteresis exhibit some trend for these coatings. Both the measured properties decrease with denser coating architecture.

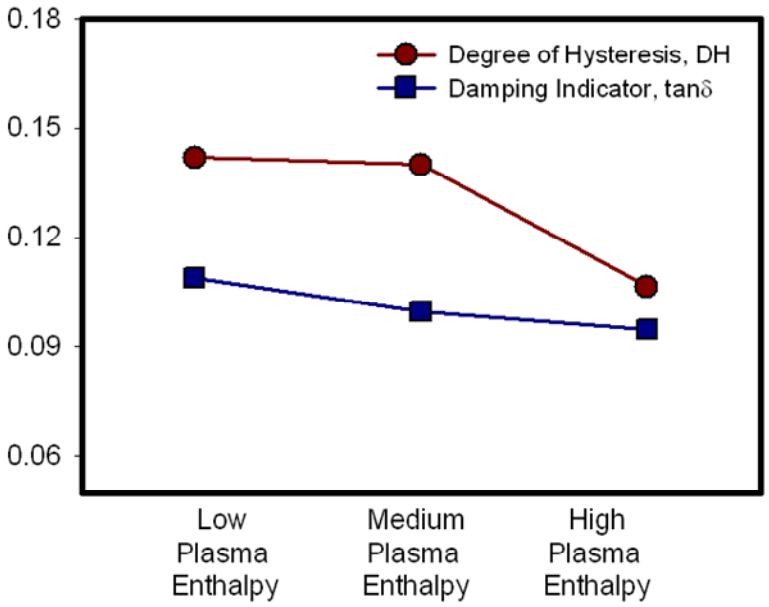

Figure 11.1: tanδ and degree of hysteresis (HD) of the coatings sprayed with three different plasma enthalpies.

These results are preliminary and yet to be repeated. Nevertheless, they do present a possibility to explore and establish a correlation, if any, between hysteresis and damping behavior of coatings.

11.2. TBC anelasticity and service life

The thermal barrier coatings (TBCs), one of the many important applications of plasma sprayed ceramics, are applied to the hot sections of a gas turbine engine to provide a thermal protection to the parts underneath at high temperatures. Due to the defect architecture, these coatings are known to possess low thermal conductivity on and high strain tolerance, which are the two key requirement of any TBC structure. A typical TBC is deposited on a superalloy with bondcoat at the interface (Figure 11.2).

Over a course of service period the top coat fails as it spalls from the part. This period is referred as the service life of the coating. Experimentally, the life of a TBC is predicted by exposing the three layer system, top coat (YSZ), bond coat and the super alloy substrate or a certain dimension, into an isothermal or a gradient temperature environment. The purpose of this test is to estimate the time period for which a coating can withstand the thermal loading before failure. Most of the failures occur due to oxide (also known as thermally grown oxide (TGO)) growth at the coating and bond-coat interface layer which builds up very high compressive stresses (order of 1 GPa)[76] due to thermal mismatch. Another reason for coating failure is sintering of the top coat, which occurs during the course of high temperature exposure of the coating. The sintered YSZ layer stiffens due to reduction in porosity and cracks, hence the reduced coating's mechanical compliance leads the coating to failure due to high mismatch stresses at operating temperatures[77]. There are several other mechanisms which contribute to the life of a coating ; however, they are not discussed in this section.

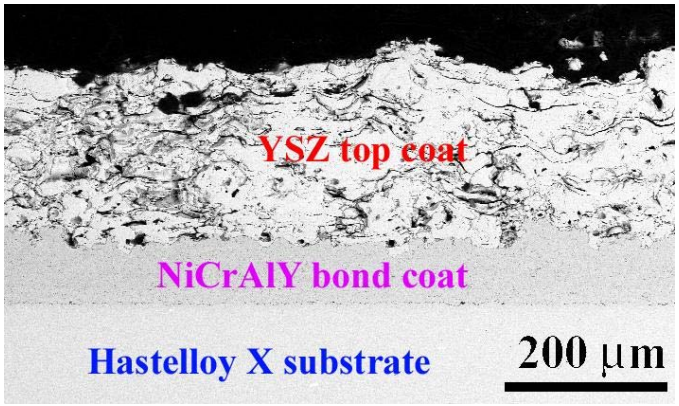

Figure 11.2: A typical plasma sprayed TBC system consists of a Hastelloy superalloy, NiCrAlY bondcoat and PS YSZ as the top coat.

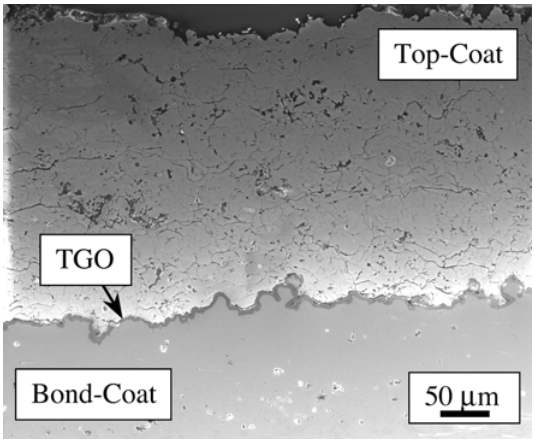

Figure 11.3. The growth of thermally grown oxide (TGO) in a TBC system. The TGO develops high compressive stresses (~ 1GPa) at the coating and bondcoat interface leading the topcoat to failure.[76, 77]

The anelasticity in a plasma sprayed TBC is an overall performance of the given defect architecture, which might have a correlation with the coating's life performance. For instance, the sintering of a topcoat would be governed by the separation between the two defect surfaces, such as crack opening dimension, intersplat spacing etc; and from our knowledge gained from previous sections of this dissertation; it is known that these geometrical attributes of the defects influence the anelasticity in the coating. Moreover, the oxygen transport through the topcoat causes oxidation of bondcoat leading to the growth of TGO. Several authors have stated that the topcoat is transparent to oxygen due to the porous and microcracked structure of a plasma sprayed coating [78, 79]. Also, it has also been established that the coatings sprayed with different feed rates, hence possessing different starting microstructure, exhibit different degree of oxygen permeability through them[79]. Therefore, it is clear that the defect density in a coating which governs the anelasticity also controls the oxygen transport to the bondcoat, and hence the TGO growth rate.

In short, it would not be surprising to correlate the coating life with its anelasticity. It is possible that the three anelastic parameters, E, ND and HD, have different contributions to the coating life and an empirical relationship can be established between these parameters as shown below.

$$\text{Coating life} = f(E, ND, HD)$$

11.3. Anelasticity in coatings sprayed with other thermal spray processes

HVOF sprayed Alumina coatings

Chapter 6 proposed some of the many ways to control or introduce anelasticity in plasma sprayed coatings. This novel characteristic of sprayed deposits can be observed in a coating sprayed with other thermal spray processes. Figure 11.4 shows the curvature-temperature response of three alumina coatings sprayed with high velocity oxy fuel (HVOF) process using HV-2000 torch, sprayed with three different torch raster speeds (330, 500 and 750 mm/sec). All other input parameters for deposition were kept constant. It is interesting to note that the higher raster speeds (500 and 1000 mm/sec) were unable to introduce any anelasticity in coatings. On the other hand, a slow raster speed (330 mm/sec) introduces some degree of anelasticity, which provides a higher particle flux per unit time and area of the substrate. It is highly possible that higher density of deposit might have introduced some local microcracking in the coating creating sites for relaxation of high deposition stresses. Later, subjected to the BCT measurements, those microcracks made the coating behave anelastically.

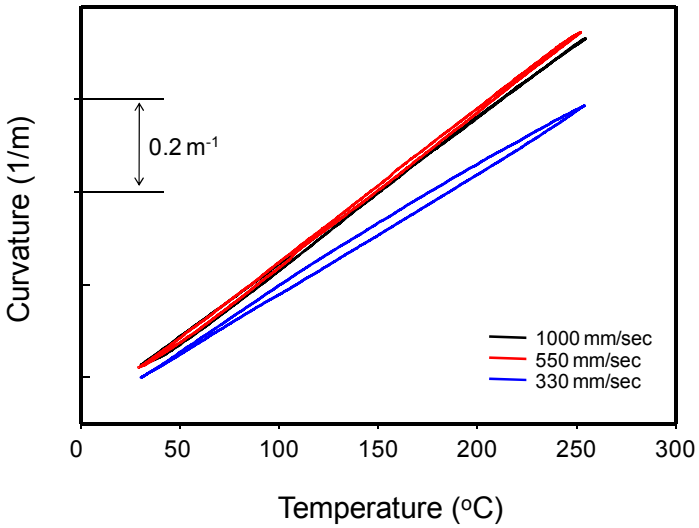

Figure 11.4: The curvature-temperature responses of three HVOF Alumina coatings sprayed with different raster speeds. The slowest raster speed introduces anelasticity in the coating.[76, 77]

The above observations provide a platform to explore more on the introduction of anelasticity in coatings sprayed with different thermal spray processes.

Plasma sprayed Mo coatings

In earlier sections, we observed that the sources of anelasticity in a ceramic coating are the physical structure and the surface properties of coating's defect architecture. This provides a motivation to explore this novel phenomenon in other materials or processing systems. For example, Figure 11.5 (a) shows the curvature-temperature data of a plasma sprayed Molybdenum (Mo-A) with the thickness of 150 μm coating on a ICP substrate (1.6 mm) obtained from the BCT measurements. The plot exhibits not only a non-linear response of the coating but also a significantly large degree of hysteresis. The curvature-temperature relationship was highly repeatable over multiple cycles similar to that observed in the case of the ceramic coatings. The degree of non-linearity (ND = 1.95) as well as hysteresis (HD =10%) exhibited by the curvature-temperature relationship was comparable to those of the plasma sprayed YSZ coatings. These observations are quite interesting as most of the metallic coatings sprayed with different thermal spray technique do not exhibit a non-linear response under mechanical loading.

Interestingly, a relatively thick (500 μm) plasma sprayed Mo coating (Mo-B) sprayed under similar conditions was only able to show a little non-linearity with some hysteresis under the BCT measurement (Figure 11.5 (b)). On the other hand, the results from the Mo coating (Mo-C) (360 μm) sprayed with flame spray technique (a combustion powder thermal spray process) showed almost linear response with very limited hysteresis (Figure 11.5 (c)).

From the above observations on Mo coatings, it can be concluded that mechanical anelasticity is not restricted only to ceramic coatings. A structure with appropriate defect architecture, density and with sufficient friction at the interfaces can exhibit anelasticity in the BCT measurement test.

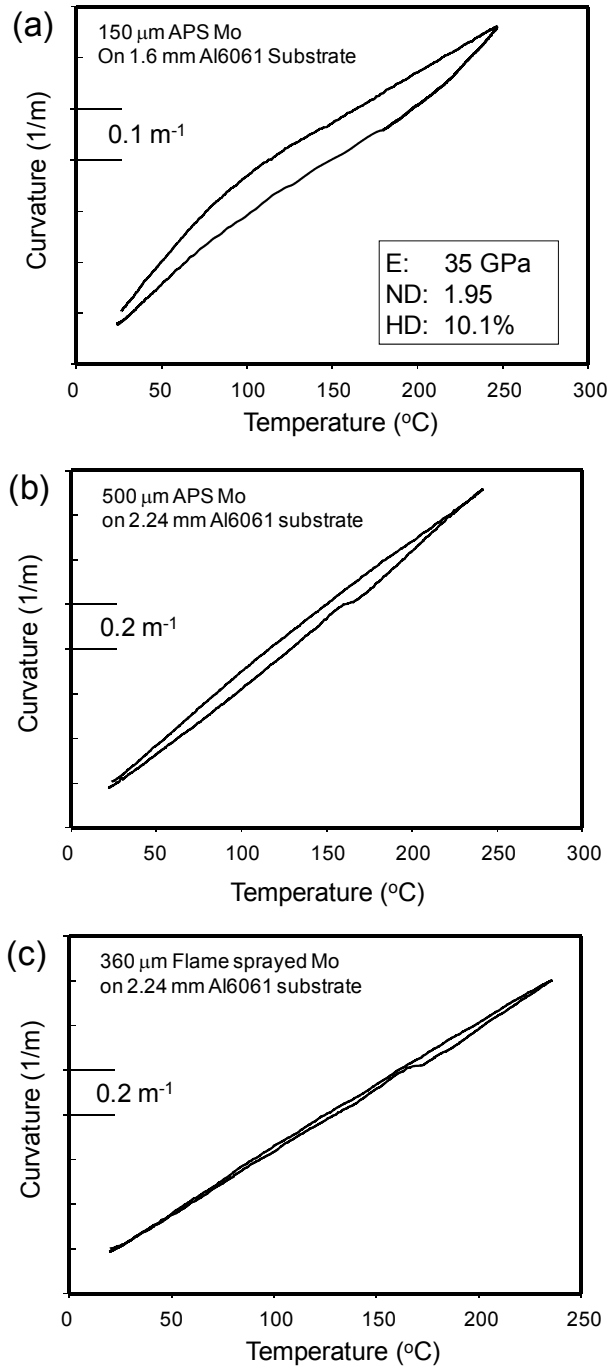

Figure 11.5: Curvature-temperature responses of the three Mo coatings. (a) thin coating and (b) thick coating sprayed by APS process. (c) thick coating sprayed by flame spray process.

11.4. Experimental approach to observe anelasticity under compressive thermal loading

So far, the BCT test of a coating of lower CTE on a higher CTE substrate material displays anelastic behavior of the coating under tensile loading. The coating after deposition, especially with the combination of YSZ coating and Al substrate, is, in general, in a state of compression. Therefore, when the coated specimen is heated, due to the sign of CTE mismatch, the coating goes to a tensile state through a zero stress state. On the other hand, the mechanisms identified for the anelastic behavior using a single crack models are for a crack under compression. Although, it is possible that some zones in a coating experiences some local compressive stress field for an external overall tensile stress. Therefore, it is also important to see the actual curvature temperature response of a coating under compressive loading. One way of achieving it is to bring the coated specimen to a temperatures lower than the room temperature, however, the current set-up of BCT measurement sensor does not offer such type of loading; nevertheless, another approach can be exercised to achieve such compressive loading, which is by selecting the substrate material, Mo, which has lower CTE (~6/^{o}C) than the YSZ coating (10/^{o}C).

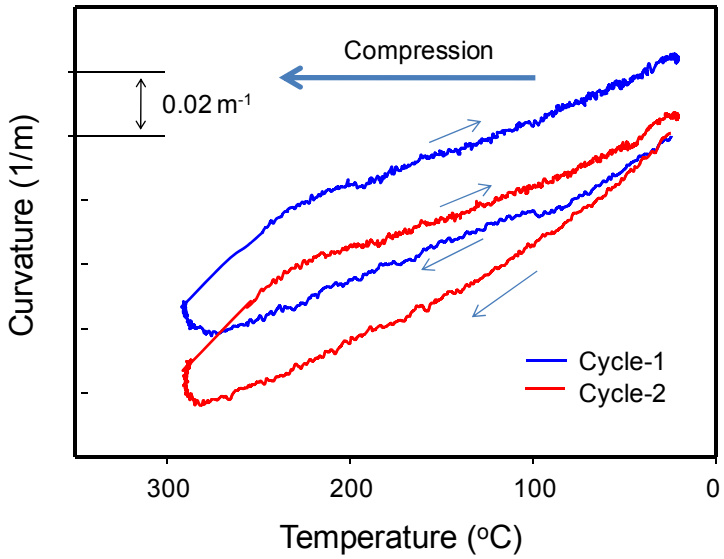

Figure 11.6: The anelastic curvature-temperature responses of YSZ coating on a Mo substrate. Due to lower CTE of substrate, the coating undergoes compression upon heating.

Figure 11.6 shows the curvature-temperature response of a 200 μm YSZ coating on a 900 μm Mo substrate. Clearly, as the temperature increases coating experiences more compressive stresses. The response is similar to that of YSZ- Al system in many ways. The coating showed both non-linearity and hysteresis. A detailed analysis on the response will provide some other insights, and hence will broaden our understanding of the coating anelasticity under externally applied compressive stresses.

11.5. Anelasticity and fracture toughness

The interplay of the defects present in a coating, which manifests as coating anelasticity, also suggests the possibility of these having an effect on other coating properties, such as fracture toughness etc. This section will present some of the preliminary results on the correlation between anelasticity and fracture toughness of a sprayed ceramic. There exists several ways to measure the fracture toughness of a material, such as tensile tests, three- and four-point bending tests, indentation tests, double cantilever beam tests, and double torsion tests to name a few[80]. The results discussed here were obtained from the double torsion test method adapted by Shyam et al[81].

To conduct the DT test, several coatings were sprayed with four different processing conditions. First three conditions used three different plasma enthalpies, Low, Medium and High at 100 mm spray distance similar to those in section 6.2. The fourth spray condition consisted of spraying with Medium plasma enthalpy but at longer (150 mm) spray distance (section 6.1). All the coatings were sprayed on to standard ICP beams, and then coupons of required dimensions were cut from the deposited beams. Later, the substrates were dissolved in acid (section 3.4) to prepare free-standing coatings for the fracture toughness test.

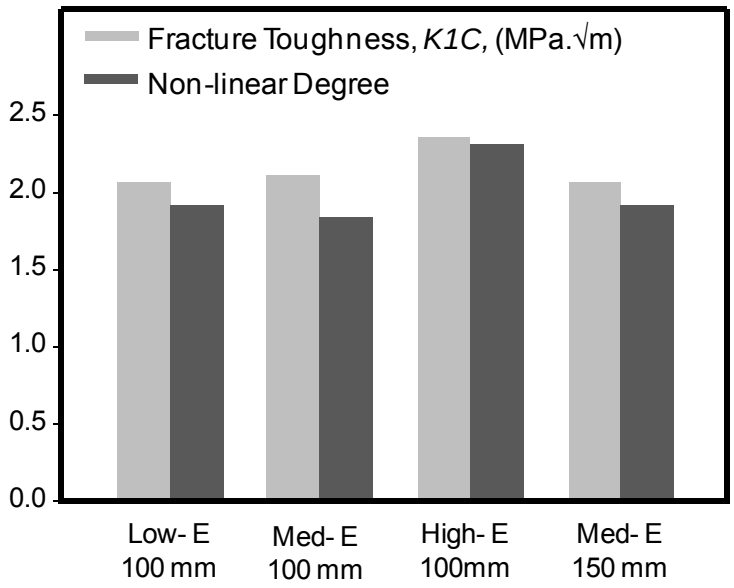

Figure 11.7: Comparison between the fracture toughness and nonlinearity of PS YSZ coatings.

The comparison of fracture toughness numbers with the non-linear degree (ND) of the coatings provides another interesting correlation between the two properties. Figure 11.7 shows the fracture toughness values averaged over the number of data points for each condition obtained from DT test. The figure also compares the ND values of the coatings sprayed with the four process conditions corresponding to those used for DT specimen preparations. At this stage, it is not possible to establish a clear relationship between the two coating properties, nevertheless the trend of the two measured properties are very similar. The difference between low-E and Med- E coatings in their fracture toughness and non-linear degree is not significant. Interestingly, both the properties are higher in value for the coating sprayed with High- E condition as compared to the other energy conditions. In section 6.2, it was mentioned that the coating sprayed with higher plasma energy consists of higher crack density, and hence it shows higher non-linearity. A similar argument can be applied to the higher fracture toughness value of the coatings sprayed with High energy condition. The higher micro-crack density provides an increased number of sites for crack deflection, which enhances the fracture toughness of the coating.

These preliminary results on the correlation between fracture toughness and non-linearity of the coatings needs to be repeated on more number of specimens as these properties are susceptible to the variability associated with local coatings microstructures. Nevertheless, the observations made here, such as increase in fracture toughness with polymer infiltrated coating and a correlation between coating's non-linear degree and fracture toughness, are noteworthy. A more careful design of

experiments can be planned to establish an empirical relation between ND and fracture toughness of the coatings.

Several other research dimensions can be proposed and explored on the anelasticity of sprayed coatings. For example, the anelasticity approach can be extended and applied to the Electron Beam Physical Vapor deposited coating used for turbine blades similar to plasma sprayed YSZ coatings.

References

1. C. Zener, Anelasticity of Metals, *Transactions of the American Institute of Mining and Metallurgical Engineers*, 1946, **167,** p. 155-191.

2. C. Zener, Elasticity and anelasticity of metals, 1 ed., The university of chicago press, 1948.

3. M. Helmut, Diffusion in solids: fundamentals, methods, materials, diffusion-controlled processes, Springer, 2007.

4. C. Zener, Internal friction in solids, *Proceedings of the Physical Society*, 1940, **52**, p. 152-166.

5. G.E. Dieter, Mechanical Metallurgy, *Mc-Graw Hill series in Materials Science and Engineering*, Mc-Graw Hill, 1988.

6. J.B. Walsh, Effect of Cracks in Rocks on Poissons Ratio, *Journal of Geophysical Research*, 1965, **70**(20), p. 5249.

7. J.B. Walsh, Effect of Cracks on Uniaxial Elastic Compression of Rocks, *Journal of Geophysical Research*, 1965, **70**(2), p. 399.

8. F. Barthelat, and H.D. Espinosa, An experimental investigation of deformation and fracture of nacre-mother of pearl, *Experimental Mechanics*, 2007, **47**(3), p. 311-324.

9. J.D. Currey, P. Zioupos, P. Davies, and A. Casinos, Mechanical properties of nacre and highly mineralized bone, *Proceedings of the Royal Society of London Series B-Biological Sciences*, 2001, **268**(1462), p. 107-111.

10. R. Menig, M.H. Meyers, M.A. Meyers, and K.S. Vecchio, Quasi-static and dynamic mechanical response of Strombus gigas (conch) shells, *Materials Science and Engineering a-Structural Materials Properties Microstructure and Processing*, 2001, **297**(1-2), p. 203-211.

11. F. Barthelat, Biomimetics for next generation materials, *Philosophical Transactions of the Royal Society a-Mathematical Physical and Engineering Sciences*, 2007, **365**(1861), p. 2907-2919.

12. J.D. Currey, and J.D. Taylor, Mechanical-Behavior of Some Molluscan Hard Tissues, *Journal of Zoology*, 1974, **173**(Jul), p. 395-406.

13. F. Barthelat, Nacre from mollusk shells: a model for high-performance structural materials, *Bioinspiration & Biomimetics*, 2010, **5**(3).

14. J.D. Currey, Mechanical-Properties of Mother of Pearl in Tension, *Proceedings of the Royal Society of London Series B-Biological Sciences*, 1977, **196**(1125), p. 443.

15. J.Y. Rho, L. Kuhn-Spearing, and P. Zioupos, Mechanical properties and the hierarchical structure of bone, *Medical Engineering & Physics*, 1998, **20**(2), p. 92-102.

16. H.N. Herkowitz, and G.R. Bell, The lumber spine, 3 ed., Lippincott Williams & Wilkins, 2004.

17. E.F. Rejda, D.F. Socie, and T. Itoh, Deformation behavior of plasma-sprayed thick thermal barrier coatings, *Surface & Coatings Technology*, 1999, **113**(3), p. 218-226.

18. S.R. Choi, D.M. Zhu, and R.A. Miller, Mechanical properties/database of plasma-sprayed ZrO2-8wt% Y2O3 thermal barrier coatings, *International Journal of Applied Ceramic Technology*, 2004, **1**(4), p. 330-342.

19. F. Kroupa, Residual stresses in thick, nonhomogeneous coatings, *Journal of Thermal Spray Technology*, 1997, **6**(3), p. 309-319.

20. F. Kroupa, and J. Dubsky, Pressure dependence of Young's moduli of thermal sprayed materials, *Scripta Materialia*, 1999, **40**(11), p. 1249-1254.

21. F. Kroupa, and J. Plesek, Nonlinear elastic behavior in compression of thermally sprayed materials, *Materials Science and Engineering a-Structural Materials Properties Microstructure and Processing*, 2002, **328**(1-2), p. 1-7.

22. V. Harok, and K. Neufuss, Elastic and inelastic effects in compression in plasma-sprayed ceramic coatings, *Journal of Thermal Spray Technology*, 2001, **10**(1), p. 126-132.

23. J.I. Eldridge, G.N. Morscher, and S.R. Choi, Quasistatic vs. dynamic modulus measurements of plasma- sprayed thermal barrier coatings, *Ceramic Engineering Science Proceedings*, 2002, 23), p. 371-378

24. T. Wakui, J. Malzbender, and R.W. Steinbrech, Strain analysis of plasma sprayed thermal barrier coatings under mechanical stress, *Journal of Thermal Spray Technology*, 2004, **13**(3), p. 390-395.

25. W.Z. Wang, C.J. Li, Y.Y. Wang, G.J. Yang, and K. Sonoya, Tensile deformation behavior of plasma-sprayed Ni-45Cr coatings, *Surface & Coatings Technology*, 2006, **201**(3-4), p. 842-847.

26. Y.J. Liu, T. Nakamura, G. Dwivedi, A. Valarezo, and S. Sampath, Anelastic Behavior of Plasma-Sprayed Zirconia Coatings, *Journal of the American Ceramic Society*, 2008, **91**(12), p. 4036-4043.

27. H. Herman, and N.R. Shankar, Fundamental-Aspects of Thermal Barrier Coatings, *American Ceramic Society Bulletin*, 1984, **63**(12), p. 1475-1475.

28. H. Herman, Plasma-Sprayed Coatings, *Scientific American*, 1988, **259**(3), p. 112-117.

29. P. Fauchais, Formation of Plasma-Sprayed Coatings, *Journal of Thermal Spray Technology*, 1995, **4**(1), p. 3-6.

30. S. Sampath, and H. Herman, Rapid solidification and microstructure development during plasma spray deposition, *Journal of Thermal Spray Technology*, 1996, **5**(4), p. 445-456.

31. P. Fauchais, M. Fukumoto, A. Vardelle, and M. Vardelle, Knowledge concerning splat formation: An invited review, *Journal of Thermal Spray Technology*, 2004, **13**(3), p. 337-360.

32. S. Sampath, and R. McCune, Thermal-spray processing of materials, *Mrs Bulletin*, 2000, **25**(7), p. 12-14.

33. S. Kuroda, T. Dendo, and S. Kitahara, Quenching Stress in Plasma-Sprayed Coatings and Its Correlation with the Deposit Microstructure, *Journal of Thermal Spray Technology*, 1995, **4**(1), p. 75-84.

34. Z. Wang, A. Kulkarni, S. Deshpande, T. Nakamura, and H. Herman, Effects of pores and interfaces on effective properties of plasma sprayed zirconia coatings, *Acta Materialia*, 2003, **51**(18), p. 5319-5334.

35. S.C. Gill, and T.W. Clyne, Stress Distributions and Material Response in Thermal Spraying of Metallic and Ceramic Deposits, *Metallurgical Transactions B-Process Metallurgy*, 1990, **21**(2), p. 377-385.

36. S. Kuroda, and T.W. Clyne, The Quenching Stress in Thermally Sprayed Coatings, *Thin Solid Films*, 1991, **200**(1), p. 49-66.

37. L. Li, A. Vaidya, S. Sampath, H.B. Xiong, and L.L. Zheng, Particle characterization and splat formation of plasma sprayed zirconia, *Journal of Thermal Spray Technology*, 2006, **15**(1), p. 97-105.

38. A. Kulkarni, Z. Wang, T. Nakamura, S. Sampath, A. Goland, H. Herman, J. Allen, J. Ilavsky, G. Long, J. Frahm, and R.W. Steinbrech, Comprehensive microstructural characterization and predictive property modeling of plasma-sprayed zirconia coatings, *Acta Materialia*, 2003, **51**(9), p. 2457-2475.

39. A. Kulkarni, A. Vaidya, A. Goland, S. Sampath, and H. Herman, Processing effects on porosity-property correlations in plasma sprayed yttria-stabilized zirconia coatings, *Materials Science and Engineering a-Structural Materials Properties Microstructure and Processing*, 2003, **359**(1-2), p. 100-111.

40. A. Kulkarni, J. Gutleber, S. Sampath, A. Goland, W.B. Lindquist, H. Herman, A.J. Allen, and B. Dowd, Studies of the microstructure and properties of dense ceramic coatings produced by high-velocity oxygen-fuel combustion spraying, *Materials Science and Engineering a-Structural Materials Properties Microstructure and Processing*, 2004, **369**(1-2), p. 124-137.

41. A. Kulkarni, On The Porosity-Property Correlations In Thermo-Structural Coatings: Towards An Integrated Approach, *Ph.D. Thesis, State University of New York at Stony Brook,* , 2002,

42. A.J. Allen, G.G. Long, H. Boukari, J. Ilavskya, A. Kulkarni, S. Sampath, H. Herman, and A.N. Goland, Microstructural characterization studies to relate the properties of thermal-spray coatings to feedstock and spray conditions, *Surface & Coatings Technology*, 2001, **146,** p. 544-552.

43. W.G. Chi, S. Sampath, and H. Wang, Microstructure-thermal conductivity relationships for plasma-sprayed yttria-stabilized zirconia coatings, *Journal of the American Ceramic Society*, 2008, **91**(8), p. 2636-2645.

44. W. Chi, "Thermal Transport Properties of Thermally Sprayed Coatings: An Integrated Study of Materials, Processing and Microstructural Effects," PhD Thesis, Stony Brook Univerisity, 2007

45. J.R. Colmenares-Angulo, V. Cannillo, L. Lusvarghi, A. Sola, and S. Sampath, Role of process type and process conditions on phase content and physical properties of thermal sprayed TiO2 coatings, *Journal of Materials Science*, 2009, **44**(9), p. 2276-2287.

46. Y.P. Li, W.G. Chi, S. Sampath, A. Goland, H. Herman, A.J. Allen, and J. Ilavsky, Process-Controlled Plasma-Sprayed Yttria-Stabilized Zirconia Coatings: New Insights from Ultrasmall-Angle X-ray Scattering, *Journal of the American Ceramic Society*, 2009, **92**(2), p. 491-500.

47. Y. Liu, T. Nakamura, V. Srinivasan, A. Vaidya, A. Gouldstone, and S. Sampath, Non-linear elastic properties of plasma-sprayed zirconia coatings and associated relationships with processing conditions, *Acta Materialia*, 2007, **55**(14), p. 4667-4678.

48. T. Nakamura, G. Qian, and C.C. Berndt, Effects of pores on mechanical properties of plasma-sprayed ceramic coatings, *Journal of the American Ceramic Society*, 2000, **83**(3), p. 578-584.

49. M.W. Arai, Xiaohong, and K. Fujimoto, Inelastic Deformation of Freestanding Plasma-sprayed Thermal Barrier Coatings, *Journal of solid Mechanics and Materials Engineering*, 2010, **4**(2), p. 1-14

50. G. Dwivedi, T. Nakamura, and S. Sampath, Controlled Introduction of Anelasticity in Plasma-Sprayed Ceramics, *Journal of the American Ceramic Society*, 2011,

51. B. Dussoubs, G. Mariaux, A. Vardelle, M. Vardelle, and P. Fauchais, DC plasma spraying: Effect of arc root fluctuations on particle behavior in the plasma jet, *High Temperature Material Processes*, 1999, **3**(2-3), p. 235-254.

52. P. Fauchais, J.F. Coudert, and B. Pateyron, The production of thermal plasma, *Revue Generale De Thermique*, 1996, **35**(416), p. 543-560, in French

53. P. Fauchais, A. Grimaud, A. Vardelle, and M. Vardelle, Plasma Spraying - an Overview, *Annales De Physique*, 1989, **14**(3), p. 261-310, in French

54. V. Srinivasan, M. Friis, A. Vaidya, T. Streibl, and S. Sampath, Particle injection in direct current air plasma spray: Salient observations and optimization strategies, *Plasma Chemistry and Plasma Processing*, 2007, **27**(5), p. 609-623.

55. T. Streibl, A. Vaidya, M. Friis, V. Srinivasan, and S. Sampath, A critical assessment of particle temperature distributions during plasma spraying: Experimental results for YSZ, *Plasma Chemistry and Plasma Processing*, 2006, **26**(1), p. 73-102.

56. S. Sampath, X.Y. Jiang, J. Matejicek, A.C. Leger, and A. Vardelle, Substrate temperature effects on splat formation, microstructure development and properties of plasma sprayed coatings Part I: Case study for partially stabilized zirconia, *Materials Science and Engineering a-Structural Materials Properties Microstructure and Processing*, 1999, **272**(1), p. 181-188.

57. X. Yang, "Identification of Nonlinear Properties of Thermal Spray Zirconia under Mechanical Loading," MS Thesis, Stony Brook University, May 2009

58. C.A. Johnson, J.A. Ruud, R. Bruce, and D. Wortman, Relationships between residual stress, microstructure and mechanical properties of electron beam physical vapor deposition thermal barrier coatings, *Surface & Coatings Technology*, 1998, **109**(1-3), p. 80-85.

59. S. Kuroda, T. Fukushima, and S. Kitahara, Simultaneous Measurement of Coating Thickness and Deposition Stress during Thermal Spraying, *Thin Solid Films*, 1988, **164**(p. 157-163.

60. J. Matejicek, and S. Sampath, In situ measurement of residual stresses and elastic moduli in thermal sprayed coatings - Part 1: apparatus and analysis, *Acta Materialia*, 2003, **51**(3), p. 863-872.

61. T. Nakamura, and Y.J. Liu, Determination of nonlinear properties of thermal sprayed ceramic coatings via inverse analysis, *International Journal of Solids and Structures*, 2007, **44**(6), p. 1990-2009.

62. G.G. Stoney, The tension of metallic films deposited by electrolysis, *Proceedings of the Royal Society of London Series a-Containing Papers of a Mathematical and Physical Character*, 1909, **82**(553), p. 172-175.

63. A. Brenner, and S. Senderoff, Calculation of Stress in Electrodeposits from the Curvature of a Plated Strip, *Journal of Research of the National Bureau of Standards*, 1949, **42**(2), p. 105-123.

64. Y.C. Tsui, and T.W. Clyne, An analytical model for predicting residual stresses in progressively deposited coatings .1. Planar geometry, *Thin Solid Films*, 1997, **306**(1), p. 23-33.

65. Y. Liu, "Anelastice Behavior of Thermal Spray Coatings and Associated Relationships with Processing Conditions.," Stony Brook University

66. D.R. Clarke, and C.G. Levi, Materials design for the next generation thermal barrier coatings, *Annual Review of Materials Research*, 2003, **33**(p. 383-417.

67. G. Dwivedi, T. Wentz, S. Sampath, and T. Nakamura, Assessing Process and Coating Reliability Through Monitoring of Process and Design Relevant Coating Properties, *Journal of Thermal Spray Technology*, 2010, **19**(4), p. 695-712.

68. D. Basu, C. Funke, and R.W. Steinbrech, Effect of heat treatment on elastic properties of separated thermal barrier coatings, *Journal of Materials Research*, 1999, **14**(12), p. 4643-4650.

69. R.W. Steinbrech, Thermomechanical Behavior of Plasma Sprayed Thermal Barrier Coatings., *Ceramic engineering and science proceedings*, 2000, **23**(379-408))

70. S.C. Zuo, and Y.G. Wei, Microstructure observation and mechanical behavior modeling for limnetic nacre, *Acta Mechanica Sinica*, 2008, **24**(1), p. 83-89.

71. H.D. Espinosa, J.E. Rim, F. Barthelat, and M.J. Buehler, Merger of structure and material in nacre and bone - Perspectives on de novo biomimetic materials, *Progress in Materials Science*, 2009, **54**(8), p. 1059-1100.

72. S. Patsias, N. Tassini, and K. Lambrinou, Ceramic coatings: Effect of deposition method on damping and modulus of elasticity for yttria-stabilized zirconia, *Materials Science and Engineering a-Structural Materials Properties Microstructure and Processing*, 2006, **442**(1-2), p. 504-508.

73. N. Tassini, S. Patsias, and K. Lambrinou, Ceramic coatings: A phenomenological modeling for damping behavior related to microstructural features, *Materials Science and Engineering a-Structural Materials Properties Microstructure and Processing*, 2006, **442**(1-2), p. 509-513.

74. P.J. Torvik, A Slip Damping Model for Plasma Sprayed Ceramics, *Journal of Applied Mechanics-Transactions of the Asme*, 2009, **76**(6).

75. A.M. Limarga, T.L. Duong, G. Gregori, and D.R. Clarke, High-temperature vibration damping of thermal barrier coating materials, *Surface & Coatings Technology*, 2007, **202**(4-7), p. 693-697.

76. K.W. Schlichting, N.P. Padture, E.H. Jordan, and M. Gell, Failure modes in plasma-sprayed thermal barrier coatings, *Materials Science and Engineering a-Structural Materials Properties Microstructure and Processing*, 2003, **342**(1-2), p. 120-130.

77. N.P. Padture, M. Gell, and E.H. Jordan, Materials science - Thermal barrier coatings for gas-turbine engine apptications, *Science*, 2002, **296**(5566), p. 280-284.

78. W.J. Brindley, and R.A. Miller, Tbcs for Better Engine Efficiency, *Advanced Materials & Processes*, 1989, **136**(2), p. 29-33.

79. A.C. Fox, and T.W. Clyne, Oxygen transport by gas permeation through the zirconia layer in plasma sprayed thermal barrier coatings, *Surface & Coatings Technology*, 2004, **184**(2-3), p. 311-321.

80. P.F. Zhao, C.A. Sun, X.Y. Zhu, F.L. Shang, and C.J. Li, Fracture toughness measurements of plasma-sprayed thermal barrier coatings using a modified four-point bending method, *Surface & Coatings Technology*, 2010, **204**(24), p. 4066-4074.

81. A. Shyam, and E. Lara-Curzio, The double-torsion testing technique for determination of fracture toughness and slow crack growth behavior of materials: A review, *Journal of Materials Science*, 2006, **41**(13), p. 4093-4104.